SEISMIC HAZARD ANALYSIS USING THE AMBIENT SEISMIC FIELD

A DISSERTATION
SUBMITTED TO THE DEPARTMENT OF GEOPHYSICS
AND THE COMMITTEE ON GRADUATE STUDIES
OF STANFORD UNIVERSITY
IN PARTIAL FULFILLMENT OF THE REQUIREMENTS
FOR THE DEGREE OF
DOCTOR OF PHILOSOPHY

Marine A. Denolle
April 2014

I certify that I have read this dissertation and that, in my opinion, it is fully adequate in scope and quality as a dissertation for the degree of Doctor of Philosophy.

(Gregory C. Beroza) Principal Adviser

I certify that I have read this dissertation and that, in my opinion, it is fully adequate in scope and quality as a dissertation for the degree of Doctor of Philosophy.

(Eric M. Dunham)

I certify that I have read this dissertation and that, in my opinion, it is fully adequate in scope and quality as a dissertation for the degree of Doctor of Philosophy.

(Germán A. Prieto)

Approved for the University Committee on Graduate Studies

Preface

With the recent occurrence of unexpectedly large earthquakes, seismic hazard analysis is now at a critical point, for which ground motion prediction is a key element. Traditionally, ground motion intensity is predicted using the empirical ground motion prediction equations, relations developed from observed ground motion measurements. There is a clear shortage of data for large events at short distances, and seismologists increasingly turn to physics based approaches to simulate ground shaking. Ground motion prediction is commonly divided into three main components: source characterization, wave propagation through a three-dimensional crustal structure, and non-linear site response. Each of these represents a challenging research endeavor, with significant source of uncertainty.

In this thesis, I develop the foundation for using ambient-noise seismology to predict ground motion, and apply the methods I build to data in California and Japan. The cross-correlation of the ambient noise recorded simultaneously at two seismic stations has similar properties to the Green's function between the two stations. In this thesis, I develop techniques for robust estimation of reliable Green's functions. Once stable Green's functions are obtained, I use a newly established surface-wave eigen problem solver to correct the surface impulse response for source depth and mechanism to construct a virtual earthquake. I validate the virtual earthquake seismograms against data from nearby moderate earthquakes and demonstrate that strong basin amplification occurs at the same locations in both data sets. I expand the virtual point sources to extended ruptures and characterize the Los Angeles sedimentary basin amplification sensitivity to M7+ scenarios on the San Andreas Fault. In Japan, I use the ambient seismic field Green's functions to characterize basin resonance,

identify virtual sources that have for strong shaking potential and recover detailed and complex wave propagation effects due to the basin structure that affect seismic amplification in central Tokyo.

This thesis demonstrates the powerful opportunities that weak signals like the ambient seismic field bring to seismic hazard analysis, and gives rise to new research questions that will contribute to improve our understanding of the seismic hazard in populated areas.

Acknowledgements

This work was supported by NSF Grant EAR-0943885, by the NSF Grant EAR-0949443, and was supported by the SAVI supplement to NSF Cooperative Agreement EAR-1033462.

I am very thankful of the scientists surrounding my time at Stanford, who have trusted me as a student, and made me become a scientist. I am lucky to learn from all of them.

In particular, my advisor Greg Beroza. Greg has undoubtedly been the perfect advisor and mentor for me. Through the years, Greg made me understand that the best quality of an advisor is to help the student meet his/ her own expectations and goals. Greg lead me to meet mines by giving me all the freedom to take my own directions, and yet steering my PhD along the path that would guarantee success. He has been patient and understanding of the many activities I undertook to fully enjoy the Stanford grad life, and is constantly looking up for my career in academia. I am privileged to be his student.

I greatly thank Eric Dunham for bringing so much to my research, for steering my reasoning in seismology in new and challenging directions. He is an rigorous scientist and writer and I am so grateful to have taken advantage of his time when it was most appropriate for my research.

I deeply thank Germán Prieto who started my PhD in 2008. Despite the distance, Germán has always been present and helpful for my research over the years, always available to provide feedback and greatly contributed to shape my research.

I thank Jesse Lawrence for being such a great mentor through the years. Jesse not only largely contributed to leading my research questions, to developing all the

tools I needed to handle large data sets, but also was a great mentor through the PhD experience.

I thank Paul Segall for always sitting on my committee and challenging me with rigorous and critical thinking. I thank George Hilley for being chair of my PhD committee, and for opening my thoughts on Earthquake Risk through his class.

I thank Roni, Tara, Natasha, Lauren, Csilla and Nancy for making life flow easily in the School of Earth Sciences, for allowing me to organize all kind of social events: beading, wine tasting, sake tasting, crepe parties etc etc, and to take full advantage of the great resources at Stanford. I spent great years in my research group with Annemarie, Justin, Ana, Sarah, and Clara. They are great colleagues and great friends.

Without my friends, colleagues, and awesome housemates, I would have graduated earlier, but not as happy! Among the exhaustive list of friends, and in addition to my research group, I thank Lida, Sjoerd, Jess, Dan, Zach, Noa, Mike O., Ohad, Cyndi, Katherine, Hari, Heather, Addy, and Ekin, my friends Annemarie, Sara, Sean, Joe for sharing great skiing days.

I thank Brad for bringing me so much over the past few years, in particular his unconditional support, patience and great science conversations during our Sierra adventures.

Depuis les Etats Unis, je tiens a remercier principalement ma famille qui m'a toujours soutenue dans mon long parcours, qui a été toujours a l'écoute, depuis la France, de ma passion envers ma recherche.

Contents

List of Tables

List of Figures

Chapter 1

Introduction

With the recent occurrent of unexpectedly large earthquakes, ground motion prediction is now at a critical stage. To mitigate the risk in the future damaging earthquakes, there is a parallel development of approaches that attempt to characterize shaking hazard for large events: the empirical and the physics-based approaches.

The first approach relies on shaking intensity measurements of past earthquakes to build empirical laws, called the Ground Motion Prediction Equations (GMPEs) that predict ground motion based on a set of parameters that reflect in particular the source processes, distance from the earthquake, and site conditions. The product of this approach used by the structural engineers that design buildings to sustain the predicted shaking, and to the authorities to establish appropriate building codes. The second approach is based on a physical understanding of earthquake processes. Recent observations of large earthquakes fuel a interest in modeling the complex rupture mechanics behind them. There is also growing knowledge of the Earth's structure accruing from efforts made in active seismic surveys, body and surface-wave tomography and coring, to establish accurate and detailed velocity models. Finally, the rapid development of high-performance computing capabilities creates opportunities to model complex and large earthquake rupture, and to propagate the radiated seismic waves in fairly complex velocity models, and to finally predict ground motion.

While those two approaches are by nature independent, there is an progressive undertaking of cross-validation of those two approaches. For instance, *Day et al.* (2008) simulate scenario earthquakes in southern California using a complex velocity structure that includes sedimentary basins, and build relations between the predicted shaking intensity and basin depth. The results of that study made the engineering community incorporate basin effects in the GMPEs (*Abrahamson et al.*, 2013; *Campbell and Bozorgnia*, 2013). Physics-based approaches are limited by the accuracy of the velocity models, and by the validity of the models of complex earthquake mechanics. The GMPEs are most limited by a shortage of data for large events at short distances. If physics-based methods are to be trusted, they need to be validated against earthquake data. I undertake this effort in this dissertation. I characterize complex wave propagation effects in sedimentary basins and build large virtual

earthquakes using the ambient seismic field.

New opportunities in seismology have emerged through analysis of the ambient seismic field. One key characteristic of the ambient seismic field is its similarity to diffuse acoustic fields. The cross-correlation of acoustic diffuse fields recorded at two sensors is related to the impulse response of the medium in which the seismic waves travel. The second key element in analyzing the ambient seismic field is that it is recorded continuously at any seismic station. This contrasts with the signals that we use, mostly earthquake signals and their often location and timing that do not favor traditional methods in seismology. *Aki* (1957) was first to make use of the ambient seismic field to construct the Green's function through the spatial autocorrelation method. *Claerbout* (1968) formulated the relation between cross-correlation seismograms at the surface and seismograms from real buried earthquakes. Helioseismology (*Rickett and Claerbout*, 1999) adopted the concept while acoustics explored the conditions under which we can extract the true Green's function (*Lobkis and Weaver*, 2001; *Weaver and Lobkis*, 2006). But it is only with the studies from *Campillo and Paul* (2003); *Shapiro and Campillo* (2004); *Sabra et al.* (2005a) that truly sparked a new movement in earthquake seismology to extract seismic-wave propagation information through the analysis of the ambient seismic field and the coda waves.

There are numerous names to the cross-correlation function, empirical and/or elastodynamic Green's function, impulse response, transfer function, or coherency, but they always refer to the response of the medium to an impulse point source force. We obtain in practice the impulse response by cross-correlating the simultaneously recorded diffuse seismic field, commonly the ambient seismic field or coda-wave from earthquakes, recorded at two sensors, usually seismic stations. Under appropriate conditions (*Snieder*, 2004; *Sánchez-Sesma and Campillo*, 2006; *Sánchez-Sesma et al.*, 2008), the cross-correlation function of the diffuse seismic fields resembles these Green's function, both in phase and amplitude. Because the seismic sensors are often located at the surface, the fundamental mode of the surface waves dominates the Green's functions (*Campillo and Paul*, 2003; *Shapiro and Campillo*, 2004; *Sabra et al.*, 2005a). The phase and amplitude information captured in the correlation function

provides opportunities to characterize the medium underneath, but their accuracy needs to be verified.

The averaged group and phase velocities between the two seismic sensors that we measure with the cross-correlation function are fairly accurate. The velocity measurements obtained from this technique benefit the tomography studies(*Shapiro et al.*, 2005; *Sabra et al.*, 2005b; *Bensen et al.*, 2008; *Lin et al.*, 2008; *Nishida et al.*, 2008; *Roux*, 2009; *Moschetti et al.*, 2010; *Lawrence and Prieto*, 2011; *Karplus et al.*, 2013) in regions where data is limited. Although the accuracy in those measurements needs to be addressed (*Weaver et al.*, 2009; *Tsai*, 2009; *Froment et al.*, 2010), they allow monitoring wave-speed changes in volcanoes (*Brenguier et al.*, 2008a; *Duputel et al.*, 2009), and may bring new information on post seismic response of the crust (*Brenguier et al.*, 2008b; *Minato et al.*, 2012).

Developing reliable amplitude measurements, however, is more difficult. Most data processing techniques used to recover accurate phase measurements, such as converting to sign-bit, annihilate the amplitude information (*Bensen et al.*, 2007). *Prieto and Beroza* (2008), *Prieto et al.* (2009), and *Lawrence and Prieto* (2011) use the simple measurement of unprocessed ambient seismic field to recover the amplitudes predicted from earthquakes and infer attenuation information at a regional scale. Theory-based analysis raises important questions about the ability to trust amplitude measurements, primarily due to the effects of non-uniform noise source distribution (*Tsai*, 2011); however, numerical studies agree with the empirical results and indicate that such concerns are exaggerated (*Cupillard et al.*, 2011; *Lawrence et al.*, in press).

While most of the interest in the ambient seismic field studies has been drawn toward characterizing and imaging the Earth's structure, my PhD work is different. I focused my research to making use of the amplitude information to understand seismic hazard. *Prieto and Beroza* (2008) demonstrates the similarity between the waveforms from the Ambient Seismic Field (ASF) impulse responses and the records from a moderate earthquake in southern California. The similarity between the ASF Green's functions and the earthquake records also demonstrated that we could retrieve the seismic amplification observed in long-period surface waves when traveling through complex sedimentary structure. The correlation function obtained from the ASF is

the response of the medium to an impulse point force located at the surface. Real earthquakes, however, have mechanisms that can be represented by a double couple force system acting at depth. Moreover, for significant earthquakes, the finite extent and evolution of rupture propagation are important.

In this thesis, I present a new approach to construct seismograms for long-period surface-waves from large virtual earthquakes, and I carried out research using data in both southern California, USA, and in Kanto, Japan. Figure 1.1 illustrates the steps to this approach, and its presentation by chapters. We first record the ambient seismic field continuously at seismic stations that are located at the surface (a), and we construct the impulse response (b), assuming that one station acts as a virtual source. The impulse responses themselves carry most of the information of complex wave propagation effects, such as the ones that dominate the strong ground motion in sedimentary basins.

In Chapter 2, I use the simple surface-to-surface responses from virtual sources located in Honshu to receivers located in Kanto. By using two dense seismic networks, I am able to characterize the resonance of the sedimentary basin underlying Tokyo, to identify the location of virtual earthquakes in central Honshu that would most affect the shaking in Tokyo, and finally to explain observed strong shaking from complex wave propagation effects such as surface-wave to body waves conversions.

To construct long-period seismograms from large earthquakes, the surface-to-surface impulse response needs to be corrected to capture the surface-wave excitation for a buried source. The surface-wave excitation depends strongly on the local structure and on the source depth. In Chapter 3 (step (c) of Fig. 1.1), I develop a new approach to solve the surface-wave eigen problem using spectral collocation given the piecewise smooth velocity profile underneath the station source. Using this information, in Chapter 4, step (d-e), I correct the surface-to-surface response to the responses of a realistic dislocation source located at depth. I validate the method, that we refer to as the Virtual Earthquake Approach, against four moderate earthquakes in southern California.

In Chapter 5, I extend the point source approximation to reproduce the ground motion from large earthquakes. To construct the Green's functions from virtual

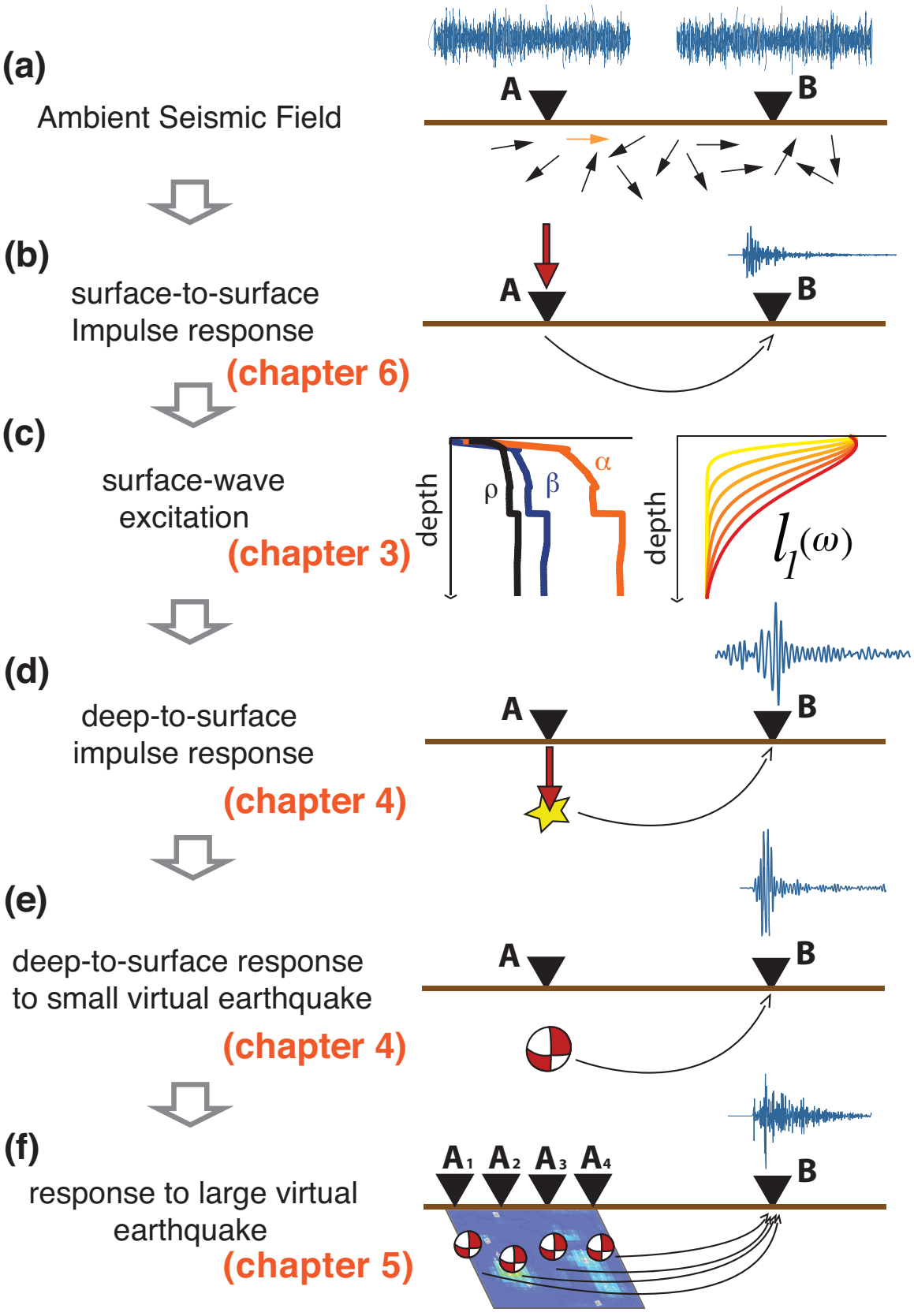

Figure 1.1: Roadmap of the virtual earthquake approach and related chapter in this dissertation.

sources on the southern San Andreas Fault, I deployed a temporary array composed of 10 broadband sensors along the fault. I refer to this experiment as San Andreas Virtual Earthquake - Los Angeles (SAVELA). I deployed between mid-February and mid-June 2010, period during which the El Mayor – Cucapah M7.2 earthquake occurred, limiting our recordings of ambient seismic field to half the planned duration. Despite the limited data, I construct Green's functions that are of sufficient quality to evaluate first order effects of the finite rupture on long period ground motion. I use realistic pseudo-dynamic source models (*Graves et al.*, 2011) to construct a large virtual earthquake, and this allows me to compare directly the Virtual Earthquake Approach waveforms with ground motion simulated from physics-based approaches for the same sources. I find a coupling of source directivity with basin structure, and greatly enhanced ground motion due to deep sedimentary basin and to the presence of a seismic waveguide. Moreover, I find overall larger shaking than predicted from the CyberShake ground motion simulations.

The SAVELA deployment is only a pilot experiment that represents a first step in predicting ground motion from the ambient seismic field for significant scenario earthquakes. The Virtual Earthquake Approach provides a new and independent way to characterize the shaking hazard of large earthquakes at long periods and should be incorporated in Seismic Hazard Analysis.

Chapter 2

Amplification Hazard in Kanto Basin, Japan

Introduction

Urban settings where tall structures are present, the prediction of long-period strong ground motion is a key component of seismic hazard analysis. Among the metropolitan areas that are highly exposed to seismic activity, some are situated on top of sedimentary basins that consist of unconsolidated sediments surrounded by stiff bedrock. Such complex velocity structure can trap seismic waves, increase their amplitudes, and extend the duration of shaking, which greatly affect damage. These effects can overwhelm the amplitude decay with increasing distance from the earthquake source. The most dramatic example of strong seismic amplification distant from the source is the M 8.0, 1985 Michoacan earthquake, that devastated Mexico City in a subduction event that was 300 km distant from the city. This earthquake lead the seismology community to pay closer attention to wave propagation effects in unconsolidated sediments (*Bard et al.*, 1988; *Aki*, 1993; *Furumura and Kennett*, 1998).

In Japan, the damage caused by the M8.3 Tokachi-oki, 2003 in Hokkaido, were largely due to long-period surface waves that amplified in soft sediments (*Koketsu et al.*, 2005). *Miyake and Koketsu* (2005) used earthquakes off the Kii Peninsula to estimate the natural excitation of three major sedimentary basins, Osaka, Nagoya and Kanto. They found a relatively long-period resonance (4 – 10 s), which correlates with the shape and thickness of the sediment structure. Seismic amplification was also found in the Kanto Basin during the M6.8 Chuetsue, 2004 and the M6.6 Chuetsu-oki, 2007, earthquakes (*Furumura and Hayakawa*, 2007; *Koketsu and Miyake*, 2008).

The Kanto sedimentary basin consists of unconsolidated sediments with S-wave velocities as low as 500 m/s (*Yamada and Iwata*, 2005; *Yamanaka and Yamada*, 2006; *Tanaka et al.*, 2005), and a bedrock basement as deep as 4 km underneath Chiba prefecture (*Afnimar et al.*, 2003). The concave structure of the sediments combined with their low wave speed yield a resonance period of approximately 7 s (*Miyake and Koketsu*, 2005; *Furumura and Hayakawa*, 2007). Large displacements were recorded, and simulated, during the Niigata-Chuetsu earthquakes (*Miyake and Koketsu*, 2005; *Furumura and Hayakawa*, 2007). These authors propose the presence of a seismic waveguide near the Gunma pass that would funnel seismic waves from

the Niigata region into the Kanto Basin. Waveguides in other settings are known to enhance seismic amplification by giving waves into sedimentary basins (*Olsen et al.*, 2006, 2009; *Day et al.*, 2012; **?**).

The large and dense seismic network MeSO-net (Metropolitan Seismic Observation Network) (*Sakai and Hirata*, 2009; *Kasahara et al.*, 2009) focused on the scientific goal of characterizing the structure under Tokyo, and in delineating the underlying plate boundary fault systems. The deployment of the 296 shallow boreholes started 2009, and provides dense coverage of sensors in the Kanto Basin (Fig. 2.1). Other than the distant offshore aftershock sequence of the M9.0 Tohoku-oki, 2011 earthquake, only a few earthquakes of M_{JMA} (magnitude from the Japanese Meteorological Agency) greater than 6 occurred since 2009. *Tsuno et al.* (2012, 2013) used those earthquakes to measure seismic amplification and characterize the resonance frequency of the basin. In addition to the seismic threat posed by the subduction zone earthquake, central Honshu hosts a large number of active faults in the upper crust (Fig. 2.1; *AIST* (2012)). Although some of these faults have been active historically, the lack of instrumentally recorded events from those faults stresses the need to characterize basin amplification from such crustal earthquake.

Since we cannot use earthquakes that have not yet occurred to characterize basin amplification, we propose to use virtual earthquakes through the study of the Ambient Seismic Field (ASF). With this new technique, one receiver acts as a virtual source, and the ambient seismic field held provides the impulse response that includes elastic and anelastic wave propagation effects. Figure 2.1 also shows the location of the Hi-net (High Sensitivity Seismographs Network) borehole seismic stations (*Okada et al.*, 2004; *Obara et al.*, 2005), stations that we propose to use as virtual earthquake sources.

We estimate the impulse responses from all sources (Hi-net stations) in Honshu to all receivers (MeSO-net stations) in Kanto. We estimate the averaged relative peak ground motion (PGM) in the period band of interest (2 – 10 s). Our results support previous correlations between resonance and velocity structure (*Miyake and Koketsu*, 2005). We find positive correlation between the sediment thickness and the mean PGM that is strongest around the period 6 s. We also examine the effect of the

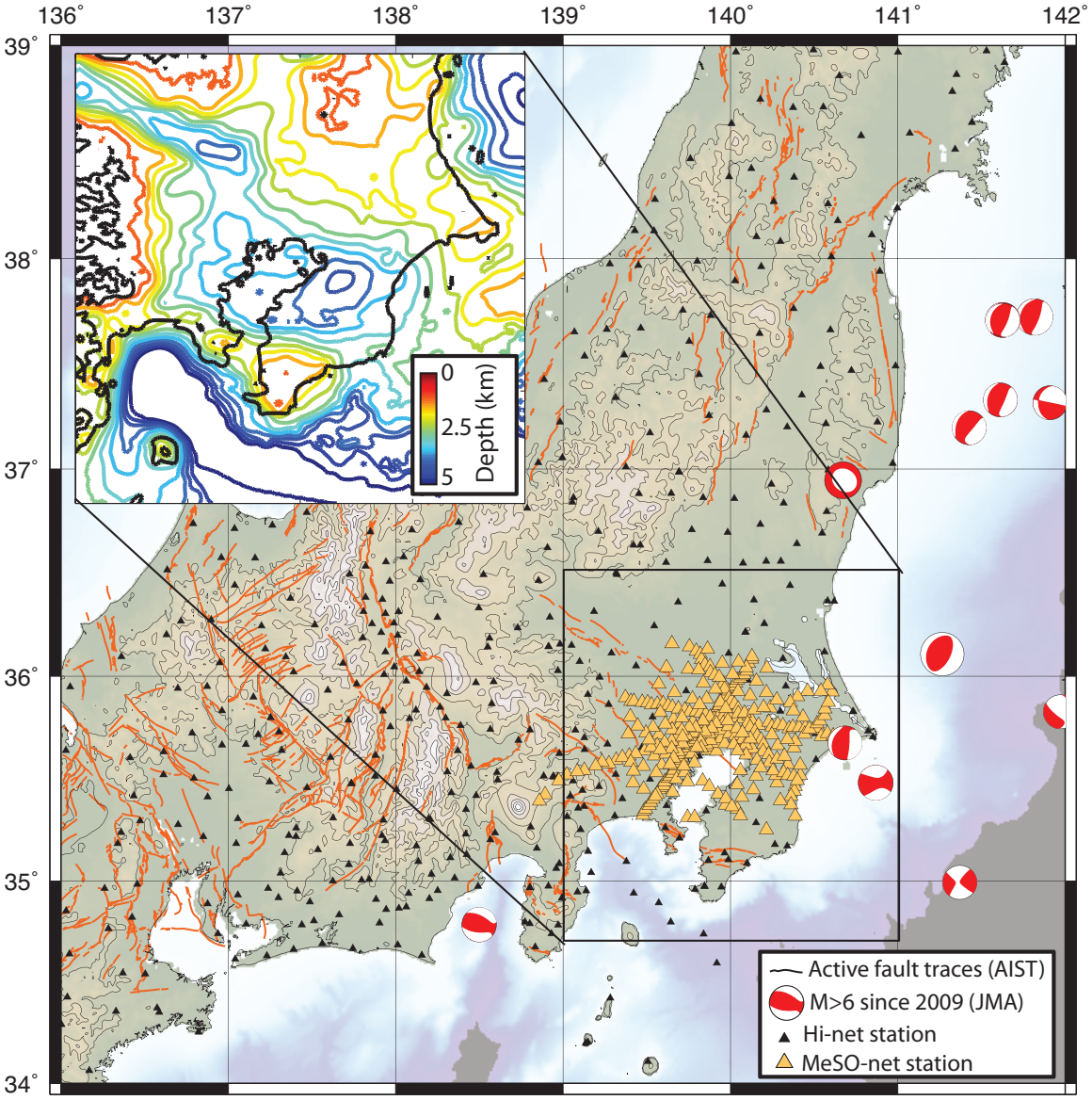

Figure 2.1: Kanto sedimentary basin with the basement depth (upper left inset (*Koketsu et al.*, 2009)), MeSO-net stations (solid gray triangles), Hi-net stations (solid dark triangles), M 6 earthquakes between 2009 and 2013 (JMA location), active fault traces (solid brown curves) from the Research Information Database DB095 (*AIST*, 2012).

direction of seismic illumination on the basin amplification, address the contribution of waveguides in channeling seismic waves into basins, and amplifying seismic waves. We find that the amplification is increased for sources located in Central Honshu in the Suwa Basin. Finally, we present evidence for basin-edge waves that convert from surface to body waves and enhance seismic amplitudes in parts of Kanto Basin.

Ambient Seismic Field Green's functions

We extract the ASF Green's function by convolution of the ambient seismic field recorded simultaneously at two seismic stations. We construct the ASF Green's functions, or impulse response functions, in the frequency domain, from the vertical velocities recorded at the receiver A, $v_A(t)$, and at virtual source B, $v_B(t)$:

$$\widehat{G}_{AB}(\omega) = \left\langle \frac{\hat{v}_A(\omega)\hat{v}_B^*(\omega)}{\{|\hat{v}_A(\omega)|\}^2} \right\rangle, \tag{2.1}$$

where the operator $\langle \quad \rangle$ denotes stacking over time, and $\{ \quad \}$ denotes smoothing over the virtual source spectrum (in our case a 6 mHz running average) to stabilize the deconvolution. We then stack each normalized cross-spectra over many time windows, and by doing so, converge toward a Green's function (*Lobkis and Weaver*, 2001; *Sabra et al.*, 2005a). We use 1-hour long time series, (*Seats et al.*, 2011) and overlap the times series by 20 minutes from 6 months of continuous record.

We treat 375 Hi-Net stations as virtual sources across Honshu and 296 MeSO-Net stations as receivers in Kanto. Using 6 months of continuous record, we detect coherent signal for sources as distant as 300 km from Kanto, covering then source location from Sendai to Osaka. The energetic microseism originating from the Pacific Ocean illuminates Kanto over a wide azimuth (>200°), which greatly contributes to stabilizing the amplitudes of the Green's functions. The coherent signal bandwidth ranges form 2 to 20 s for most station pairs. We define the signal-to-noise ratio as the peak amplitudes of the time series normalized by the standard deviation of the time series ($max|f(t)|$ / std (f(t))). With this measure of stability of amplitude, we

show in Figure 2.2 that directionality of the noise sources does not affect amplitude measurements.

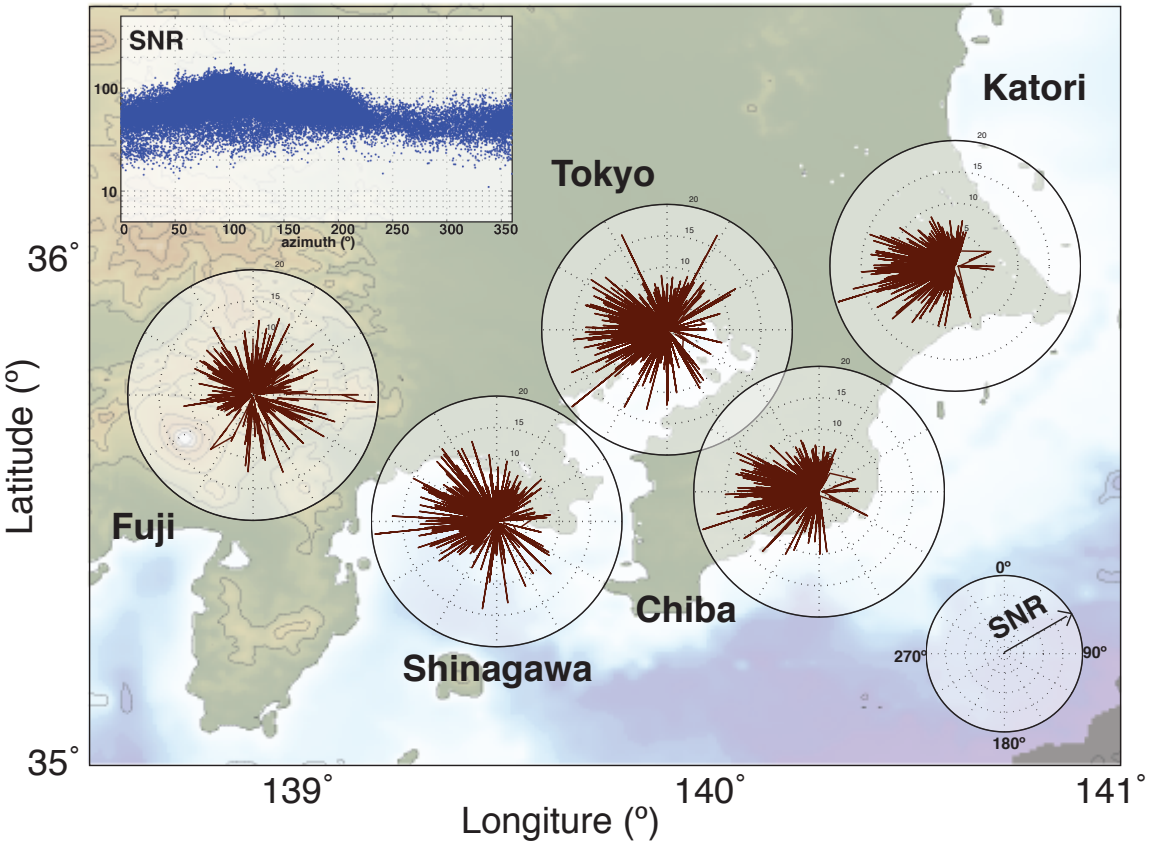

Figure 2.2: Variation of the signal-to-noise ratio $(max|f(t)|/std(f(t)))$ against the azimuth between station source and station-receiver for all station pairs (top left scatter plot), and spatially across Kanto (map view).

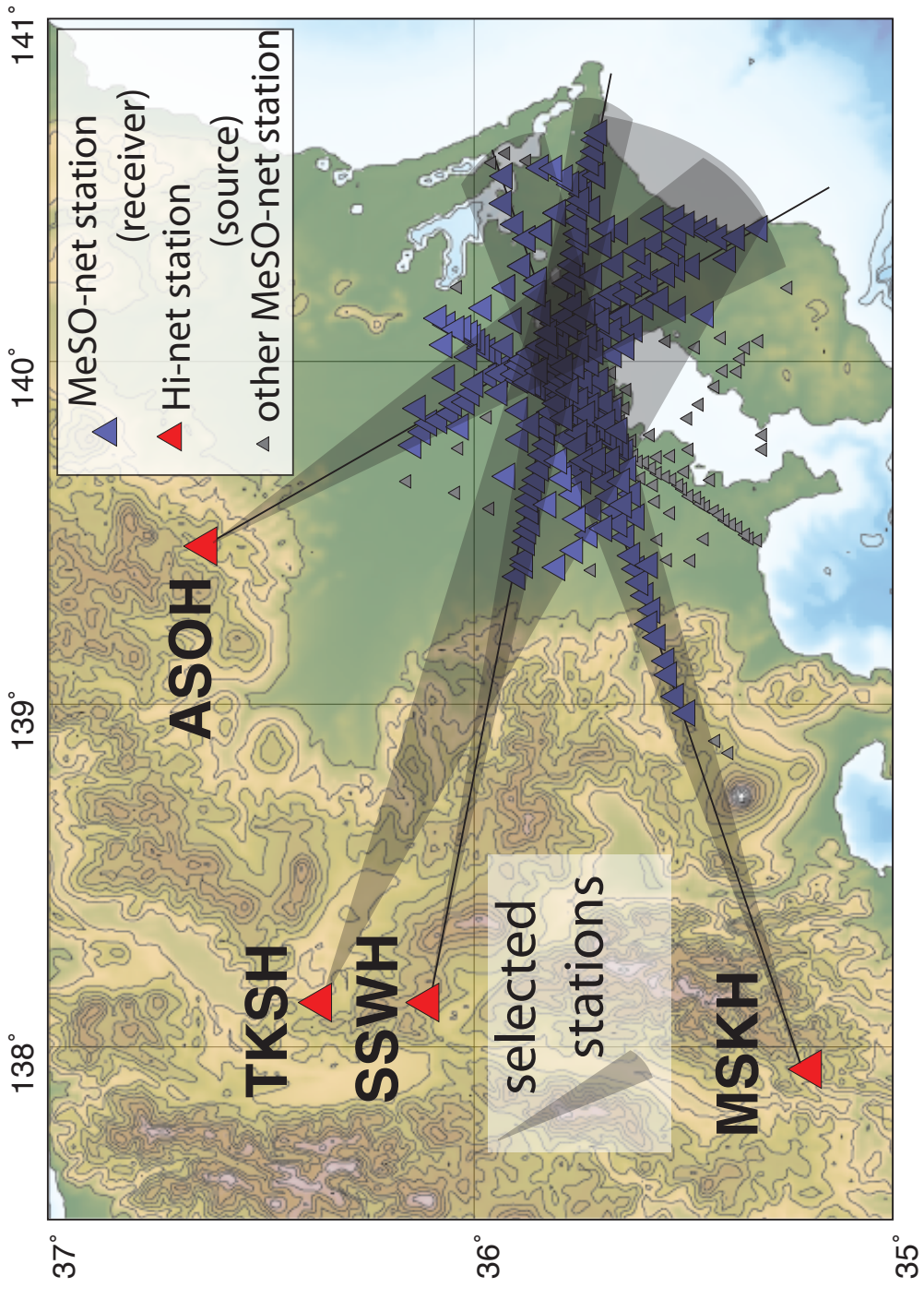

Figure 2.3: Kanto Area with Hi-net sources (red triangles) to a receiver gather of MeSO-net stations (purple triangles) used in Figures 2.4 and 2.5 .

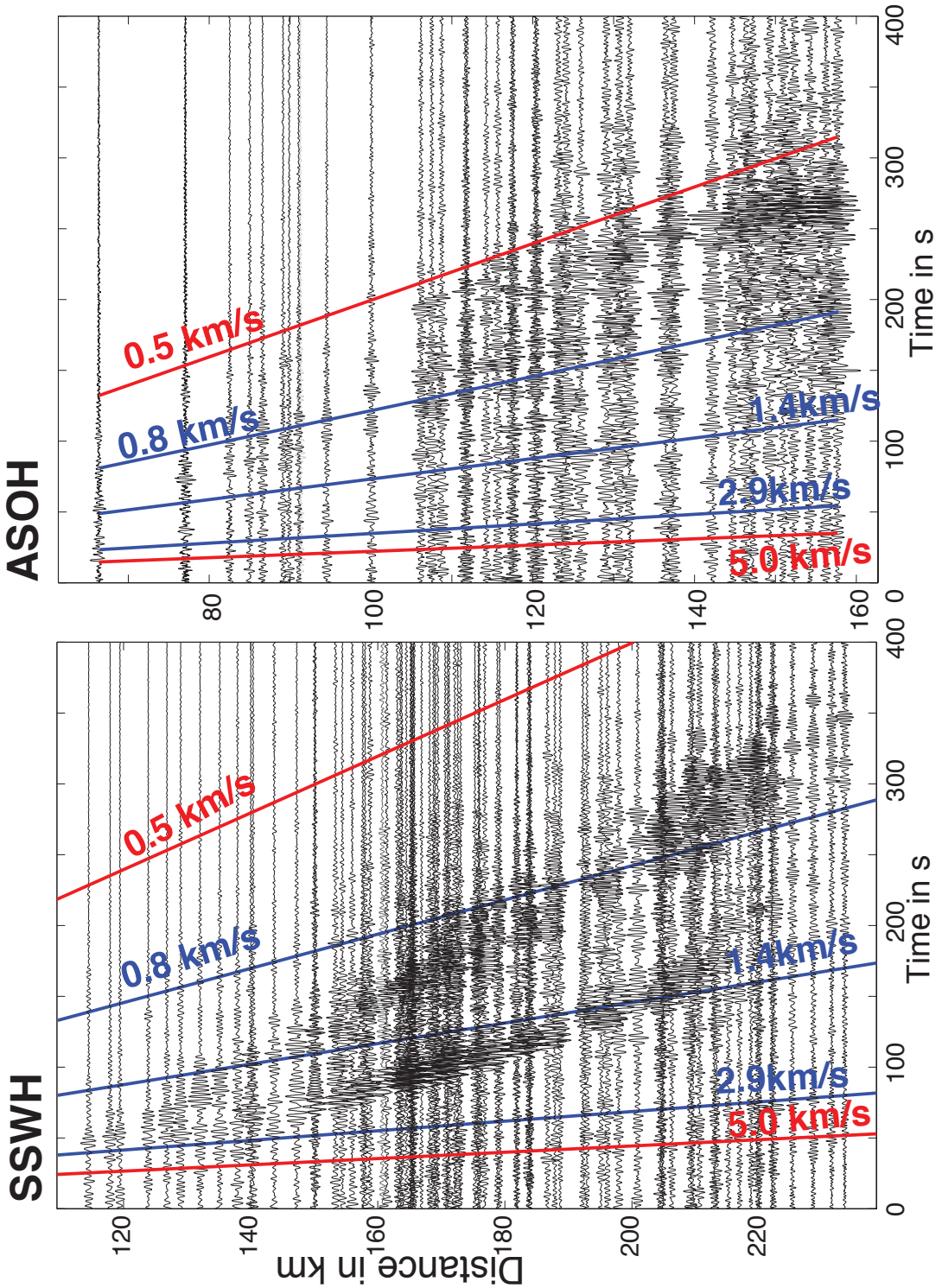

Figure 2.4: Vertical-to-Vertical Green's functions from Hi-net sources to a receiver gather of MeSO-net stations (mapped in Figure 2.3).

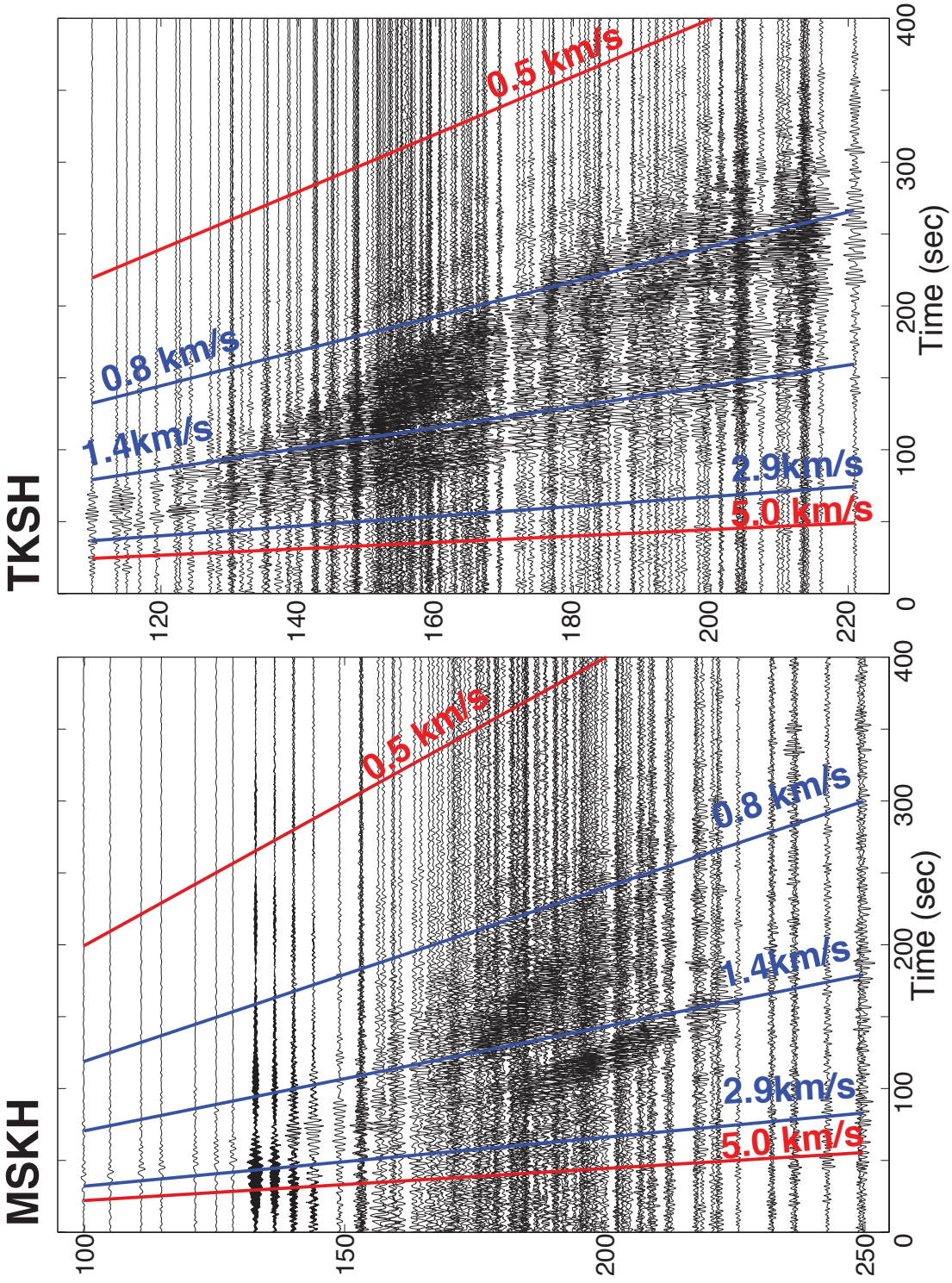

Figure 2.5: Vertical-to-Vertical Green's functions from Hi-net sources to a receiver gather of MeSO-net stations (mapped in Figure 2.3).

We show in Figures 2.3, 2.4, and 2.5 examples of Green's functions for virtual sources distant from the Kanto Basin. We filter the time series between 3 and 10 s. For each source, we select the receivers that fall within a few degrees of azimuth and remove the first order effect of the amplitude decay with distance from the source. Using the ambient seismic field, we reconstruct Rayleigh-wave phase velocities less than 500 m/s. The dispersion of the waveforms is strong in Kanto compared to dispersion of the surface waves for similar source-receiver distances in southern California (*Shapiro et al.*, 2005; *Prieto et al.*, 2009). Despite the expected amplitude decay from geometrical spreading, larger seismic amplitudes dominate the far field, where we expect the interaction with soft sediments to be stronger.

Seismic Amplification in Kanto region

The structure of the sedimentary basin often controls the long-period ground motion in the observations (*Miyake and Koketsu*, 2005; *Koketsu et al.*, 2005; *Koketsu and Miyake*, 2008) and for wave propagation simulations (*Olsen*, 2000; *Furumura and Hayakawa*, 2007; *Olsen et al.*, 2006; *Kawabe and Kamae*, 2008; *Olsen et al.*, 2009; *Iwaki and Iwata*, 2010; *Day et al.*, 2012). We show in Figure 2.1 the contours of the V_S=3.2 km/s isosurface depth, used in *Furumura and Hayakawa* (2007) as a measure of the basin depth, that reflects the shape of the basin and from which we can infer that the strongest effect on trapping seismic waves should occur underneath Chiba Prefecture. We expect the deep basin to affect seismic wave resonance around 7 – 14 s, and shorter periods 2 –17 s for the shallower part, as hypothesized from observations and simulations (*Miyake and Koketsu*, 2005; *Furumura and Hayakawa*, 2007).

To isolate the effect of local structure on seismic amplitudes, we remove the surface-wave geometrical spreading decay of $\sqrt{r}$ appropriate for laterally homogeneous medium. At each receiver, we average the peak amplitude within the periods 3, 4, 6 and 7 s, and show in the spatial variation of the relative amplitudes (Fig. 2.6). For reference, we contour every kilometer of the $V_S = 3.2$ km/s isosurface depth, and highlight the coastlines.

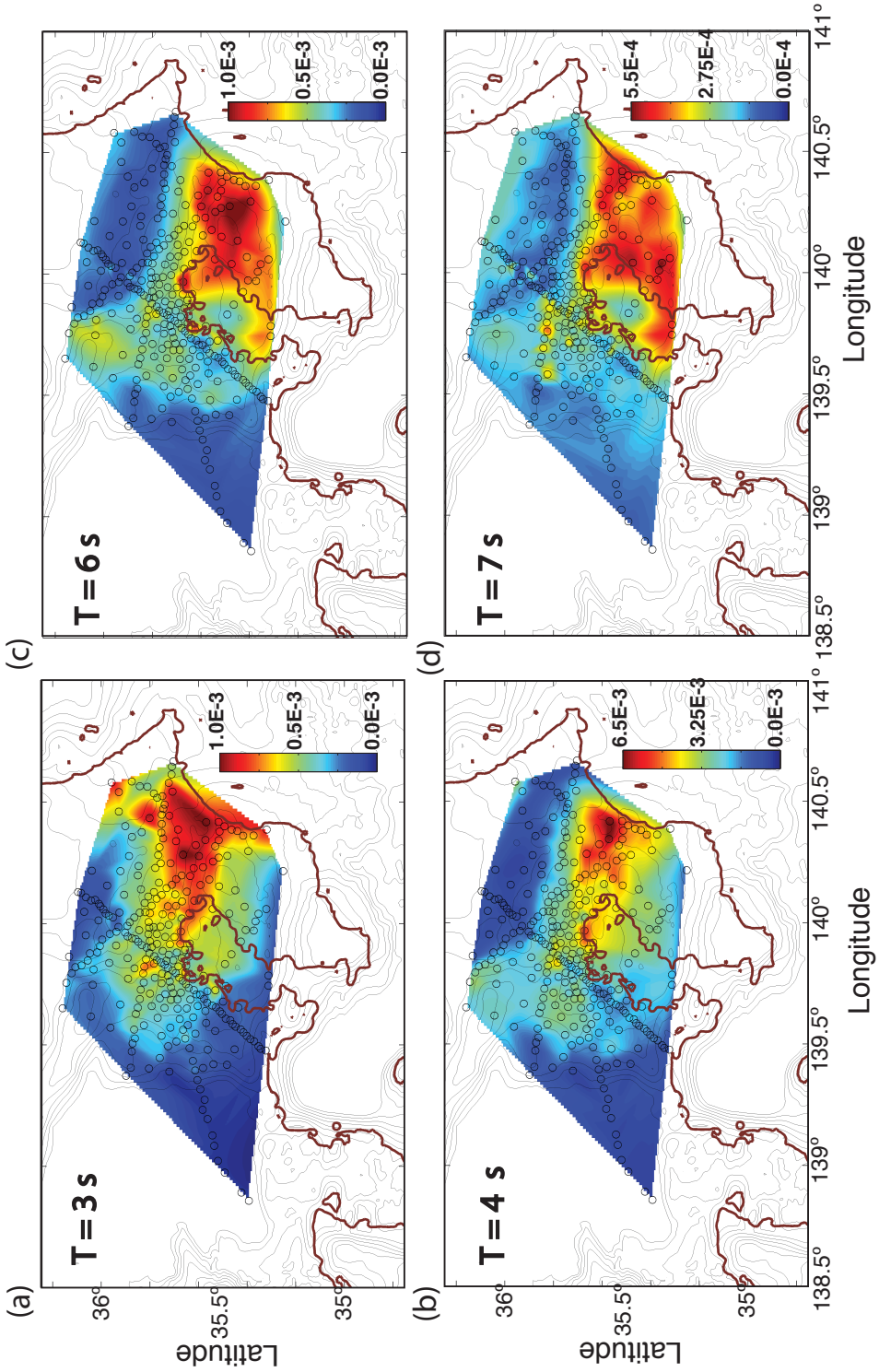

Figure 2.6: PGM amplitudes recorded in MeSO-net receivers (black solid circles), averaged over all Hi-net stations, bandpass filtered time series around the periods 3 s (a), 4 (b), 6 s (c), and 7 s (d). Brown solid lines are coastlines. Black solid contours are 1 km-spaced for the $V_S = 3.2$ km/s isosurface depth.

We find a positive correlation between PGM and depth of basement (Figure 2.6). The basin edge separates the low to high amplitude of the averaged PGM. The northern tip of the seismic network is situated on top of a secondary sedimentary basin, that we refer to as Saitama Basin. This basin may play a major role in channeling seismic waves from Niigata into Kanto Basin (*Furumura and Hayakawa*, 2007), and we see its clear resonance around 5 and 6 s (Fig. 2.6 (b-c)). The long periods 6-7 s are more strongly excited where the sedimentary basin is the deepest, whereas the shorter periods 3 – 4 s seismic waves seem to focus under Narita. There is asymmetry in the excitation of the basin, with stronger shaking expected on the eastern side, but we propose that these effects arise from seismic directivity as most of our virtual sources are located on the western side of Kanto.

The margins of Tokyo Bay seem most affected in seismic amplification across all frequencies, which could be explained through the low impedance of the unconsolidated deposits. It is interesting to note the correspondence between the high amplitude patch on the western flank of the bay with the area where seismic waves that are diffracted and reflected on the basin edge constructively focus (*Furumura and Hayakawa*, 2007). Polarization measurements from the horizontal components of the Green's tensor should provide new insights to test this supposition.

A simple way to account for the effect of basins on ground motion is to correlate the observed peak amplitudes with the thickness of the sediments. *Day et al.* (2008) proposed a spectral response model with respect to the sediment thickness that motivated a parametrization of basin effects in the Ground Motion Prediction Equations (GMPEs). We use the function that accounts for basin response from *Campbell and Bozorgnia* (2013) to predict its contribution to each period of the PGM:

$$log10(PGM(T)) = \begin{cases} (c_{14}(T) + c_{15}(T))(Z_{2.5} - 1) & ; \quad Z_{2.5} \leq 1 \\ 0 & ; \quad 1 < Z_{2.5} \leq 3 \\ c_{16}(T)k_3(T)e^{-0.75}\left[1 - e^{-0.25(Z_{2.5}-3)}\right] & ; \quad Z_{2.5} \geq 3 \end{cases}, \tag{2.2}$$

where the coefficients c_{14}, c_{15}, c_{16}, and k_3 depend on the period T, $Z_{2.5}$ is the $V_S = 2.5$ km/s isosurface depth. *Campbell and Bozorgnia* (2013) find the GMPE parameter

by fitting the predicted horizontal ground motion with recorded shaking intensities.

We narrow pass filter the time series around the periods of interest and show in Figure 2.7(a) the mean peak amplitudes (logarithmic base 10 scale) against the V_S = 2.5 km/s isosurface depth at each site (as provided by the integrated velocity model). We plot the expression of equation 2.2 with the coefficients found in (*Campbell and Bozorgnia*, 2013), and we plot the same function with the coefficients that best fit our data, but reduced to three degrees of freedom. We see that the GMPEs fit well our data for the period of 5 s and 7 s, but we see strong disagreement in the slopes used in the GMPE. Finally, we can represent the variation with a simple linear relation:

$$log10(GMP(T)) = a(T)Z_{2.4} + b(T), \tag{2.3}$$

where we show the best fit slope and constant in Figures 2.8(b) and 2.8(c) respectively. We see clear decay of the ground motion amplitude with period, but a variable scaling that peaks at 6 s (Fig. 2.8(a)), period at which we also minimize the root-mean-squares of the residuals.

Our results suggest that amplification systematically increases with basin depth. We note additionally that the simulations of ground motion in the Los Angeles Basin show an increase of the amplification effect with increasing period up to the natural period of the Los Angeles Basin at 8 s *Day et al.* (2008). This connects well with our results on the Kanto Basin with its natural resonance of 5 – 7 s.

We show that the surface-to-surface impulse responses extracted from the ambient seismic field are strongly affected by sedimentary basins and that we retrieve effects that were observed in the Niiagata-Chuetsu earthquakes and tier ground motion simulations (*Furumura and Hayakawa*, 2007). Earlier in this study, we found that the incidence of the surface-waves, or more precisely where the source is located, produced drastically different shaking intensity. We take advantage of the density of the Hi-net seismic network to locate potential earthquake sources that would most affect strong shaking in Kanto Basin.

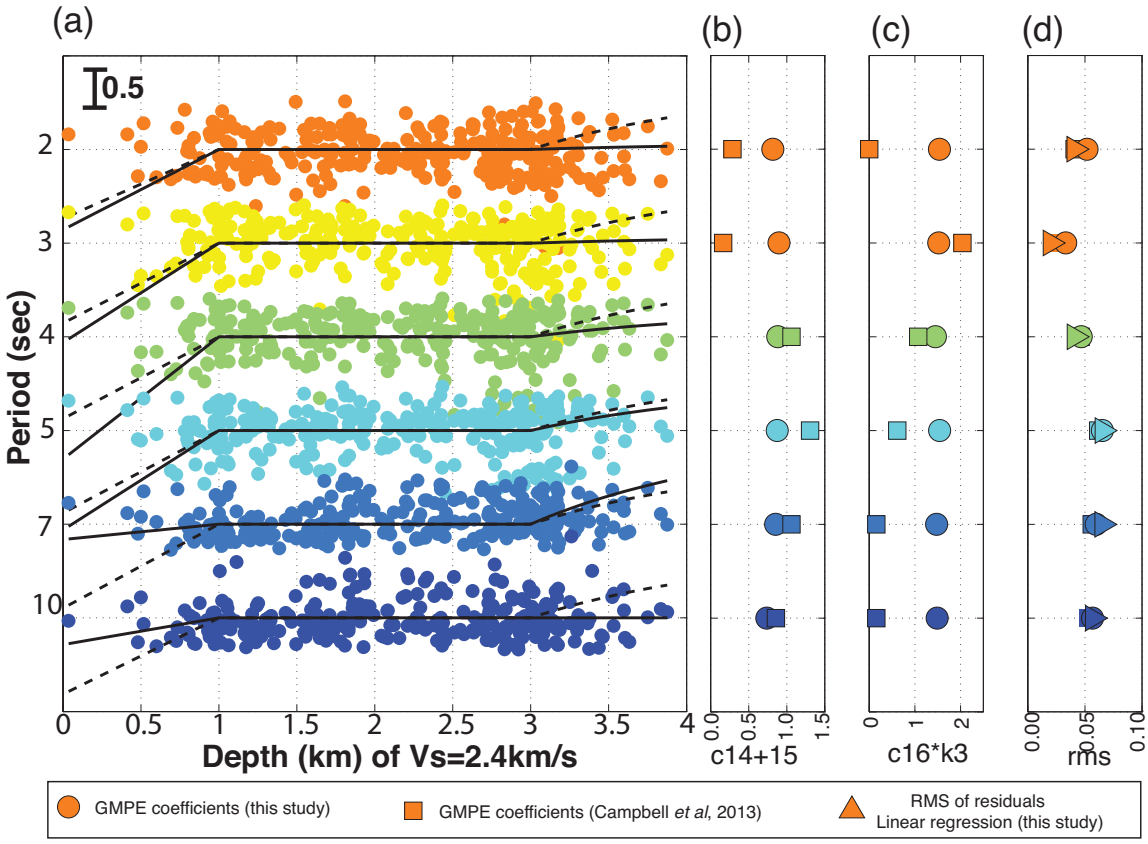

Figure 2.7: Basin term in GMPE (*Campbell and Bozorgnia*, 2013) against the V_S = 2.4 km/s isosurface (x-axis) for the periods 2, 3, 4, 5, 7 and 10 seconds. We color and shift the data sets to separate the measurements from each period for clarity. (a) Similar as in Figure 2.7(a), dashed lines are the scaled GMPE (*Campbell and Bozorgnia*, 2013), solid lines are the GMPE with best-fit coefficients. (b)-(c) coefficients for Japan against period for our study (solid circles) and *Campbell and Bozorgnia* (2013) (solid squares). (d) Root-mean-square (rms) of the residuals for the linear fit (solid triangles), our best-fit coefficient (solid circle), *Campbell and Bozorgnia* (2013) coefficient (square circle).

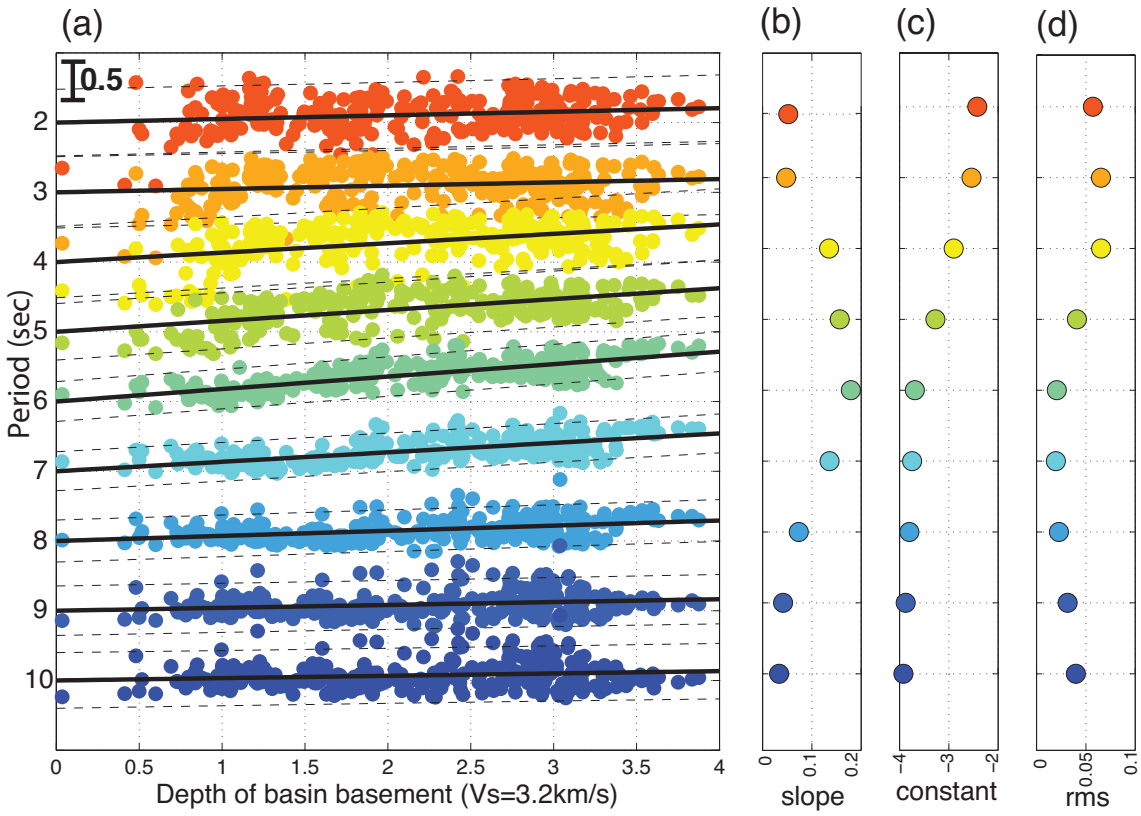

Figure 2.8: Linear fit of ground motion with sediment thickness. (a) Peak amplitude measured against thickness of the V_S = 2.4 km/s (x-axis) below each receiver with time series narrowly filtered around the periods 2 to 10 s (y-axis), and color coded by period. Solid lines are the best-fit line within the 95% confidence (dashed lines). (b) Best-fit slope for each period. (c) Best-fit constant (log10 of background level of ground motion). (s) root-mean-square (rms) norm of the residuals.

Amplification Hazard

If the Earth's structure were laterally homogeneous, earthquakes located at equal distance from a receiver would produce identical shaking intensity, and amplitudes would decay monotonically with distance from the source. Instead, we see strong variations of ground motion from sources equidistant from Kanto. Figure 2.9 depicts the peak ground motion measured from virtual sources located 150 to 200 km away from the center of the MeSO-net array. From the North-East corner, the blue colored shaking indicates low amplitudes, and moving counter-clockwise, this low intensity is

expected from sources to the west until Niigata region. To the WNW, as we enter the Nagano Prefecture, the sources produce significantly stronger shaking in Tokyo (KMDH, SSWH, SUYH). The level of shaking from southern sources (TGKH and HWKH) then decays to have level similar to the sources close to the north.

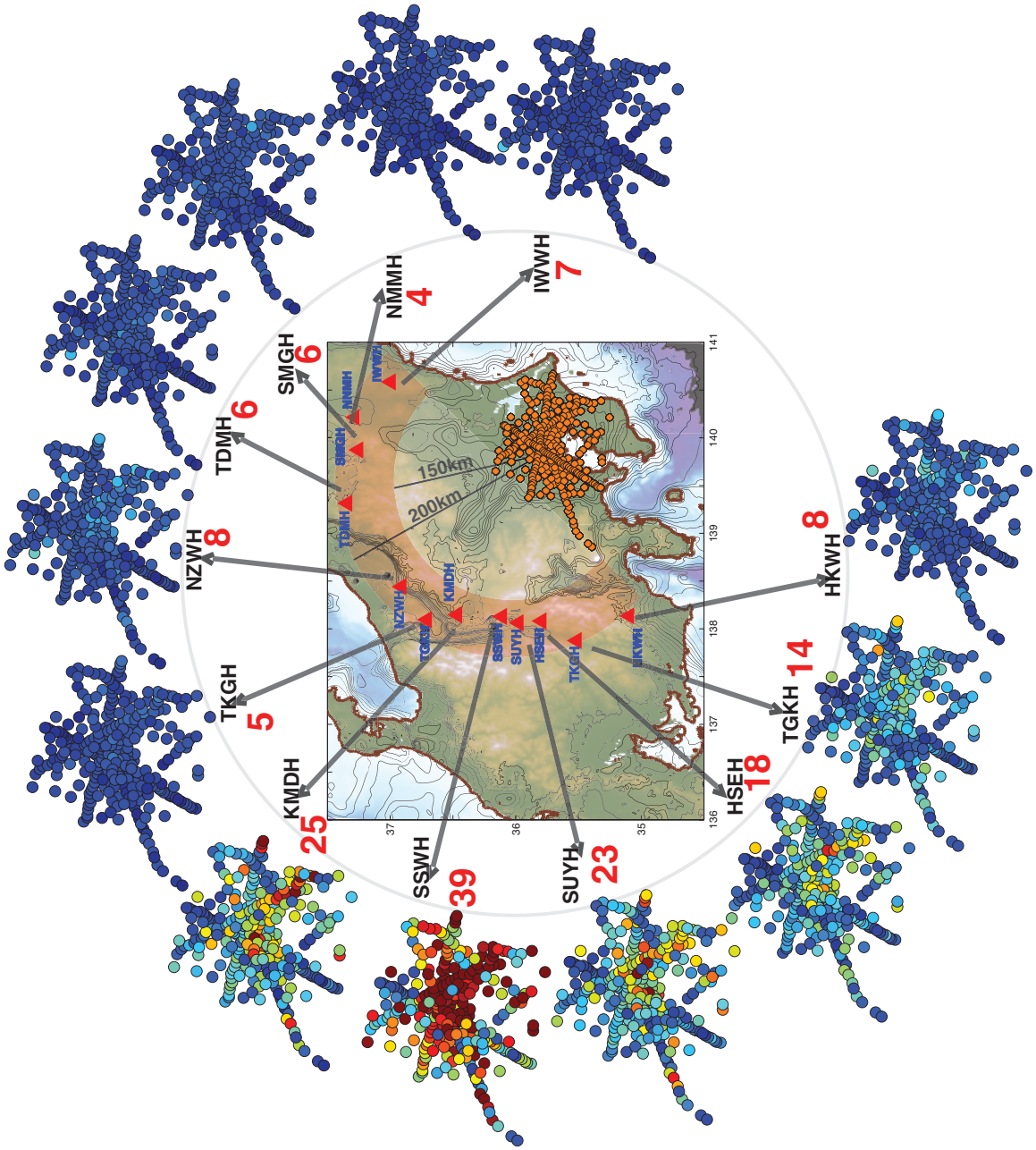

Figure 2.9: Peak ground motion maps for far-field sources. Depth of isosurface $V_S = 3.2$ km/s contoured every kilometer (solid black thin lines). Seismic station maps of MeSO-net receivers (orange circles) and Hi-net virtual sources (red triangles) within a range of 150 – 200 km. Scatter map of peak ground motion at individual receivers color scaled from low to strong shaking (blue to red), and relative peak amplitude scaled by 10^{-4} (red numbers).

We note that the NZWH station is the closest to the 2007 M6.8 Chuetsue epicenter, but we do not see the strong amplification effect observed in Kanto Basin. It is possible that this result from the lack of body- to surface-wave conversion mentioned in *Furumura and Hayakawa* (2007) in our Green's function at the virtual source location.

The sources located in the Mastumoto area are intriguing since they are located on bedrock. The northern Kanto Basin extends with a shallower expression toward the Nagano area, which could explain channeling of the seismic waves from Nagano events into Kanto Basin. This expression of complex wave paths needs to be further investigated. Simulations should provide important additional information.

We now attempt to locate the sources that strongly affect the amplification, not only with azimuth, but in more a general way, across Honshu. This is similar to source imaging, where we search for locations on the fault that generate most of the seismic energy. We separate regions in Kanto and define 20 km $\times$ 20 km bins for which we form a cluster MeSO-net receivers. In each bin, we retain the PGM from the Green's functions filtered 2 – 10 s, predicted by sources that are at least 30 km away.

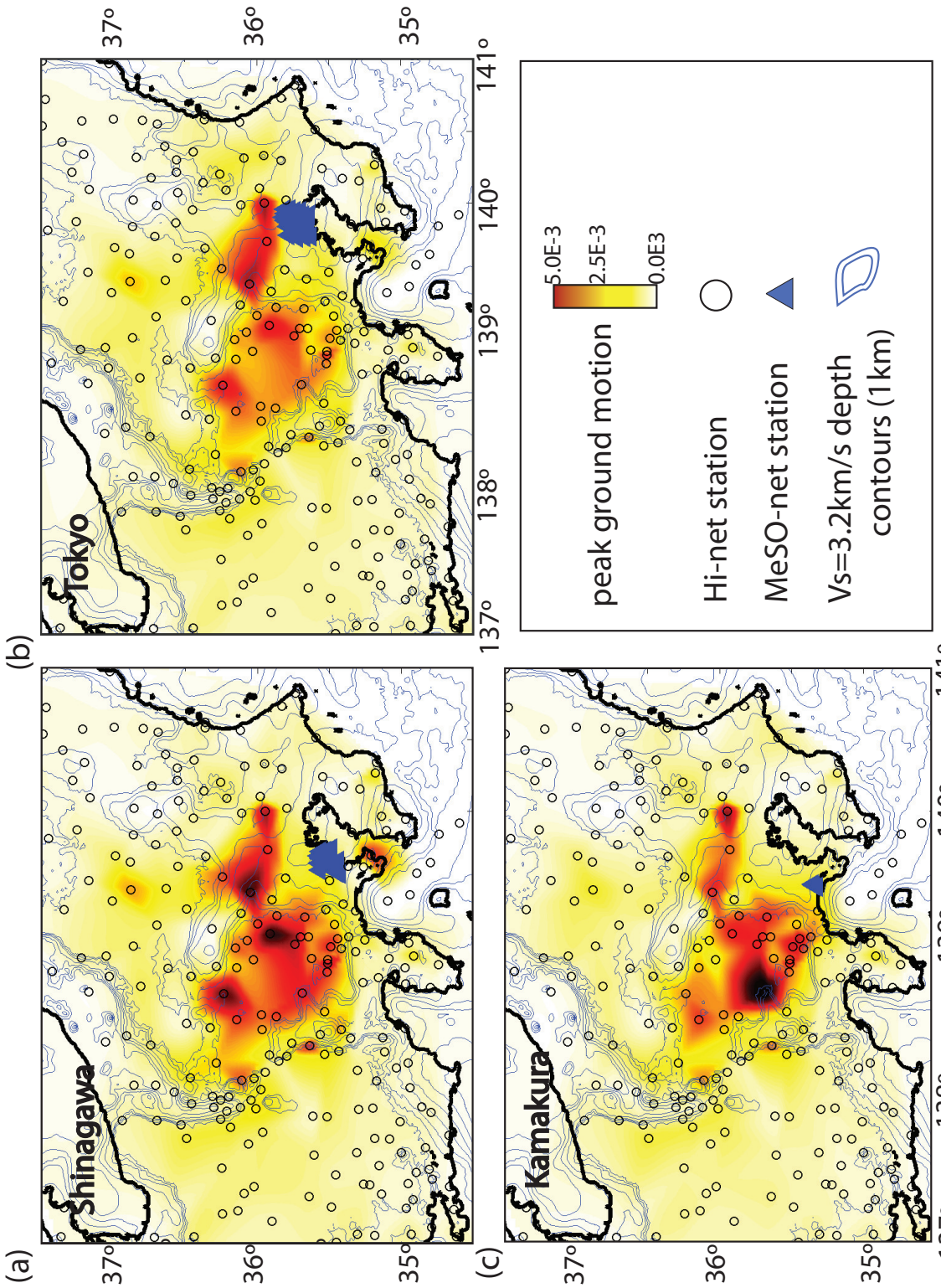

Figure 2.10: Shaking potential of individual virtual sources (solid circles) to areas in Kanto. Color scale ranges from zero (white) to maximum PGM measured (red) in the frequency band 2 – 10 s.

Figure 2.10 is a reciprocal representation of Figure 2.9, but it represents the sensitivity for Kanto. For each sub region, we first average the peak amplitude for a given source, to all receivers within that region. We then attribute a color to the shaking potential of each source to that particular region that we interpolate in between virtual sources (Fig. 2.10). We draw the contours of the $V_S = 3.2$ km/s isosurface for reference.

Our results correlate with Figure 2.9 where we see the Suwa stations highlighted by hot colors. The dominant "bright spot" interestingly is located in the mountainous regions of western Saitama and eastern Yamanashi prefectures, East Nagano, and Shinagawa and Kamakura, probably from being closer to Tokyo. No active fault has yet been mapped in this area (*AIST*, 2012).

All things being equal, West Honshu has stronger shaking potential in Kanto than the East Honshu for shallow earthquakes. Surprisingly, the surface-wave amplitudes retrieved from the ASF Green's functions are enhanced when traveling through the sharper edge of the sedimentary basin (see Figure 2.1). To first order, the transmitted waves from fast-to-slow material will have a larger amplitude than the incident wave, simply due to impedance contrast. *Furumura and Hayakawa* (2007) propose that the basin edge strongly scatters and refocuses seismic waves coming from the North into central Tokyo. We propose that the scattering of surface-waves traveling through this sharp interface explains the increased seismic amplification.

Amplification due to basin-edge effects.

We have shown that the Earth's structure greatly affects seismic-wave propagation, but we have so far only considered forward scattered wave propagation, and neglected any phase conversion or reflections. With the strong variations in wave speed along direct wave paths, such as the one expected at the western basin edge (Fig. 2.1), we might anticipate the conversion of body waves to surface waves. *Kawase* (1996) and *Pitarka et al.* (1998) explained the intense ground motion in the Hyogo-ken Nanbu, M6.9 1994 Kobe earthquake with phase conversion at the edge of the Osaka sedimentary basin. *Graves et al.* (1998) simulate horizontal S-waves traveling across

the Santa Monica Fault into the Los Angeles Basin that partially convert to Love waves, and show that the horizontal components are more efficiently excited at the basin interface than vertical components. Ground motion mat also be amplified by the interference of the direct body waves and diffracted surface waves, depending on the angle between the incoming wave and the bedrock-basin interface (*Adams*, 2000). Although we have not yet recovered the horizontal components from the ASF Green's functions, the patterns of complex wave propagation we observe suggest possible reflection, phase conversion, and even the presence of body waves.

The Kanto Basin is known for its unconsolidated sediments with very low wave speed that is contrasted with a stiff, high velocity, bedrock at its base. This enhances dispersion of surface waves, and, by doing so, extends the duration of shaking at larger distances. We solve the surface-wave excitation using the Generalized Eigenproblem Spectral Collocation method (*Denolle et al.*, 2012), and given velocity profile extracted from the velocity model (*Koketsu et al.*, 2009). We then computes the synthetic surface-wave vertical-to-vertical component of the Green tensor (*Aki and Richards*, 2002) for receivers evenly spaced from 0 to 200 km away from a point source. We show in Figure 2.11 the normalized Green's functions, illustrate a simple case of strong dispersion, and show examples of extended shaking in the far-field. Note that this duration is only due to the sediment structure in a 1D profile, and that we have not yet considered the 3D basin effect in wave propagation.

We show in Figures 2.12, 2.13, and 2.14 a few example of the ASF Green's functions from all MeSO-net receivers according to the source-receiver distance. We see strong dispersion for the Green's functions, as expected from the sediment structure (Fig. 2.12). We also see early an arrival that is non-dispersive and approximately twice as fast as the later wave train, that is highly dispersed and has higher frequency content. We believe that the fast (wave speed $\sim$3 km/s), and non dispersive arrivals are body waves, and we anticipate measuring their polarization using the horizontal components of the Green tensor will support this conjecture.

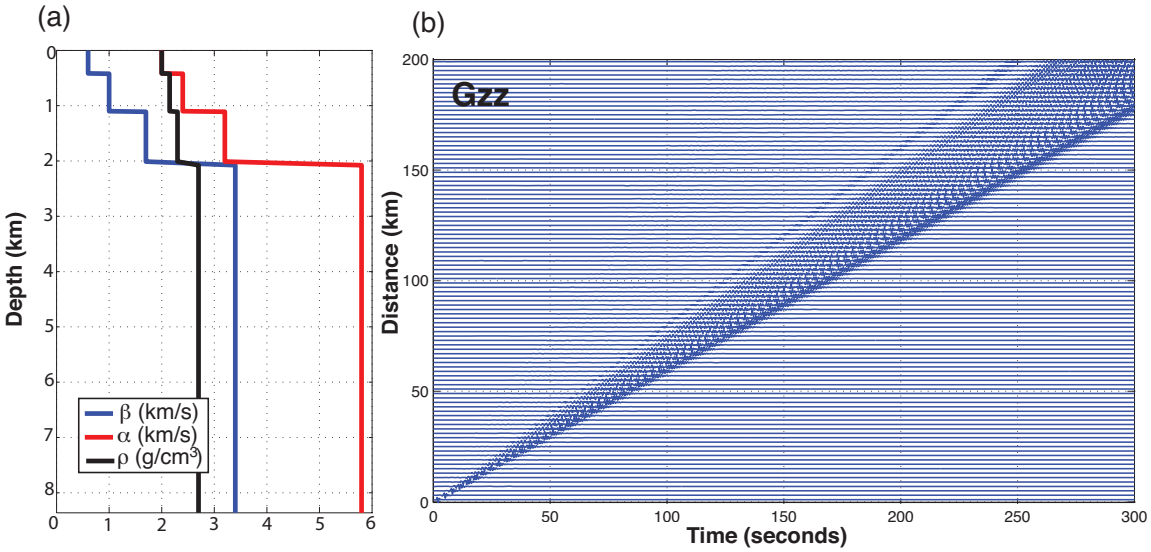

Figure 2.11: (a) Velocity and density profile underneath central Kanto. (b) Synthetic ZZ Green's functions evaluated at distances from 0 to 200 km.

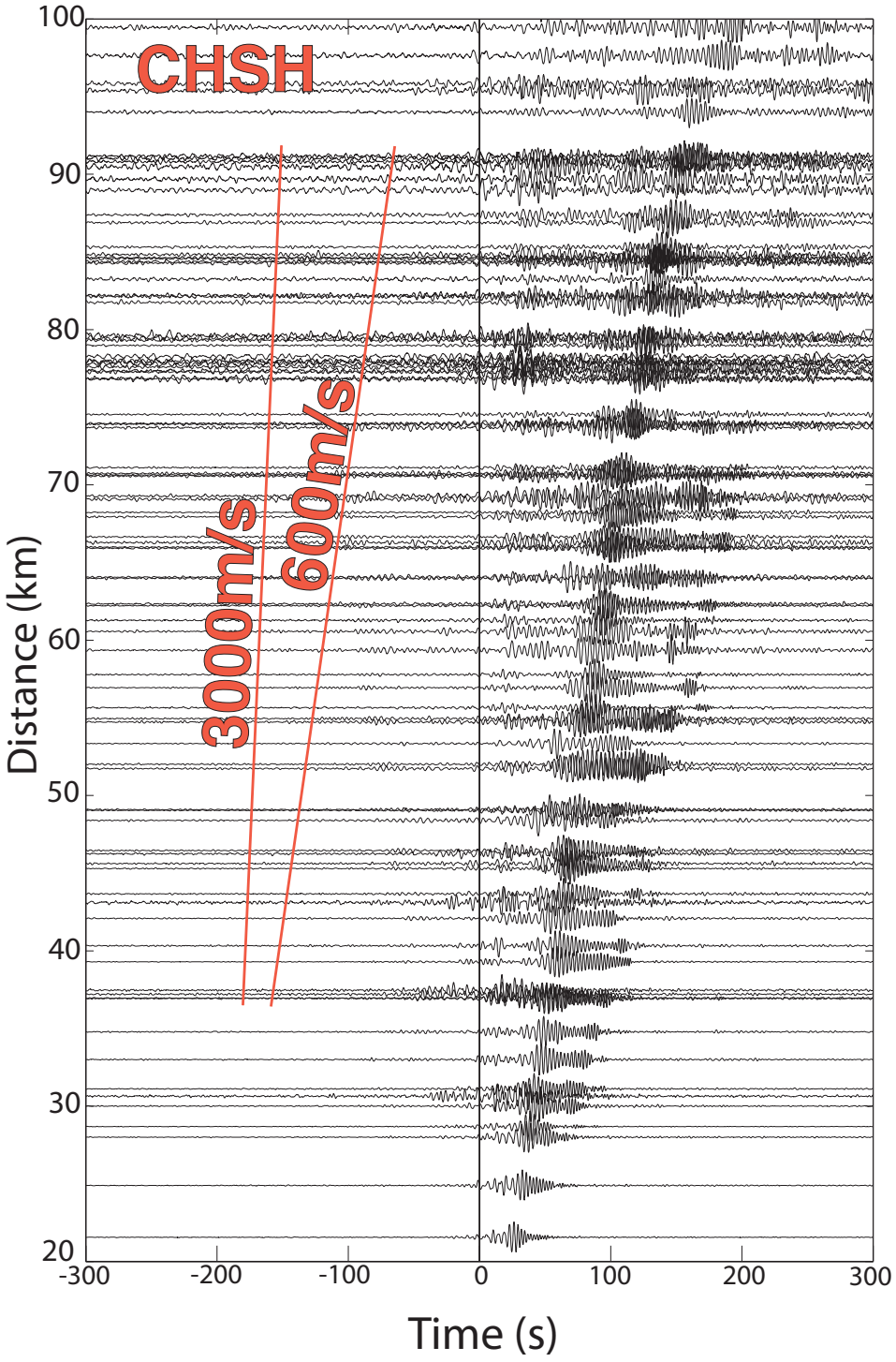

Figure 2.12: Evidence for recovering direct body waves from CHSH Hi-net source (see location in Figure 2.15).

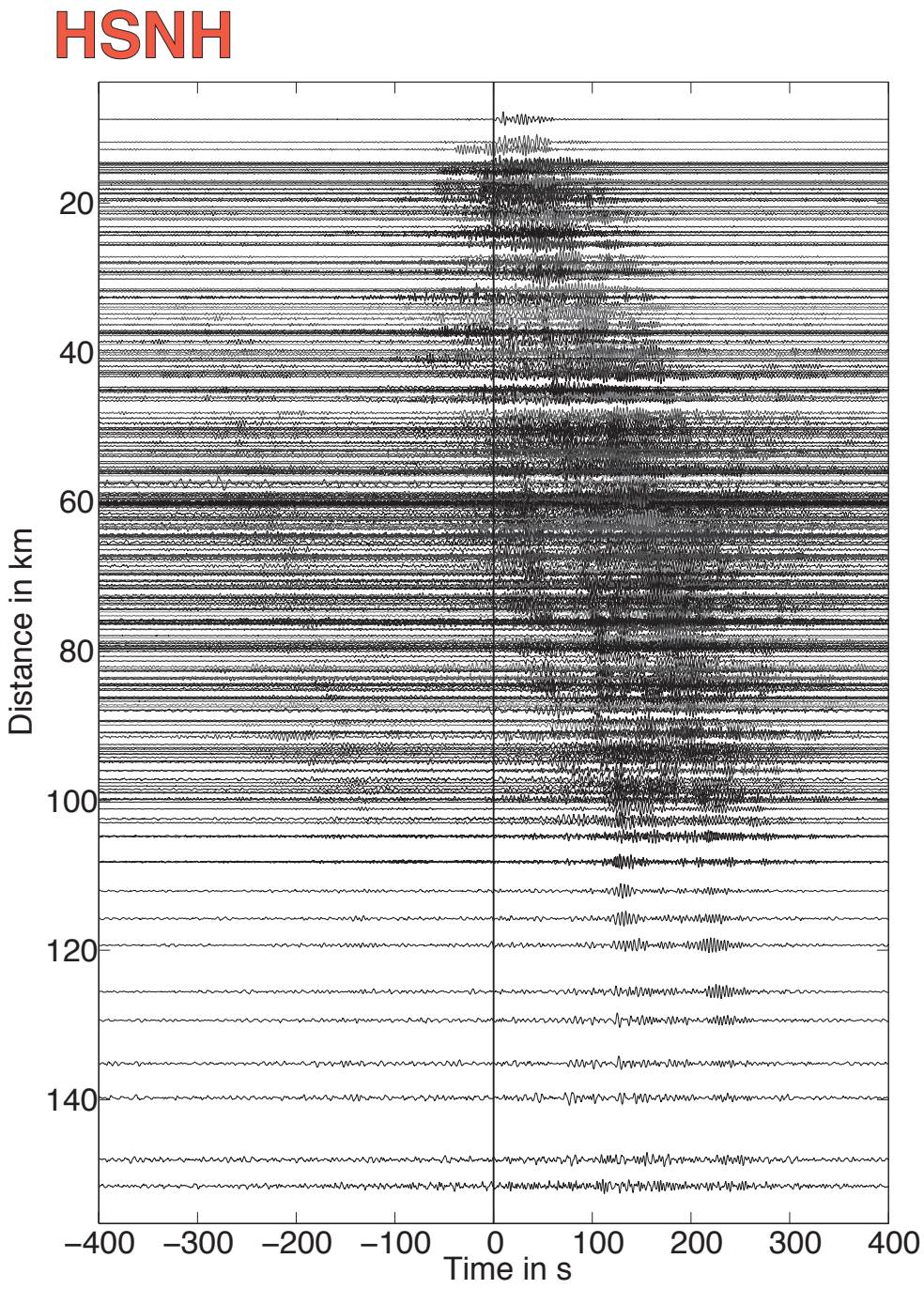

Figure 2.13: Evidence for reflection of surface waves onto the basin edge from HSNH Hi-net source (see location in Figure 2.15).

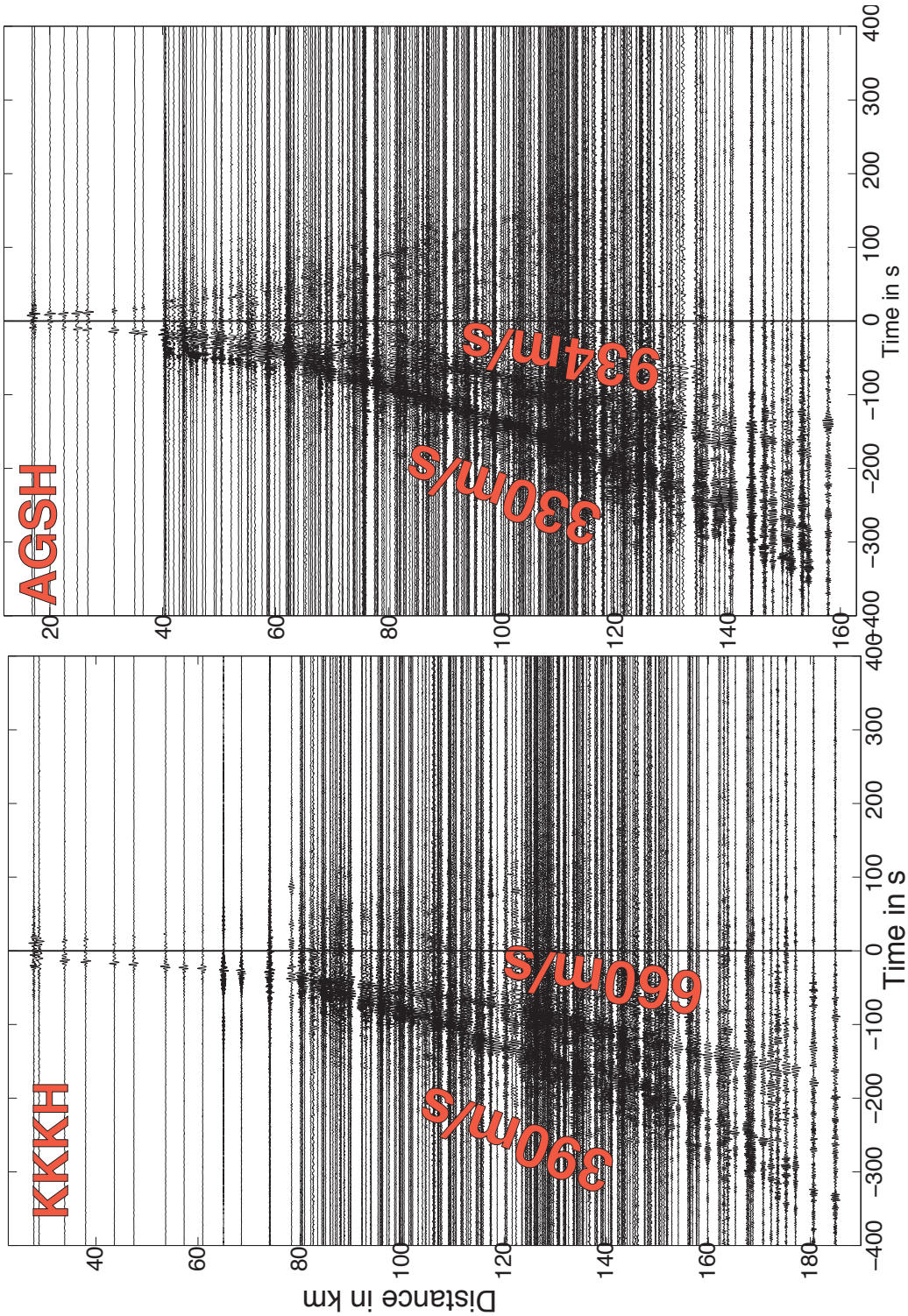

Figure 2.14: Evidence for conversion of surface waves to body waves from KKKS and AGSH Hi-net sources (see location in Figure 2.15).

A source located at HSNH station, on the coast of Chiba Prefecture, produces fascinating waveforms (Fig. 2.13). We see three distinct wave packets. The earliest arrivals seem to propagate with approximate wave speed of 1.5 km/s and are impulsive. In contrast, the latest arrival is highly dispersed and has an approximate group velocity of 500 m/s. Most importantly, we note the small amplitude, but nonetheless very clear, reflected wave that propagates in the opposite direction at distance 100 km from the virtual source. This wave is also apparent in the anti-causal fields.

Finally, we highlight an intriguing expression of complex wave propagation that only appears for specific source-receiver paths (Fig. 2.14) that suggests the presence of phase conversions. KKKH and ASGH Hi-net stations are located on the western end of the MeSO-net array and are located on bedrock. We observe fast and clean arrivals close to the sources, within 80 and 40 km respectively. We propose that the incident surface waves split between two main strands that we interpret as being S_V or P waves for the fastest train, and Rayleigh waves for the slow and dispersed wave train.

Both the phase conversion and the reflection pattern are observed for additional source-receiver paths. Since we know the location of each source and each receiver (or their respective source-receiver distance), we estimate the location of this effect by picking a source-receiver range within which we see the effect. We count the number of times we pick a specific location, i.e. a station receiver, and we show in Figure 2.15 the cumulated number of hits. We overlay the contours of the basement (V_S = 3.2 km/s isosurface depth). The sites that were counted numerous times are directly located above the edge of the sedimentary basin. This clearly confirms the hypothesis that surface-waves strongly interact with the basin edge.

Conclusions

In this study, we have laid the foundations of an analysis using the ambient seismic field to characterize seismic wave amplification in Kanto Basin by combining both MeSO-net and Hi-net dense seismic networks.

We have built peak ground motion maps at different frequency bands and related

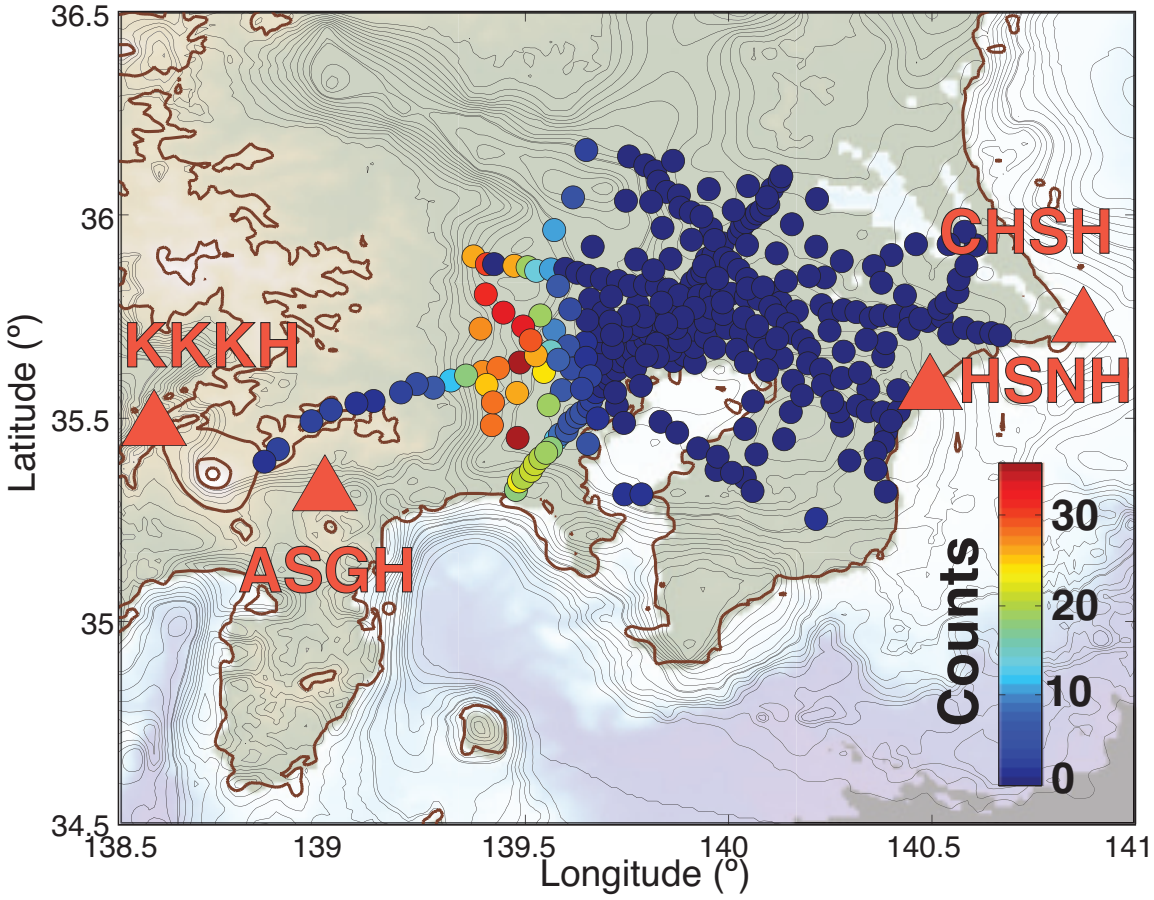

Figure 2.15: Map showing probability density function of basin edge measured from picking the conversion point highlighted in the red circle.

the spectral characteristics of the ground motion to basin structure and shallow geomorphology. We also constructed a simple linear relation to predict the variation of shaking intensity with sediment thickness. We believe the Ground Motion Prediction Equations would benefit from incorporating the ambient seismic field Green's functions as an independent data set to predict long period ground motion.

The pattern of seismic amplification due to complex wave propagation effects outside of Kanto Basin is puzzling. We have identified the virtual sources that should produce stronger shaking in Kanto and found that they are located in the Suwa Basin in Central Honshu, where several strike slip and thrust M7+ earthquakes have occurred in the past. The resulting ground motion produced in Kanto results from complex wave paths that we suspect dare enhanced by the presence of the northern Kanto Basin trend that channeled seismic waves. This was hypothesized to explain observation during the Niigata-Chuetsu earthquakes (*Furumura and Hayakawa*, 2007). There are about permanent 23 Hi-net stations deployed above a fault that hosted M7+ earthquakes, which suggest that they could be used to construct virtual earthquakes of that magnitude. Obvious future work is to generalize this approach and to establish a data base of scenario earthquakes for all active faults of Honshu that are close to Hi-net stations. Ultimately, this could enable a new approach to Probabilistic Hazard Seismic Analysis for long-period ground motion.

Finally, we measure much more complex wave propagation effects than anticipated. The basin edges are found to greatly contribute to strong ground motion as they cause phase conversion and, in particular, interference between surface and body waves in the basin. Moreover, the impedance contrast between bedrock and basin medium acts as a mirror for waves in the basin so that seismic waves reflects from its boundary. With the ASF vertical Green's functions, we see clear evidence of phase conversion at the sharp sedimentary basin western edge of Kanto Basin. We hypothesize the conversion Rayleigh and Sv waves that we suspect from the first order measurement of move-out. Targeted future studies will incorporate horizontal components, known to be the most sensitive to basin-edge features and to convert to Love waves.

This study is an example of the extraordinary potential of dense seismic networks

for characterizing seismic hazards in an urban environment. Specifically, our results highlight the power of using virtual earthquakes from correlation of the ambient seismic field, to compensate for the lack of data, and exploit the available seismic networks to investigate basin amplification effects for large earthquakes.

Chapter 3

Surface-wave Excitation

Introduction

Seismic waves in the Earth are modeled as elastic waves, and to first order the Earth can be approximated as a 1-D medium because the depth variations of elastic properties are much stronger than horizontal variations. In this study we focus on surface wave solutions only. Neglecting lateral variations in material properties, the elastic wave equation in the frequency and horizontal-wavenumber domain takes the form of an eigenproblem in the absence of sources. This problem has been solved by a variety of methods, beginning with the propagator-matrix approach of *Thomson* (1950) and *Haskell* (1953). The propagator matrix technique begins with the assumption of a layered medium with spatially uniform elastic properties within each layer. The original method is known to suffer from instabilities at high frequencies (*Ewing et al.*, 1957). Since these methods were introduced, seismologists have devised a number of approaches for obtaining accurate and stable solutions at high frequencies, including the delta matrix method (*Pestel and Leckie*, 1963; *Watson*, 1970; *Buchen and Ben-Hador*, 1996), the Schwab–Knopoff approach (*Knopoff*, 1964; *Schwab and Knopoff*, 1971), and the R/T matrix method (*Kennett*, 1974; *Kennett and Clarke*, 1979; *Kennett*, 2009; *Pei et al.*, 2008).

In addition to the propagator matrix technique, the eigenvalue problem can also be solved using the shooting method. This is more accurate but can be computationally inefficient since it involves multiple iterations to satisfy all boundary conditions and to isolate particular eigenmodes (*Takeuchi and Saito*, 1972; *Dahlen and Tromp*, 1998). Another class of methods is based on directly approximating the eigenfunctions as a finite sum of polynomials or other special functions, with coefficients determined by minimizing appropriately defined residual functions. Galerkin finite element methods like those developed by *Lysmer* (1970) fall into this class, as do collocation methods. It is even possible to design hybrid methods that utilize both propagator matrix and collocation techniques (*Spudich and Ascher*, 1983; *Ascher and Spudich*, 1986).

In this chapter, we focus on the surface-wave component of the seismic wavefield, and treat the coupled system of equations as an eigenproblem, where the eigenvalues

(wavenumbers) and eigenfunctions comprise the surface-wave modes. We follow *Kirrmann* (1995) and recast the system of ordinary differential equations in the depth variable z into an equivalent linear eigenproblem in standard form,

$$\mathbf{L}\mathbf{u} = k\mathbf{u}, \tag{3.1}$$

for wavenumber k and a linear differential operator $\mathbf{L}$ involving d/dz and frequency ω. The eigenvector $\mathbf{u}$ contains the displacement fields and certain components of the stress tensor as a function of depth z. The stress tensor components that enter $\mathbf{u}$ are different than those in the standard stress-displacement vector. The eigenproblem also requires appropriate boundary conditions.

We discretize the problem (Eq. 3.1) by seeking values of $\mathbf{u}$ at a finite set of points, and convert the linear operator $\mathbf{L}$ into a matrix using a difference operator $\mathbf{D}$ to approximate the depth derivative d/dz. Boundary conditions are directly incorporated as constraint equations on the point values of $\mathbf{u}$ and $d\mathbf{u}/dz$ on the boundaries. This yields a generalized matrix eigenvalue problem,

$$\mathbf{A}\mathbf{u} = k\mathbf{B}\mathbf{u}, \tag{3.2}$$

where $\mathbf{A}$ and $\mathbf{B}$ involve $\mathbf{D}$, and are singular (preventing us from rewriting (Eq. 3.2) as a standard eigenvalue problem). Numerical solution of the finite-dimensional eigenvalue problem is straightforward and directly yields all resolvable eigenmodes.

If we discretize this problem using N points with a standard finite-difference (FD) scheme, it converges for sufficiently smooth solutions with error that decreases as N^{-p}, where p is the FD order of accuracy. We have found low-order FD methods to be computationally intensive with unreasonably large values of N required for an accurate solution. Instead we use a Chebyshev spectral collocation method that converges faster than N^{-p} for any p for smooth functions. Spectral accuracy is still possible in the presence of discontinuous material properties, provided the domain is split at material interfaces into multiple layers (within which properties are smoothly varying). Each layer is separately discretized and fields on the two sides of the layer interface are coupled with appropriate continuity conditions.

We first show how to recast the eigenproblem in standard form. We then show that a spectral collocation discretization greatly improves accuracy and efficiency relative to finite difference methods. We refer to this optimal combination as the Generalized Eigenproblem Spectral Collocation (GESC) method.

We verify the accuracy of our results against known analytical solutions for simple cases, and against well-established methods (*Herrmann*, 1978) for more complex media. Once verified, we apply our method to solve for the surface-wave response of the southern California crust as represented by a local profile of the SCEC Community Velocity Model (CVM) (*Magistrale et al.*, 2000; *Kohler et al.*, 2003), and investigate the cases where the Rayleigh wave surface particle motion transitions between retrograde to prograde. Our method is both efficient and general and does not suffer from instabilities at high frequency. It is more flexible than other approaches because it allows a combination of homogeneous layers, continuous gradients, discontinuities in material properties, and directly gives all surface-wave modes with no iteration needed to satisfy boundary conditions or isolate particular modes.

Formulation of the eigenproblem

We combine Hooke's law and the momentum balance for an elastic solid with depth-dependent properties to derive the eigenproblem in the Fourier domain. In cylindrical coordinates (r, ϕ, z), we seek a solution of the specific form (*Aki and Richards*, 2002):

$$\mathbf{u} = \left[r_1(k,z,\omega)\mathbf{S}_k^m(r,\phi) + l_1(k,z,\omega)\mathbf{T}_k^m(r,\phi) + ir_2(k,z,\omega)\mathbf{R}_k^m(r,\phi) \right] e^{-i\omega t}, \qquad (3.3)$$

where $\mathbf{u}$ is the displacement field, z is the depth coordinate, ω is the frequency, and

$$\begin{aligned} \mathbf{T}_k^m(r,\phi) &= \frac{1}{kr}\frac{\partial Y_k^m}{\partial \phi}\mathbf{e}_r - \frac{1}{k}\frac{\partial Y_k^m}{\partial r}\mathbf{e}_\phi, \qquad (3.4) \\ \mathbf{S}_k^m(r,\phi) &= \frac{1}{k}\frac{\partial Y_k^m}{\partial r}\mathbf{e}_\mathbf{r} + \frac{1}{kr}\frac{\partial Y_k^m}{\partial \phi}\mathbf{e}_\phi, \\ \mathbf{R}_k^m(r,\phi) &= -Y_k^m\mathbf{e}_z. \end{aligned}$$

The unit vectors of the cylindrical coordinate system are $(\mathbf{e}_r, \mathbf{e}_\phi, \mathbf{e}_z)$; the scalar displacement functions are $r_1(k,z,\omega)$, $l_1(k,z,\omega)$, and $r_2(k,z,\omega)$; and $Y_k^m(r,\phi) = J_m(kr)e^{im\phi}$, with m the order of the Bessel function $J_m(\cdot)$ and k the horizontal wavenumber. The elastic medium is characterized by its density ρ and Lamé parameters λ and μ. The compressional and shear wave speeds are α and β. The equations governing Love and Rayleigh waves are

$$\begin{aligned} -\rho\omega^2 l_1 &= -\mu k^2 l_1 + \frac{d}{dz}\left(\mu \frac{dl_1}{dz}\right), \\ -\rho\omega^2 r_1 &= -k^2(\lambda+2\mu) r_1 - k\lambda \frac{dr_2}{dz} + \frac{d}{dz}\left(\mu \frac{dr_1}{dz}\right) - k\frac{d}{dz}\left(\mu r_2\right), \\ -\rho\omega^2 r_2 &= k\mu \frac{dr_1}{dz} - k^2 \mu r_2 - \frac{d}{dz}\left[(\lambda+2\mu)\frac{dr_2}{dz} + k\lambda r_1\right]. \end{aligned} \tag{3.5}$$

The standard approach to solve equation 3.5 is to define the stress-displacement vectors for Love waves as (l_1, l_2), where $l_2 = \sigma_{z\phi}$, and for Rayleigh waves as (r_1, r_2, r_3, r_4), where $r_3 = \sigma_{rz}$ and $ir_4 = \sigma_{zz}$.

In this work, we assume a traction-free boundary condition at the free surface $z = 0$ and vanishing displacement at the bottom of the domain. The latter is known in seismology as the locked mode approximation (*Harvey*, 1981). Equation 3.5 yields the Love-wave eigenproblem,

$$\frac{d}{dz}\begin{bmatrix} l_1 \\ l_2 \end{bmatrix} = \begin{bmatrix} 0 & \frac{1}{\mu} \\ k^2\mu - \rho\omega^2 & 0 \end{bmatrix}\begin{bmatrix} l_1 \\ l_2 \end{bmatrix}, \tag{3.6}$$

where $l_1 = 0$ at the bottom and $l_2 = 0$ at the free surface; and the Rayleigh-wave eigenproblem

$$\frac{d}{dz}\begin{bmatrix} r_1 \\ r_2 \\ r_3 \\ r_4 \end{bmatrix} = \begin{bmatrix} 0 & k & \frac{1}{\mu} & 0 \\ -k\frac{\lambda}{\lambda+2\mu} & 0 & 0 & \frac{1}{\lambda+2\mu} \\ k^2\frac{4\mu(\lambda+\mu)}{\lambda+2\mu} - \rho\omega^2 & 0 & 0 & k\frac{\lambda}{\lambda+2\mu} \\ 0 & -\omega^2\rho & -k & 0 \end{bmatrix}\begin{bmatrix} r_1 \\ r_2 \\ r_3 \\ r_4 \end{bmatrix}, \tag{3.7}$$

where $r_1 = r_2 = 0$ at the bottom and $r_3 = r_4 = 0$ at the free surface. The resulting

system can be written as $d\mathbf{f}/dz = \mathbf{P}(z)\mathbf{f}(z)$, where $\mathbf{f}$ is the displacement-stress vector, and we can solve this boundary value problem either by direct integration from the bottom to the surface (*Takeuchi and Saito*, 1972) or by the propagator matrix approach (*Haskell*, 1953). As written, the system is a quadratic, rather than a linear eigenproblem, because k is raised to the second power.

We propose a reformulation of the surface-wave eigenproblem that offers advantages over the traditional approach described above. We replace the stress functions l_2, r_3, and r_4 with

$$L_2 = k\mu l_1, \tag{3.8}$$

$$R_3 = k(\lambda + 2\mu)r_1 + \lambda\frac{dr_2}{dz}, \tag{3.9}$$

$$R_4 = \mu\frac{dr_1}{dz} - k\mu r_2, \tag{3.10}$$

where $\sigma_{r\phi} = iL_2$, and $\sigma_{rr} = iR_3$ and $R_4 = r_3 = \sigma_{rz}$.

The Love-wave eigenproblem becomes

$$\begin{bmatrix} 0 & \frac{1}{\mu} \\ \rho\omega^2 + \frac{d}{dz}\left(\mu\frac{d}{dz}\right) & 0 \end{bmatrix} \begin{bmatrix} l_1 \\ L_2 \end{bmatrix} = k \begin{bmatrix} l_1 \\ L_2 \end{bmatrix} \tag{3.11}$$

where $l_1 = 0$ at the bottom and $\mu dl_1/dz = 0$ at the free surface. The Rayleigh-wave eigenproblem becomes

$$\begin{bmatrix} 0 & -\frac{\lambda}{\lambda+2\mu}\frac{d}{dz} & \frac{1}{\lambda+2\mu} & 0 \\ \frac{d}{dz} & 0 & 0 & -\frac{1}{\mu} \\ \rho\omega^2 & 0 & 0 & \frac{d}{dz} \\ 0 & -\rho\omega^2 - \frac{d}{dz}\left(\frac{4\mu(\lambda+\mu)}{\lambda+2\mu}\frac{d}{dz}\right) & -\frac{d}{dz}\frac{\lambda}{\lambda+2\mu} & 0 \end{bmatrix} \begin{bmatrix} r_1 \\ r_2 \\ R_3 \\ R_4 \end{bmatrix} = k \begin{bmatrix} r_1 \\ r_2 \\ R_3 \\ R_4 \end{bmatrix} \tag{3.12}$$

where $r_1 = r_2 = 0$ at the bottom and $(\lambda + 2\mu)dr_2/dz + \lambda k r_1 = 0$ and $R_4 = 0$ at the free surface. If we include an internal layer interface, we must respect continuity of the displacements l_1, r_1, and r_2, and continuity of the traction components of stress $\mu dl_1/dz$, $(\lambda + 2\mu)dr_2/dz + \lambda k r_1$, and R_4.

Reduction to a generalized matrix eigenvalue problem

The left-hand side of equations 3.11 and 3.12 involve linear operators with depth-dependent elastic parameters and spatial derivatives. We convert this to a finite-dimensional generalized matrix eigenvalue problem using a collocation method. We solve for the eigenfunctions at $N+1$ collocation points within each layer (indexed by $i = 0, 1, \ldots, N-1, N$) by requiring that equations 3.11 and 3.12 be satisfied exactly at those points. We approximate d/dz with the $(N+1) \times (N+1)$ difference operator $\mathbf{D}$. For a field f with point values f_i, $(df/dz)_i = \sum_{j=0}^{N} D_{ij} f_j$.

To accommodate discontinuities in material properties, we layer the medium by placing internal interfaces at locations such that the eigenfunctions are smooth within the layers. Collocation points are placed on either side of an interface, and we enforce appropriate continuity conditions to relate fields on the two sides.

we incorporate the boundary and continuity conditions by removing rows of the matrix system and replace them by appropriate equations of constraint. We illustrate the technique for Love waves in a single layer. We adopt the convention that z is positive downward with $z = 0$ being the free surface, so that $i = 0$ is at the free surface and i increases with z until $i = N$ at the bottom. First, we discretize equation 3.11 as

$$\left(\begin{array}{c|c} \mathbf{0} & \boldsymbol{\mu}^{-1} \\ \hline \mathbf{D}\boldsymbol{\mu}\mathbf{D} + \boldsymbol{\rho}\omega^2 & \mathbf{0} \end{array}\right) \begin{pmatrix} u_0^L \\ \vdots \\ u_{2N+1}^L \end{pmatrix} = k \left(\begin{array}{c|c} \mathbf{I} & \mathbf{0} \\ \hline \mathbf{0} & \mathbf{I} \end{array}\right) \begin{pmatrix} u_0^L \\ \vdots \\ u_{2N+1}^L \end{pmatrix}, \tag{3.13}$$

where $\mathbf{I}$ is the $(N+1) \times (N+1)$ identity matrix, the vector $\mathbf{u}^L$ contains the Love-wave displacement and stress $(\mathbf{l}_1 \quad \mathbf{L}_2)$ sampled at the collocation points, and $\boldsymbol{\mu}$ and $\boldsymbol{\rho}$ are diagonal matrices of the depth-dependent shear modulus and density evaluated at the collocation points. The first $N+1$ rows correspond to Hooke's law at the $N+1$ collocation points, and the last $N+1$ rows are the momentum balance equation at the same points.

To introduce the boundary conditions at the free surface and the bottom, we remove entire rows of the system and replace these with constraint equations. At the

free surface ($i = 0$) we replace Hooke's law with the condition $\mu_{00} \sum_{j=0}^{N} D_{0j} u_j^L = 0$, where μ_{00} is the first element of $\boldsymbol{\mu}$. This replaces the first row in (3.13). At the bottom ($i = N$) we replace Hooke's law with the rigid-bottom condition $u_N^L = 0$. This replaces row $N + 1$ in equation 3.13. In the more general case of a layered medium, coupling conditions at layer boundaries are incorporated using a similar approach. Once boundary conditions have been implemented, the resulting matrices $\mathbf{A}$ and $\mathbf{B}$ are singular, making this a generalized eigenvalue problem. The problem is readily solved using the QZ algorithm (*Moler and Stewart*, 1973), which is implemented in Matlab's subroutine `eig` through an interface to the LAPACK library.

Discretization using a Chebyshev collocation method

The method described in the previous section can be implemented using any difference operator $\mathbf{D}$. A simple approach would be to use a standard low-order finite-difference approximation, for which error would decrease as N^{-p} for some small integer p. Instead, we use a Chebyshev spectral collocation method. Spectral methods are by far the most efficient when the solution is smooth, in which case they converge faster than N^{-p} for any p. Chebyshev collocation methods are an appropriate choice for problems on a non-periodic, bounded domain (*Trefethen*, 2000). The basic unknowns are the values of the fields at $N + 1$ collocation points. These values uniquely define a global degree N interpolation polynomial that can be used to evaluate the solution at any value of z. The interpolation polynomial can equivalently be written in terms of an expansion over the Chebyshev polynomials, but the method does not require solving for the coefficients of that expansion.

The collocation points are not evenly distributed over the interval; they are instead clustered near the boundaries. We first map the interval $z \in [a, b]$ to $\hat{z} \in [-1, 1]$ with the mapping $z = (a + b)/2 - \hat{z}(b - a)/2$. In this standard interval, the collocation points, $\hat{z}_n$, are the Chebyshev-Gauss-Lobatto points

$$\hat{z}_n = \cos\left(\frac{n\pi}{N}\right), \qquad n = 0, \cdots, N. \tag{3.14}$$

The differentiation matrix **D** for the Chebyshev method is well known and the difference operation can be efficiently implemented with an FFT-based algorithm (*Trefethen*, 2000).

Verification of the numerical method

In this section we compare the Chebyshev collocation solution to solutions for simple models consisting of layers of constant elastic properties. This allows us to gauge how many points are needed within each layer to obtain a desired accuracy.

Single layer case We first consider the simple case of a homogeneous finite-width layer with zero displacement at the bottom of the layer ($z = H$) and no traction at the surface ($z = 0$). The medium has constant elastic properties such as α for the P-wave speed, β for the S-wave speed and ρ for the material density. We calculate the true solution for this trivial case. For simplicity, we solve the system in a cartesian coordinate system, but similar results are obtained from a cylindrical framework. The Love-wave analytical solution for the wavenumber and eigenfunction is trivial, and for any mode n:

$$\begin{aligned} k_L^n &= \sqrt{\frac{\omega^2}{\beta^2} - \frac{\pi^2(n-1/2)^2}{H^2}} \\ l_1(z) &= \cos(\pi(n-1/2)z/H) \end{aligned} \tag{3.15}$$

We compare our numerical solution with the first five modes with this analytical formulation in Fig. 3.1. One approach to solve the Rayleigh-wave case is to derive the displacement fields from potentials. Using the notation $\eta_\alpha = \omega\sqrt{1/c^2 - 1/\alpha^2}$ and $\eta_\beta = \omega\sqrt{1/c^2 - 1/\beta^2}$ for P- and S-wave vertical slowness respectively, we write the potential as solutions to the wave equation:

$$\begin{aligned} \phi(z,k,\omega) &= (A_1\cosh(\eta_\alpha z) + A_2\sinh(\eta_\alpha z))\, e^{-ikx} \\ \psi(z,k,\omega) &= (B_1\cosh(\eta_\beta z) + B_2\sinh(\eta_\beta z))\, e^{-ikx}, \end{aligned} \tag{3.16}$$

where we calculate constants A_1, A_2, B_1, B_2 when satisfying the boundary conditions of vanishing displacement at the bottom of the layer $r_1(H) = r_2(H) = 0$ and zero traction at the surface $R_4(0) = \sigma_{zz}(0) = 0$. We derive the displacements from the potentials:

$$r_1(z) = \frac{\partial\phi}{\partial x} - \frac{\partial\psi}{\partial z} \tag{3.17}$$

$$r_2(z) = \frac{\partial\phi}{\partial z} + \frac{\partial\psi}{\partial x} \tag{3.18}$$

We incorporate equations 3.17 in equations 3.18 and express the boundary conditions to find the constants. The traction-free surface yields:

$$B_1 = \frac{2ik\eta_\alpha}{k^2+\eta_\beta^2} A_2 \tag{3.19}$$

$$B_2 = -\frac{k^2+\eta_\beta^2}{2ik\eta_\beta} A_1 \tag{3.20}$$

We impose zero-displacement at the bottom of the layer and replace B_1 and B_2 using equations 3.19 and 3.20 to express a system of equation for A_1 and A_2:

$$A_1\left[\cosh(\eta_\alpha H) - \frac{k^2+\eta_\beta^2}{2k^2}\cosh(\eta_\beta H)\right] = \left[-\sinh(\eta_\alpha H) + \frac{2\eta_\alpha\eta_\beta}{k^2+\eta_\beta^2}\sinh(\eta_\beta H)\right] A_2 \tag{3.21}$$

$$A_1\left[\sinh(\eta_\alpha H) - \frac{k^2+\eta_\beta^2}{2\eta_\alpha\eta_\beta}\sinh(\eta_\beta H)\right] = \left[-\cosh(\eta_\alpha H) + \frac{2k^2}{k^2+\eta_\beta^2}\cosh(\eta_\beta H)\right] A_2 \quad . \tag{3.22}$$

We obtain the dispersion relation by canceling the determinant of this system:

$$(4+(2-\frac{c^2}{\beta^2})^2)\cosh(\eta_\alpha H)\cosh(\omega\eta_\alpha H)-\left(4\eta_\alpha\eta_\beta+\frac{(2-c^2/\beta^2)^2}{\eta_\alpha\eta_\beta}\right)\sinh(\omega\eta_\alpha H)\sinh(\omega\eta_\beta H) \\ -4(2-c^2/\beta^2)=0 \tag{3.23}$$

We solve this equation numerically using non-linear solver and compare the analytical and numerical eigenfunctions for both differentiation methods.

We show in Fig. 3.1 the solutions for the fundamental and first four higher modes for both a second-order finite difference discretization (FD2) and the Chebyshev spectral discretization (GESC). The two methods find the correct solution for the fundamental mode; however, the spectral approach is much more accurate for a given number of points, and for the number of points ($\sim$50) used in the FD2 approach, the solution was very inaccurate for higher modes. Note the dramatic difference in convergence rate between the two methods. Even 100 points do not provide enough resolution to accurately recover the higher modes with the low-order FD approach.

Multilayer case Next we consider the multilayer case with discontinuities in elastic properties across horizontal interfaces. Analytical solutions become algebraically awkward for multiple layers, so we compare our results with eigenfunctions generated from a widely known and verified algorithm *Computer Programs in Seismology* (*Herrmann*, 1978), which we refer to as CPS. Those solutions are calculated using the Haskell–Thompson propagator matrix technique that includes a bottom boundary condition for semi-infinite half-space. To approximate this condition, we add a thick layer at the bottom of our model. We find that for fixed frequency, a layer with $\omega H/\beta > 10$ provides a satisfactory approximation (error $< 10^{-10}$) to the half-space. As a test case, we use a medium with four homogeneous layers over a thick layer that approximates an underlying half-space (Table 4.1).

As shown in Figure 3.2, for periods of 1 s and 3 s, both methods accurately retrieve the displacement eigenfunctions for the four first modes. In this case, the size of the residuals depends not only on the accuracy of our solution, but also on the accuracy of

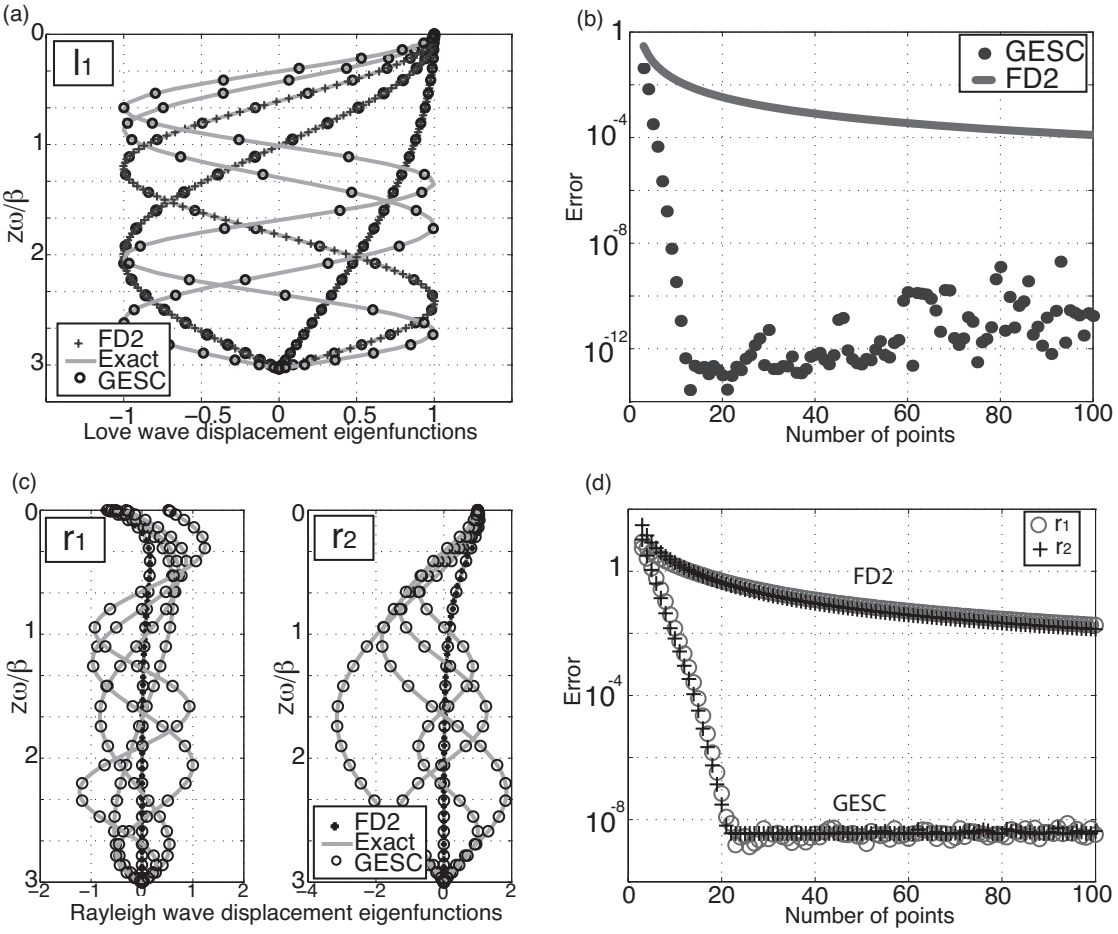

Figure 3.1: Surface-wave eigenfunctions for a single homogeneous layer with $\omega H/\beta = 3$. (a) Love-wave displacement eigenfunctions l_1 for the first five modes. (b) L_∞ error between the Love-wave numerical and exact solutions for the fundamental mode. GESC agrees to within machine precision after only 12–16 points, while FD2 converges much more slowly. (c) Rayleigh-wave horizontal (r_1) and vertical (r_2) displacement eigenfunctions for the first five modes. (d) L_∞ error between the Rayleigh-wave numerical and exact solutions for the fundamental mode.

the propagator technique, and the degree to which our lowermost layer approximates a half space. Figure 3.2 verifies that the two techniques provide the same solution for both Love and Rayleigh waves for all four modes at both periods considered.

Table 3.1: Elastic properties in the layered medium.

Layer base (km)	ρ (kg/m^3)	β (km/s)	α (km/s)
12.5	2400	3	5.19
25	2625	3.5	6.06
37.5	2850	4	6.93
50	3075	4.5	7.79
1000	3300	5	8.66

Stability, accuracy, and efficiency In the original propagator matrix methods, numerical instabilities arose at high frequencies due to inexact cancellation of extremely large terms (the exponentially growing solutions of the elastic wave equation) of opposite sign. The collocation method completely avoids this because exponentially growing functions are never evaluated, and the method is therefore free of instability even at high frequencies. Of course, obtaining an accurate solution requires using enough points to resolve the spatial variation of the eigenfunctions, and this increases the size of the matrix system. Consequently, it is unavoidable that the computational expense increases if one seeks to accurately solve for the high order modes at high frequencies.

Using a spectral method, as opposed to a low order finite difference or finite element method, minimizes the number of points required for accuracy, as demonstrated by the examples above. Adaptive sampling further increases the efficiency to add resolution only where eigenfunction variations are likely to be the strongest (e.g., near the free surface or material interfaces).

We illustrate this by solving for the fundamental mode at high frequencies (1– 50 Hz) using two sampling strategies. To quantify efficiency, we determine the minimum number of grid points required to reach a given accuracy measured in terms of the L_2-norm of the difference between our solution and a high resolution reference solution. We refine the mesh until error drops below a given tolerance (i.e., 10^{-3} or 10^{-6}). We focus on the specific material structure shown in Figure 3.3(a), which consists of three layers. The uppermost layer, of thickness H, has an average shear wave speed β_0.

One sampling strategy (not adaptive) specific to the surface-wave fundamental

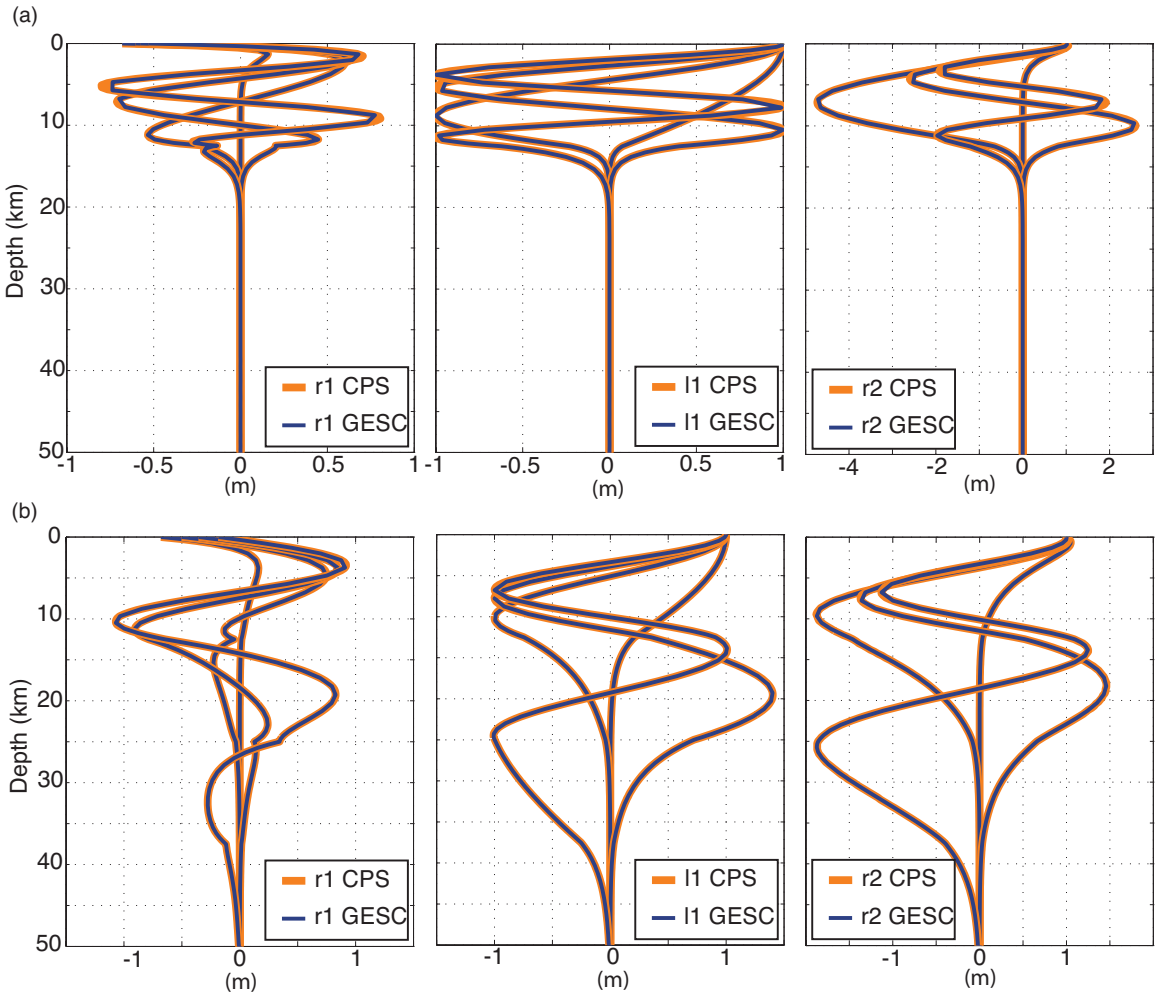

Figure 3.2: Comparison of the CPS and GESC solutions for the fundamental and first three higher mode surface-wave displacement eigenfunctions (l_1, r_1, and r_2) for (a) $T = 1$ s and (b) $T = 3$ s in a layered medium (see Table 4.1).

modes is to increase the number of points, or resolution, in the first layer until meeting the accuracy criterion. The second strategy (adaptive) is to divide the first layer into two layers, with the shallowest having a frequency-dependent thickness $H_1 = \beta_0 T/2$, and the second layer having thickness $H_2 = H - \beta_0 T/2$, where T is the period. We then only refine within the upper layer for the fundamental mode. This allows us to preserve high resolution near the surface where the spatial variations of the fundamental mode eigenfunctions are strongest, while avoiding unnecessary

refinement at greater depths where the eigenfunctions either vary slowly or have negligible amplitude. The choice $\beta_0 T/2$ may not be optimal, but suffices for this comparison.

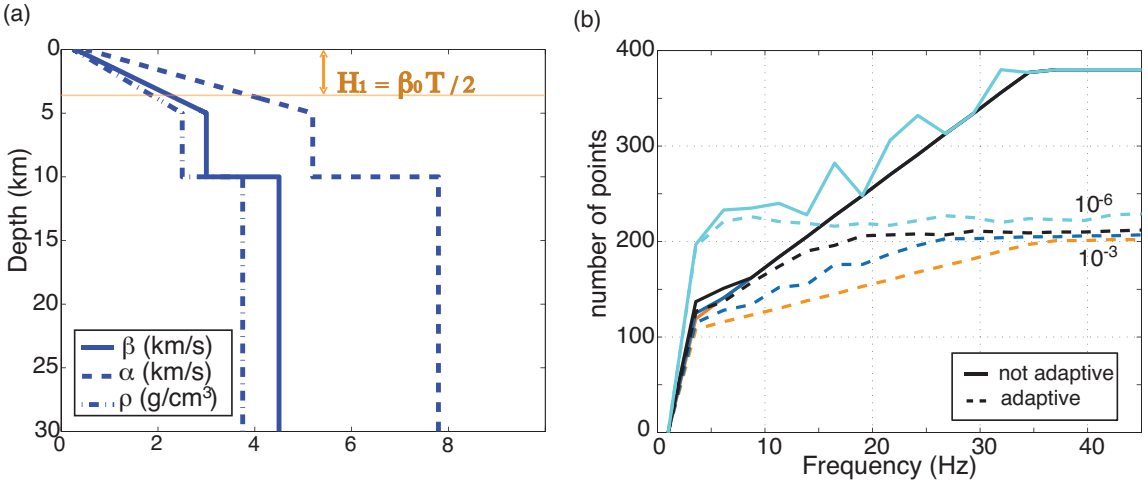

Figure 3.3: (a) Velocity profile used where λ is the frequency-dependent thickness for the adaptive sampling. (b)Number of points required to meet accuracy of the solutions with increasing frequency. Solid lines show the original sampling, dashed lines show the convergence of the adaptive sampling

In Figure 3.3(b), we display the number of points required to reach a desired accuracy with increasing frequency. In the first case (not adaptive), the required number of points monotonically increases with frequency and the method becomes computationally inefficient. In the second case (adaptive), the required number of points levels off and it is possible to achieve a desired accuracy at arbitrarily high frequencies without increasing the overall number of points. This simple test reveals the advantage of using an adaptive sampling strategy to minimize computational expense. One can envision a procedure that automatically adjusts the number of points in each layer, or even the number of layers, to maximize efficiency, but we have not pursued this.

We have now verified our technique for single and multilayer cases, primarily for cases with constant properties in each layer. The power of the collocation approach becomes more evident when there are gradients in the elastic properties. In this

case, the propagator matrix technique loses accuracy since it replaces a medium with continuously varying properties with a stack of homogeneous layers. In the following sections we solve the eigenproblem for complex velocity structures, including an example featuring thick sedimentary layers in a deep sedimentary basin. We illustrate the technique by extracting dispersion curves for a 1-D profile from the Los Angeles basin, which is an exceptionally deep (9 km) basin that is likely to have very complex surface-wave modes. We take our velocity profiles from the SCEC CVM-4 velocity model (*Magistrale et al.*, 2000; *Kohler et al.*, 2003).

Dispersion Curves

Surface-wave tomography depends on dispersion, as expressed by variations in phase velocity c and group velocity U with frequency. These can be related using the energy integrals:

$$c_R = \frac{\omega}{k_R}, \qquad c_L = \frac{\omega}{k_L} \qquad U_R = \frac{I_2^R + I_3^R/(2k_R)}{c_R I_1^R}, \qquad U_L = \frac{I_2}{c_L I_1}, \tag{3.24}$$

where for Love waves

$$I_1^L = \frac{1}{2}\int_0^\infty \rho l_1^2 dz, \qquad I_2^L = \frac{1}{2}\int_0^\infty \mu l_1^2 dz, \tag{3.25}$$

and for Rayleigh waves

$$I_1^R = \frac{1}{2}\int_0^\infty \rho(r_1^2 + r_2^2)dz, \quad I_2^R = \frac{1}{2}\int_0^\infty \left[(\lambda+2\mu)r_1^2 + \mu r_2^2\right] dz,$$
$$I_3^R = \frac{1}{2}\int_0^\infty \left[\lambda r_1 \frac{dr_2}{dz} - \mu r_2 \frac{dr_1}{dz}\right] dz. \tag{3.26}$$

The eigenfunctions are known at the Chebyshev collocation points, providing a unique polynomial representation of the solution. We use Clenshaw–Curtis quadrature to evaluate the energy integrals by simply calculating the dot product of the energy integrands at the collocation points and the quadrature weights (*Trefethen*, 2000, ch. 12).

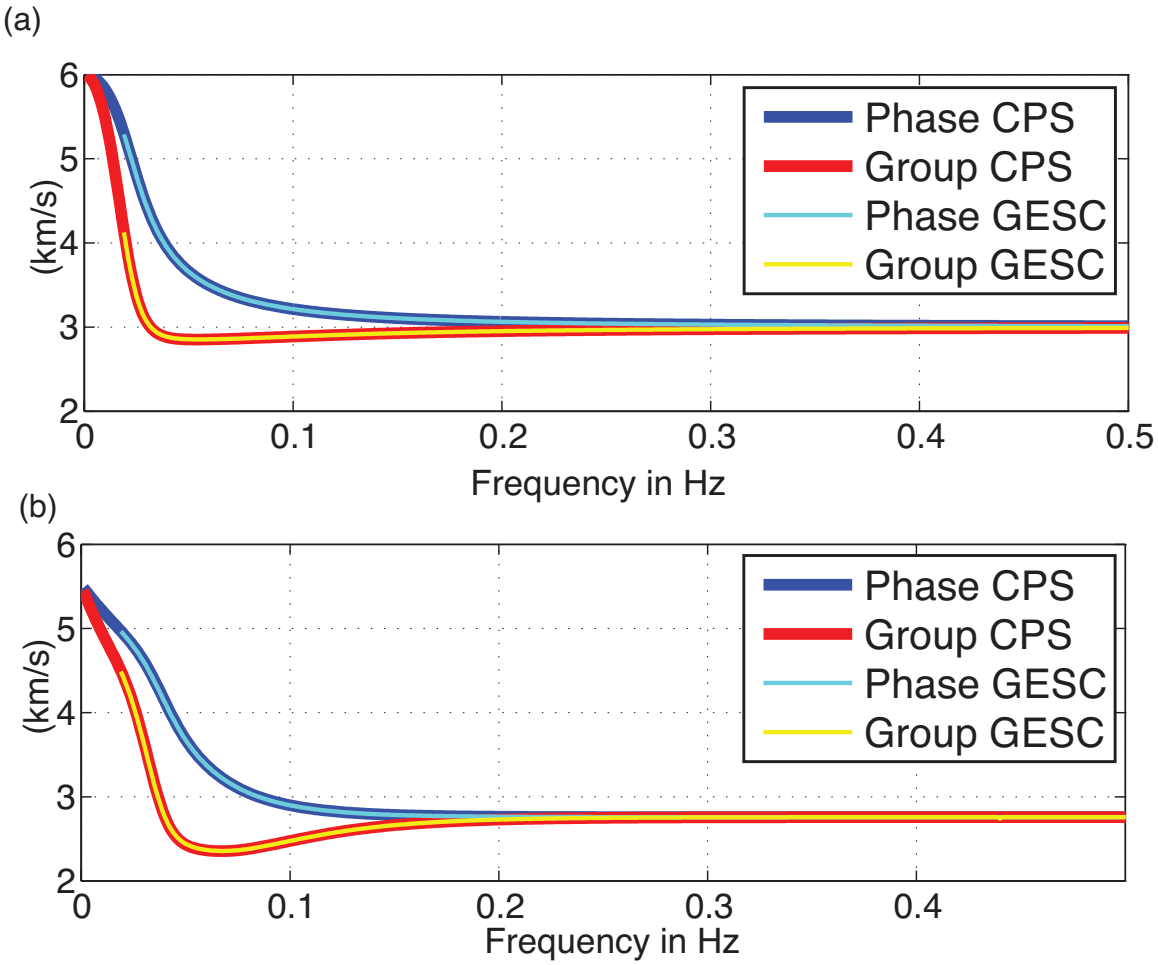

Figure 3.4: Comparison between dispersion curves for CPS and GESC solutions for fundamental mode Love (a) and Rayleigh waves (b). Because of the finiteness of our bottom layer, we do not compare the very low frequency solutions.

In Figure 3.4, we verify the accuracy of the dispersion curves by comparing our results with the dispersion curves calculated with CPS. This demonstrates the accuracy and efficiency of the Chebyshev spectral collocation method for surface-wave eigenfunctions, wavenumbers, and dispersion curves. Thus, we have at hand all the tools necessary to generate synthetic surface-wave waveforms.

Time domain waveforms

We seek to generate theoretical waveforms for surface waves in the far-field limit. We follow *Aki and Richards* (2002, ch. 7, Eqs. 7.148, 7.150, and 7.151) and express the displacement fields for surface waves generated by a point moment tensor source at depth h recorded at distance r and azimuth ϕ in terms of the eigenfunctions.

We build a layered model (see Table 4.1) with constant properties in each layer for this test case. We use a parabolic moment-rate function (*Herrmann*, 1978) with the Fourier spectrum

$$\dot{M}_o(\omega) \propto \exp(-i\omega 2\tau)\frac{4\sin^2(\omega\tau/2)\sin(\omega\tau)}{(\omega\tau)^3} \tag{3.27}$$

where τ is the width of the parabola in time. We compute the spectrum of the surface-wave displacements at each frequency, given a frequency sampling that depends on the time sampling and length of the time series of interest. In the following example, we generate a time series of 1000 s and 4096 points using the Fast Fourier Transform, which leads to $\Delta t = 0.24$ s.

In Figure 3.5, we compare results from the two methods for a double couple source for a moderate earthquake in southern California (based on the 12/08/08 M 5.4 Chino Hills event, with strike 291°, rake 142°, dip 58°, and scalar moment $M_0 = 1.53 \times 10^{17}$ N m). The moment tensor is provided by the Southern California Earthquake Data Center and involves both strike-slip and thrust components. We impose the source at 5 km depth and compute the displacement fields for a surface receiver at a distance of 300 km and an azimuth of 50°.

The waveforms clearly overlap, which verifies our method for the far-field case. As mentioned earlier, the power of the spectral approach is that it allows a general variation of properties with depth.

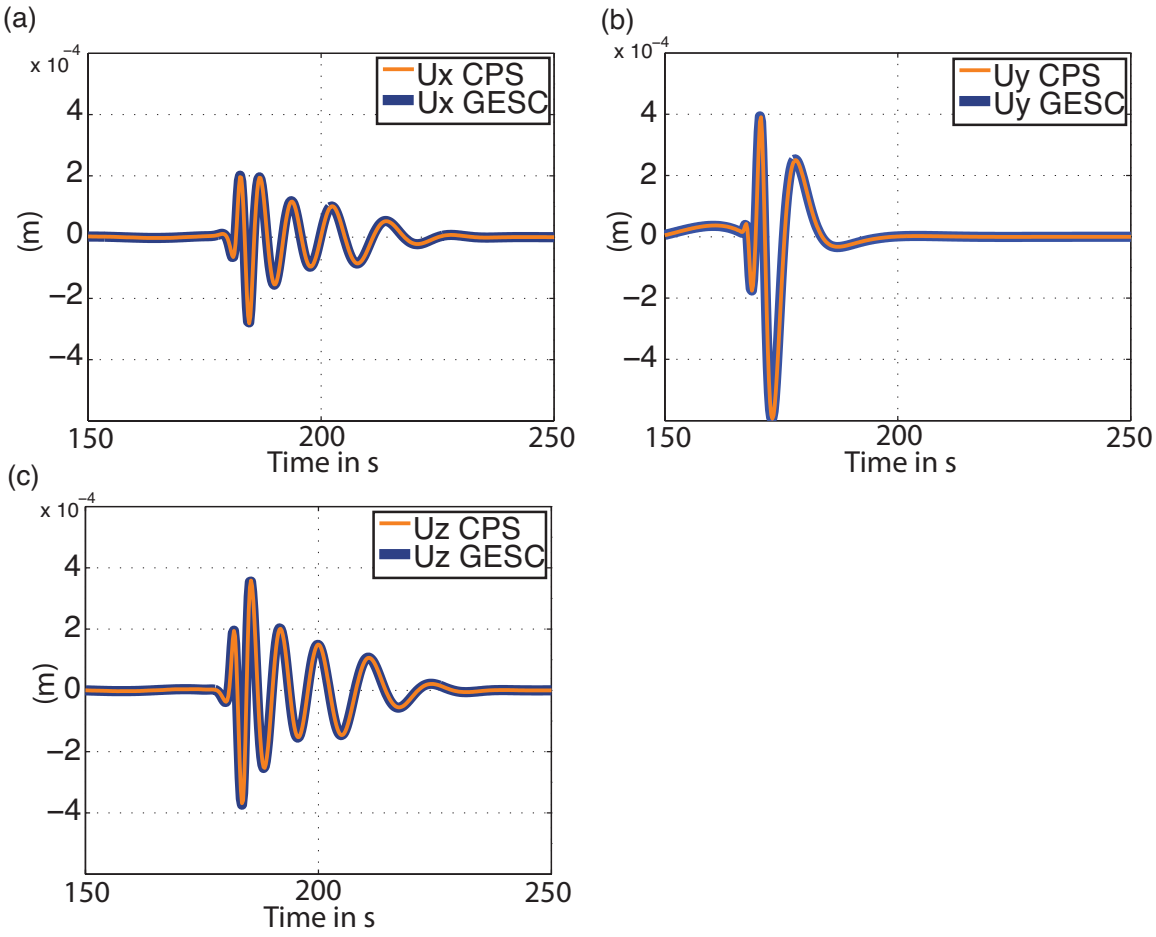

Figure 3.5: Comparison between our results (GESC) and the waveforms obtained using the CPS technique.

Surface-prograde particle motion

The first case we consider is the change in retrograde to prograde particle motion of the Rayleigh fundamental mode that can occur when sediments overlie hard bedrock. *Tanimoto and Rivera* (2005) suggest that the presence of very low shear wave speed at the surface could change the Rayleigh wave particle motion from retrograde to prograde and, for the special case of the Los Angeles sedimentary basin, this reversal lies in the frequency band of 0.06 to 0.17 Hz depending on the thickness of the sedimentary layer. We investigate these findings, first with an idealized velocity

model used by *Tanimoto and Rivera* (2005).

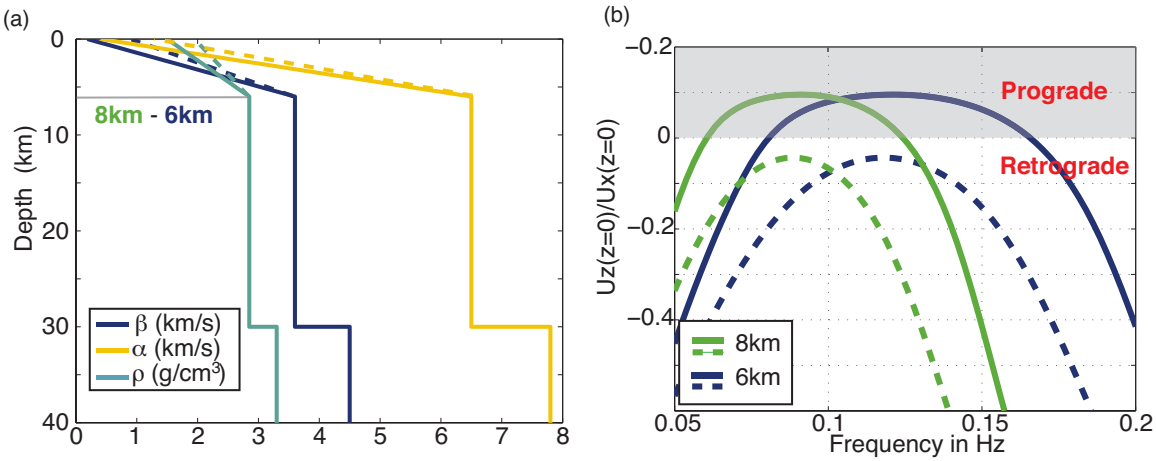

Figure 3.6: (a) Idealized velocity structure with thick sediment layers (6 and 8 km). (b) Changes from retrograde to prograde motion for Rayleigh waves as indicated by the ratio $u_z(0)/u_x(0)$. For a given sediment thickness, we see a change in retrograde to prograde motion from 0.07 to 0.18 Hz (for 6 km-thick sediments) and from 0.06 Hz to 0.12 Hz (for 8 km-thick sediments), highlighted in gray, given the surface shear velocities $\beta_0 = 0.1605$ km/s and $2\beta_0$.

We obtain the same transitions between retrograde and prograde motion for those cases, as highlighted by the gray box in Fig. 3.6. The lower the surface shear velocity is, given for a sediment thickness, the more likely prograde particle motion becomes.

We next consider 1-D velocity profiles extracted from the Community Velocity Model Version 4.0 from the Southern California Earthquake Center, under several seismic stations located above the thickest parts of the Los Angeles sedimentary basin. In Fig. 3.7 we display the ratio of the horizontal and vertical eigenfunctions at the Earth's surface.

While we do not see any changes in the sense of particle motion at locations near the deepest part of the sedimentary basin (WTT, USC, LGB and LLS), there are interesting changes in behavior with the surface shear velocity showing $u_x(0)$ almost four times as large as $u_z(0)$. *Tanimoto and Rivera* (2005) argue that this corresponds

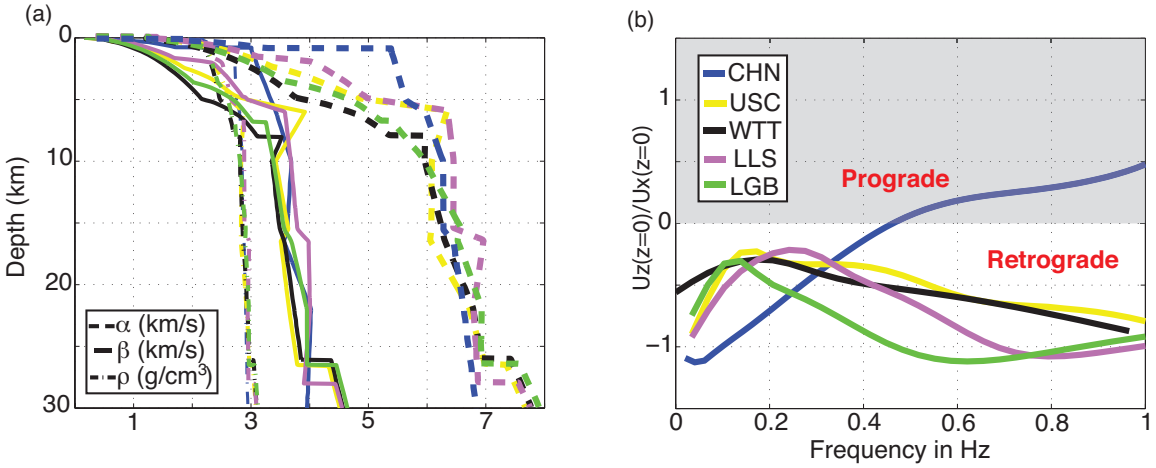

Figure 3.7: (a) Velocity structure in Los Angeles area interpolated from CVM4. (b) $u_z(0)/u_x(0)$ as a function of frequency. We do not see changes in Rayleigh-wave polarization for the expected locations on the deepest part of the sedimentary basin, but we do see the retrograde-to-prograde transition occurring at higher frequency for CHN.

to the resonant period of the sedimentary layer for vertically traveling shear waves. It is interesting to note that in this case, the 5 – 8 s periods we find are similar to the resonant frequency of the geometry of the basin and the 1-D structure. Surprisingly, the change from retrograde to prograde particle motion occurs at a shallower part of the sedimentary basin, at CHN. At this location, the sediments are thinner and the gradient in the elastic parameters is much stronger, which results in the change in particle motion.

We further explore the occurrence of prograde Rayleigh-wave particle motion from variations in the velocity models in simple cases. We test for the cases of layer of thickness H = 1 km for constant layer properties and constant gradient over half space. We vary the value of a Poisson medium β_1, α_1, ρ_1 at the surface and keep the half-space elastic properties β_2, α_2, ρ_2 constant (Fig. 3.8). We establish a characteristic frequency $f_c = (\beta_2 - \beta_1)/H$ that reflects the contrast of impedance. In Figure 3.8 (b), we show the ratio of the vertical-to-vertical eigenfunction values taken at the surface that reflects the ellipticity of the particle motion. In the case of a half space, this ratio is approximately -1.5. We map the range of frequency where we expect

prograde particle motion at a given contrast in shear velocity as highlighted in red above the contour line. Prograde particle motion only occurs in a very narrow range of frequency and elastic parameters for Poisson medium. We note however that the ratio varies considerably in media with high contrast. The ratio varies from the half space value to positive values smoothly in the case of a gradient over half space, whereas the transition is much sharper in the constant layer over half space cases.

Hypocenter depth effect on ground motion

We calculate the surface-wave eigenfunctions for a 1-D model extracted from CVM4 and located at the epicenter of the M 5.4, 2008 Chino Hills earthquake. The model has a combination of layers, gradients, and large discontinuities, which are straightforward to incorporate in our approach. The hypocenter is estimated to be around 12.4 km. Although we cannot reproduce 3-D effects from the sedimentary basin in our simulations, we can demonstrate the effect of depth on surface wave excitation for this source. This is important because the Puente Hills Thrust, which underlies the basin, has the potential for large earthquakes that could strongly excite basin resonances. We explore what would be the impact of a deep over shallow source on the theoretical displacement spectra at a distant station (SDD) in Orange County, for sources in the sediments at depths of 4 and 8 km, and at 13 km depth in the underlying bedrock, near the site of the Chino Hills earthquake. In the time series, we impose a moment-rate function with a width $\tau = 0.5$ s as in equation (3.27).

As expected in Fig. 3.9, the depth of the source in this particular velocity profile strongly influences the wave excitation spectrum. For the shallow source (4 km), high frequency surface waves are much more strongly excited. The velocity structure and the depth of the source have a strong effect on the resulting ground motion predicted in terms of duration and spectrum of the shaking.

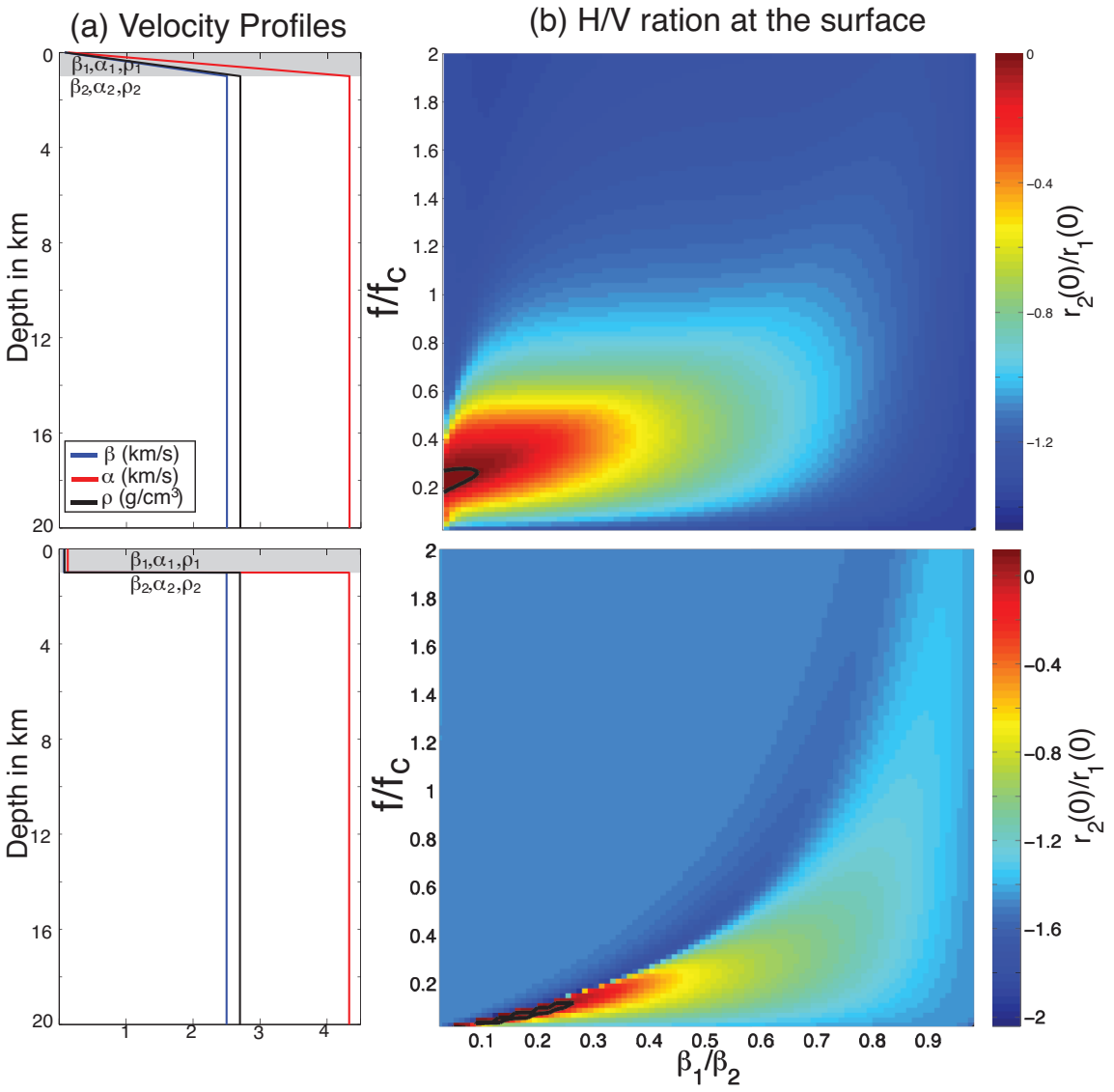

Figure 3.8: (a) Velocity profiles tested: constant properties layer on the top and constant gradient at the bottom. (b) ratio of the Rayleigh-wave eigenfunctions taken at the surface $r_2(0)/r_1(0)$ for varying upper layer velocities and normalized frequency.

Conclusions

We have developed a formulation of the surface-wave eigenproblem in standard linear form, and converted it to a generalized matrix eigenvalue problem using a Chebyshev spectral collocation method. The spectral collocation approach allows us to solve

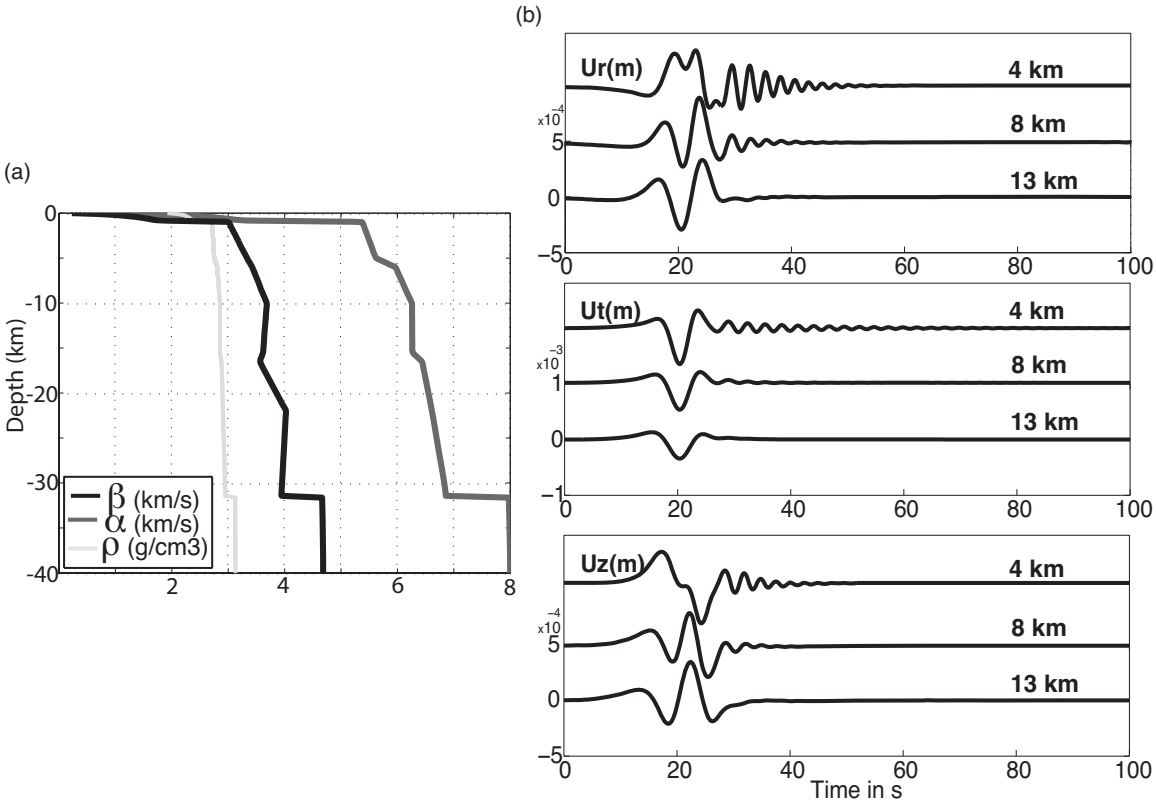

Figure 3.9: (a) Velocity structure under CHN seismic station (SCEC CVM4). (b) Displacement time series expected at SDD.

the eigenproblem with high accuracy with a minimal number of points per layer (generally about 20 – 30 for fundamental mode calculations). The accuracy of spectral methods makes this technique highly efficient. We verified the method by testing our results against analytical solutions for simple velocity structures and against solutions calculated with traditional methods (*Herrmann*, 1978) for more complex structures.

We have not considered anelasticity in this study. In similar formulations, anelastic effects of a linear viscoelastic solid can be incorporated by allowing the elastic moduli to assume complex, frequency-dependent values. Although we have not implemented it, this approach should be straightforward to handle in our method, since the eigenvalue solver can be equally well applied to complex matrix systems having complex eigenvalues.

The power of using spectral collocation methods for this eigenproblem is that they permit general variations of properties with depth and solve the eigenproblem in an accurate and efficient manner. This allows for the sort of complexities in shallow crustal structure (sediment consolidation with depth, sharp interfaces, low velocity zones) that we expect to encounter in practical situations. The frequency range that can be solved is broad and our technique is free of numerical difficulties at high frequencies, provided we optimize the number of points in each layer to ensure adequate resolution and minimize the total number of points used.

We demonstrate the utility of our method by calculating dispersion curves and theoretical surface-wave seismograms in the far-field approximation. We apply the method to particular locations from the Los Angeles sedimentary basin. We have explored the domain of occurrence of prograde particle motion at the surface for simple cases and found only a narrow range that satisfy the conditions. We however highlighted the impact of sharp contrast in velocity structure on the Rayleigh-wave ellipticity at the surface. We do not find the retrograde to prograde particle motion switch at the specific locations of the SCEC CVM4 mentioned by *Tanimoto and Rivera* (2005); however, we do see it at locations where the sedimentary basin is shallow and where the gradient with depth of the elastic parameters is very strong. We highlight, however, the importance of structure on the Rayleigh-wave elliptical

particle motion and further work is needed to undertake the inverse problem. Preliminary work from *Lin et al.* (2012) uses both the H/V ratio and the phase velocity measurement to constraint α, β and ρ.

This eigenproblem may be generalized to examine any interface-wave behavior. We have so far worked with air-solid and solid-solid interfaces by constraining specific boundary conditions. We can extend the problem of fluid-solid interface waves for non-viscous fluids, such as Scholte waves in the ocean, by changing the boundary and continuity conditions.

Chapter 4

The Virtual Earthquake Approach

Introduction

Ground motion prediction is a central component of seismic hazard analysis. Until recently, it has been based primarily on ground motion prediction equations, which are regressions of observed ground motion intensity measurements (*Abrahamson and Shedlock*, 1997; *Toro et al.*, 1997) against source, path, and site descriptions. Those empirical equations suffer from a shortage of data for large seismic events at short distances, and only account for wave propagation effects, such as amplification in sedimentary basins, approximately, if at all.

Simulations of earthquake rupture and the resulting ground motion have the potential to overcome the lack of data and to properly model wave propagation in basins, so seismologists are increasingly turning to such physics-based methods (*Olsen et al.*, 2006, 2009) for ground motion prediction. If such simulations are to be trusted, however, their accuracy must be established (*Hartzell et al.*, 2011).

Within the three main sources of uncertainty in ground motion prediction, the earthquake rupture process, wave propagation in a complex three dimensional Earth, and nonlinear site effects, we focus on the linear wave propagation, or path effects, and only consider moderate sized earthquakes, for which a simple source description suffices. *Prieto and Beroza* (2008) use deconvolution of the ambient seismic field without pre-processing and show that the relative amplitude of the Ambient Noise Impulse Response Function (ANIRF) is preserved and exhibits similar propagation effects to those observed in records of a moderate earthquake.

Figure 4.1 shows schematically the steps we undertake to obtain a realistic displacement response to a buried double couple source. The ANIRF is the surface-wave response of the Earth to a virtual source (a point force) at the surface (station-source) and recorded at the surface (station-receiver). Because the point force and recorded displacement are both three-component vectors, the ANIRF is a rank two tensor with nine components. We compute the nine components of the ANIR tensor following *Prieto and Beroza* (2008) (Fig. 4.1(a)) and show in the first section that we retrieve reliable propagation information with the ambient noise surface-impulse response. The source depth strongly affects the fundamental mode excitation at short periods,

especially for complex velocity structures, such as in southern California, and we must account for that. However, the impulse responses obtained from the ambient noise, which account for the complex 3-D wave propagation, restricts the surface-wave excitation to be at the surface. If we describe the medium surrounding the source to be locally 1-D, we can express the excitation as solution of the surface-wave eigenproblem. In the second section (Fig. 4.1 (b)), we use the Generalized Eigenproblem Spectral Collocation (GESC) method (*Denolle et al.*, 2012) to solve the surface-wave eigenproblem by assuming locally a 1-D medium at the virtual source. We use the displacement eigenfunctions to correct the ANIRF and simulate the response of the Earth to a buried point force. In the following section (Fig. 4.1(c)), we account for radiation pattern effects due to a double-couple at depth. We compare the predicted surface-wave ground motion from the depth-and source-corrected ANIRFs, referred to as "virtual earthquakes," with records from moderate earthquakes, which we treat as point sources at the wavelengths/periods of interest. We choose four events that occurred close to permanent broadband seismic stations in southern California to validate the approach: the 2009 M 4.5 San Bernardino, 2008 M 5.1 Hector Road, 2008 M 5.4 Chino Hills, and 2011 M 4.2 San Fernando earthquakes. By validating the virtual earthquakes against data, we demonstrate that it should be possible to simulate long-period ground motion from larger earthquakes with this approximation.

We have discussed in the previous chapters the validity and uncertainties in the ambient seismic field Green's functions on how we preserve the relative amplitudes with minimal data processing of the ambient seismic field. Although the noise sources consistently originate from the Pacific coast (*Stehly et al.*, 2006) in the period band of 5 – 10s. We show in figures 4.1– 4.8, the maximum amplitude of the impulse responses, averaged from causal and anticausal sides. We do not observe any systematic azimuthal (i.e., from each station source to each receiver) variation in the amplitudes, which suggests that our process successfully recovers energy that is much closer to the idealized equipartitionned case than the directional source distribution would indicate.

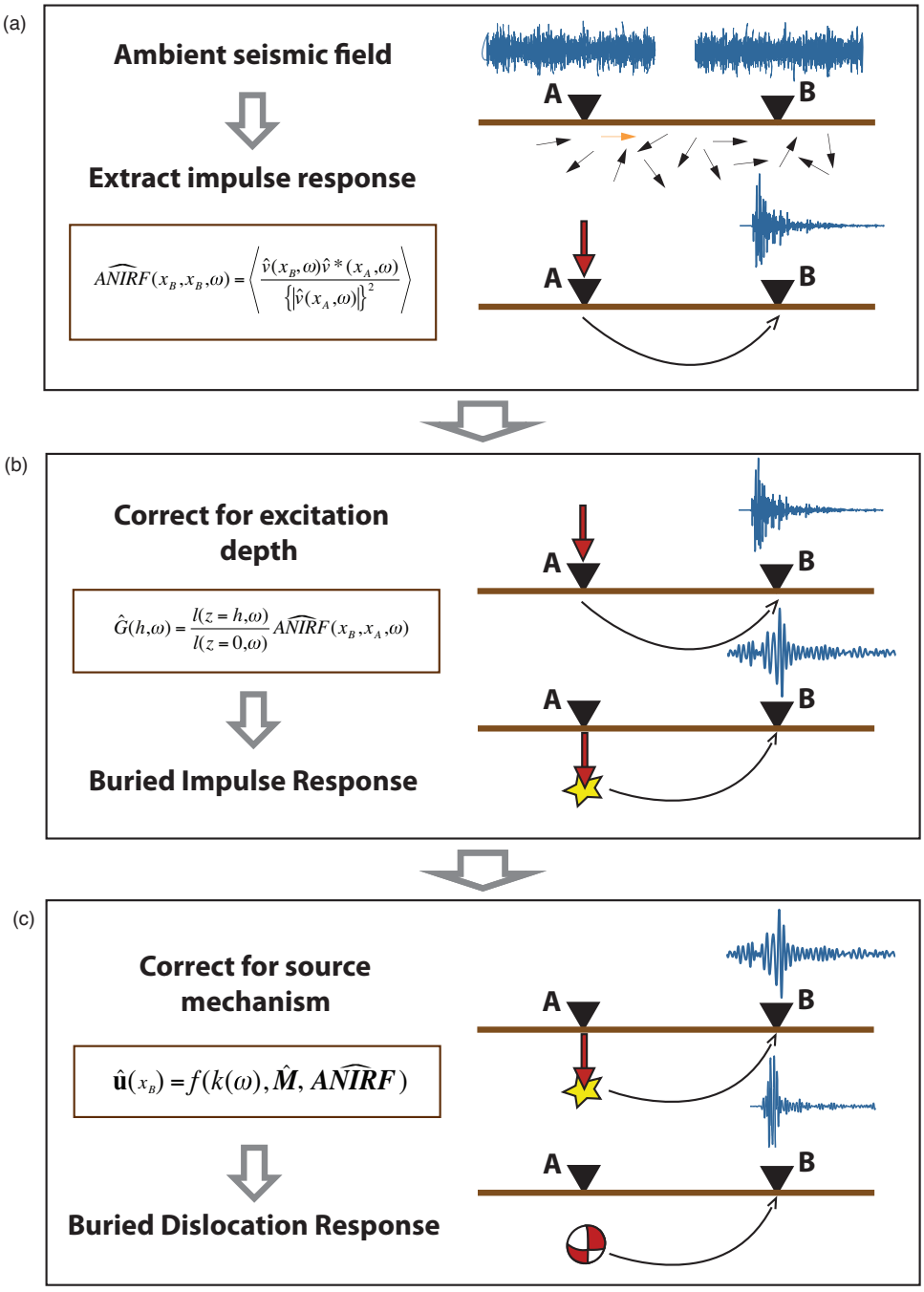

Figure 4.1: Scheme to predict surface-wave response to buried point dislocations using the ambient seismic field. (a) We compute the impulse responses $\widehat{ANIRF}(\mathbf{x}_B, \mathbf{x}_A, \omega)$ from the ambient noise displacement records at the virtual source A, $\hat{\mathbf{v}}(\mathbf{x}_A, \omega)$, and receiver B, $\hat{\mathbf{v}}(\mathbf{x}_B, \omega)$. (b) We solve the surface-wave eigenproblem and use the displacement eigenfunctions $l(z)$ to predict the response to a buried point force (symbolized by red arrows) $\widehat{\mathbf{G}}(h)$. (c) We use those eigenfunctions and moment tensor ($\hat{\mathbf{M}}$) to predict ground motion in B, $\hat{\mathbf{u}}(\mathbf{x}_B)$.

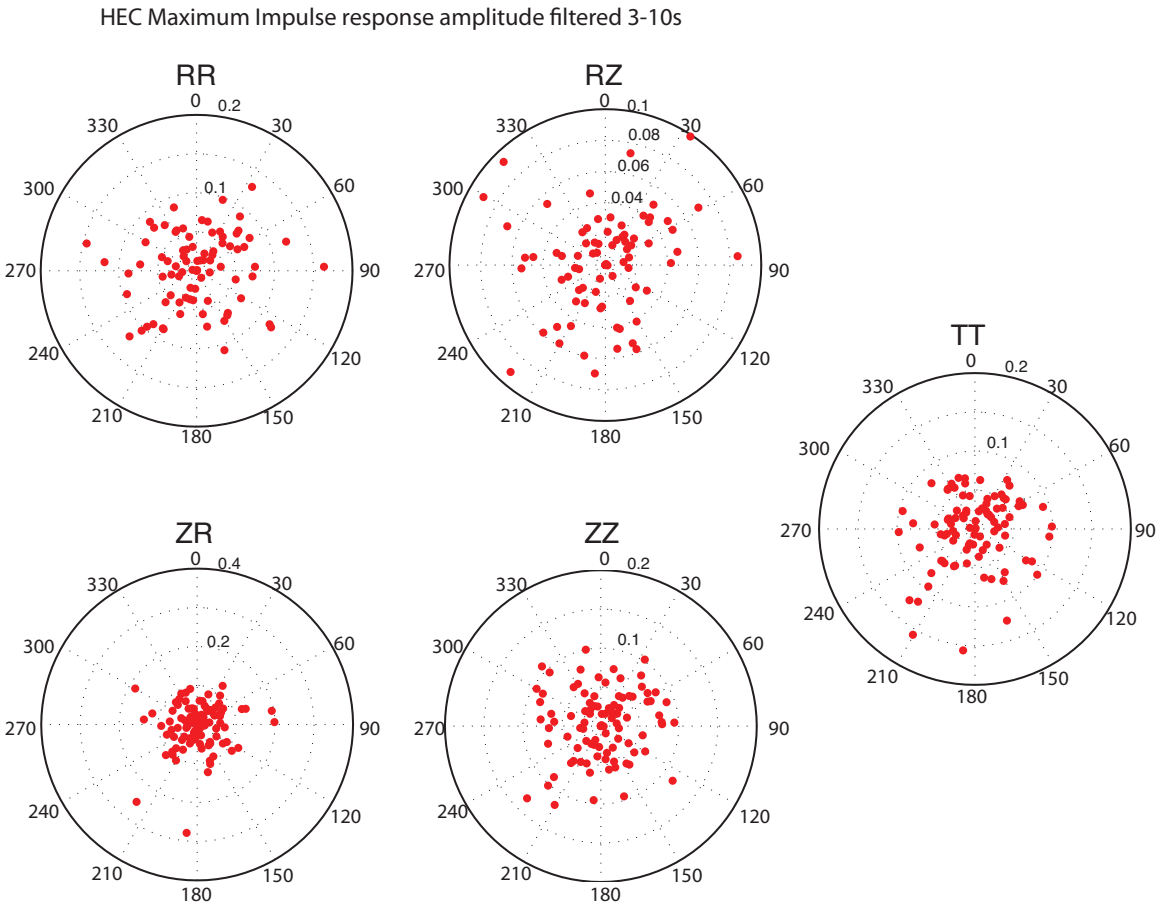

Figure 4.2: Variation with azimuth (or station pair) of the maximum amplitude of the impulse response, filtered 3 – 10 s, corrected for geometrical spreading $\sqrt{r}$, where r is the distance between source and receiver for the virtual source HEC.

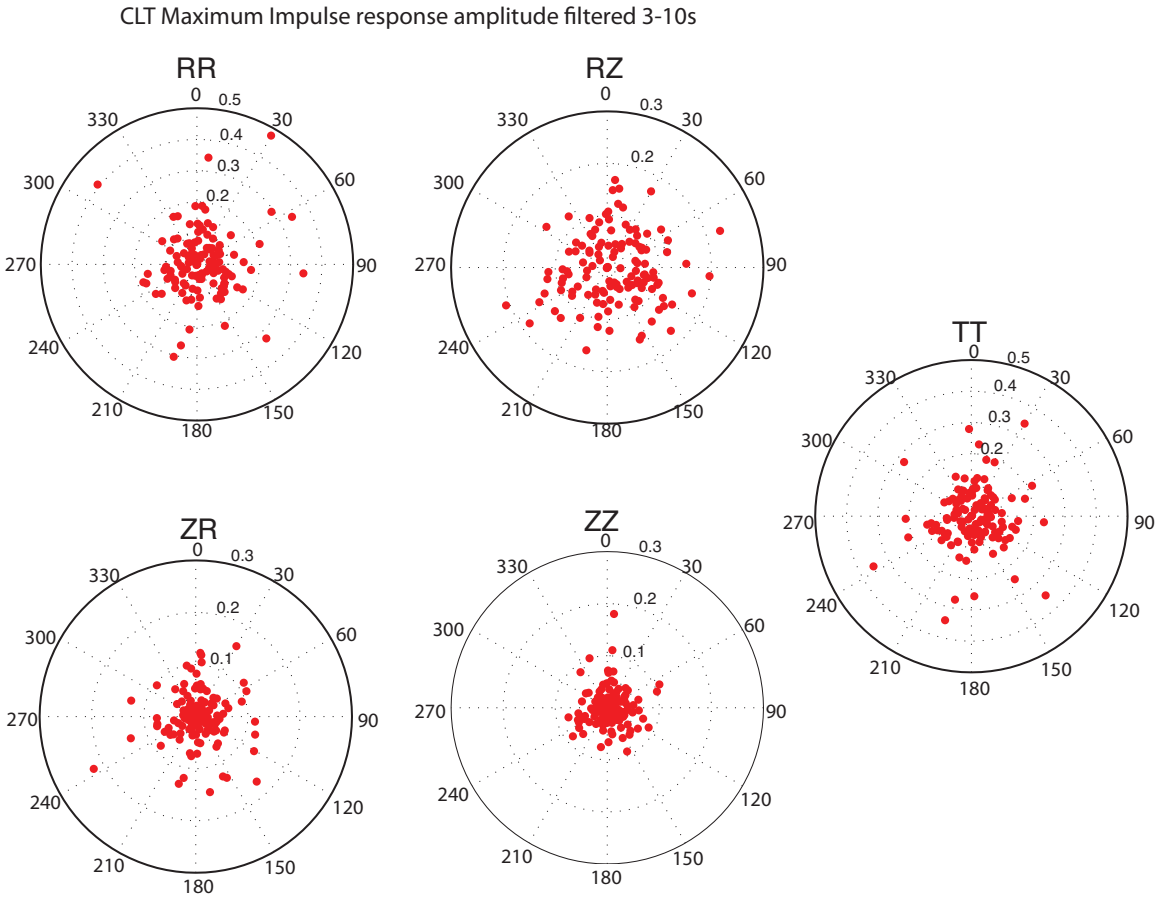

Figure 4.3: Variation with azimuth (or station pair) of the maximum amplitude of the impulse response, filtered 3 – 10 s, corrected for geometrical spreading $\sqrt{r}$, where r is the distance between source and receiver for the virtual source CLT.

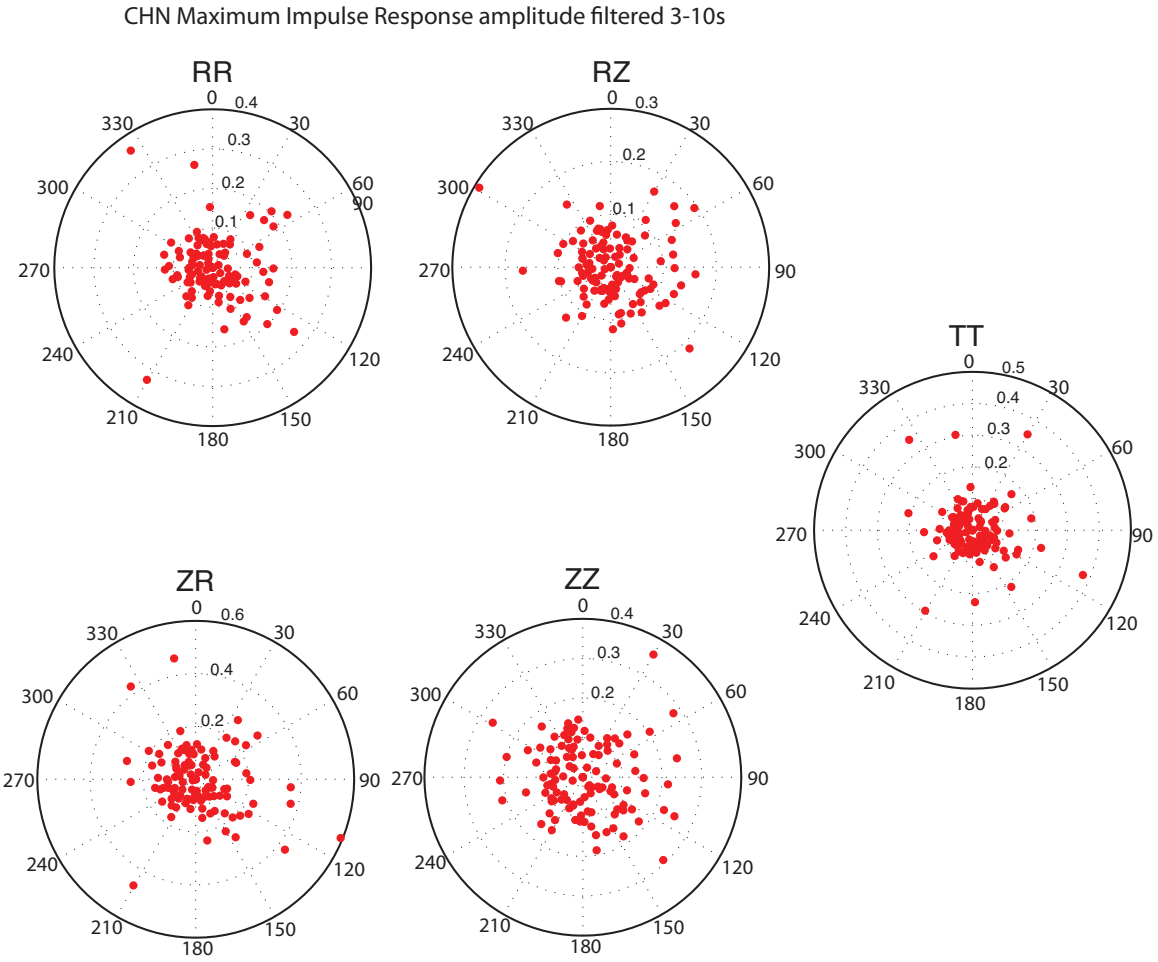

Figure 4.4: Variation with azimuth (or station pair) of the maximum amplitude of the impulse response, filtered 3 – 10 s, corrected for geometrical spreading $\sqrt{r}$, where r is the distance between source and receiver for the virtual source CHN.

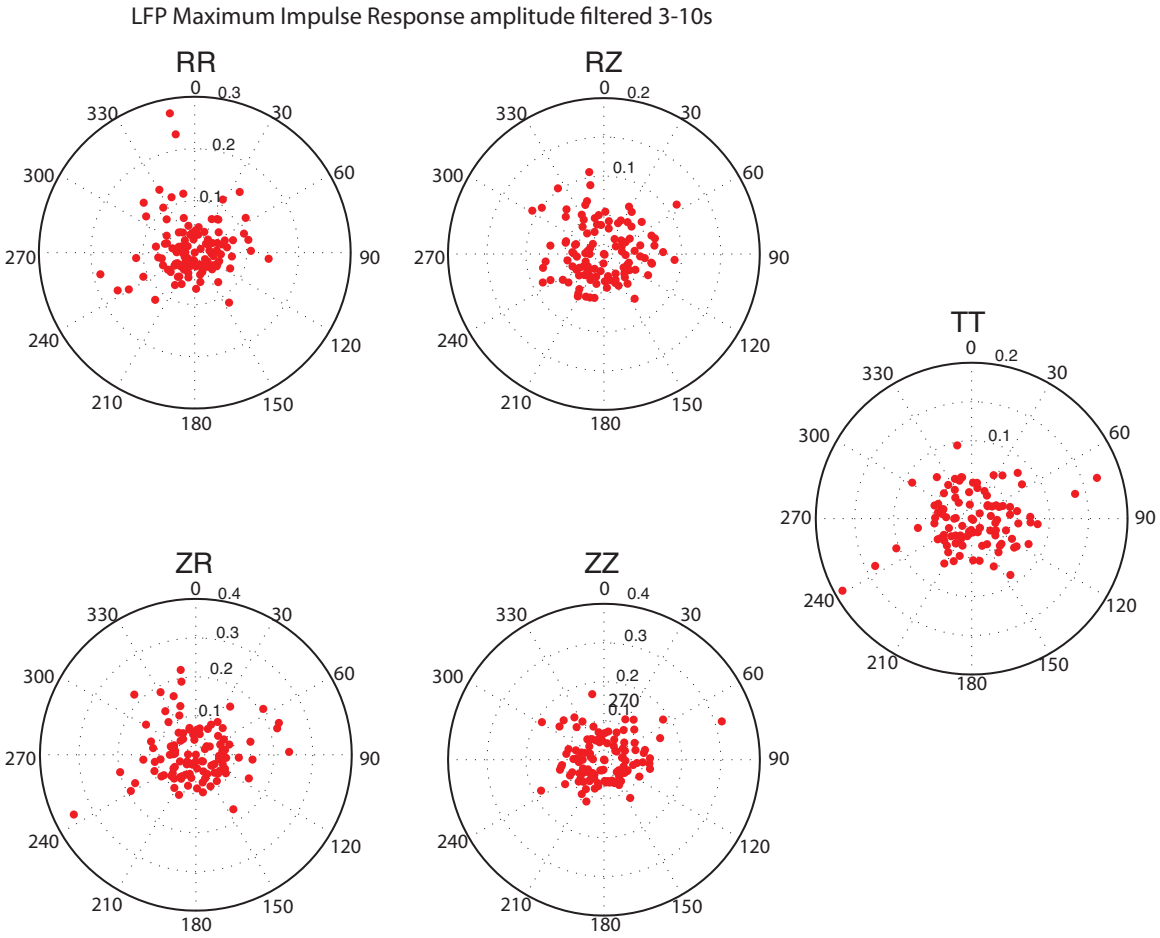

Figure 4.5: Variation with azimuth (or station pair) of the maximum amplitude of the impulse response, filtered 3 – 10 s, corrected for geometrical spreading $\sqrt{r}$, where r is the distance between source and receiver for the virtual source LFP.

Impulse response functions

We use the raw ambient seismic field to compute the IRFs for one year of continuous data (during 2010 – 2011) from the Southern California Seismic Network and ANZA seismic network. We select one-hour-long time series, and discard the ones with spikes larger than 10 times the standard deviation of the window, and compute the frequency domain IRF (*Prieto et al.*, 2009).

Stehly et al. (2006) shows that the noise sources in southern California varies through the year cycle, but mainly originate from the oceans. We use *Seats et al.* (2011)'s technique to improve the apparent azimuthal distribution of the noise sources, which accelerates convergence to the Green's function. We divide the day-long records into 70 time windows of 30min duration, overlapped by 20 minutes.

In the context of predicting ground motion, we define the ANIR tensor to be proportional to the surface-wave Green tensor $\mathbf{G}(\mathbf{x}, \mathbf{x}', t)$, up to a normalization factor that is common to all receivers. The Green tensor component $G_{ij}(\mathbf{x}, \mathbf{x}', t)$ is the i^{th} component of displacement at receiver position $\mathbf{x}$ and time t by a unit impulse in the j^{th} direction applied at source position $\mathbf{x}'$ and time $t = 0$. The Fourier transform of $\mathbf{G}(\mathbf{x}, \mathbf{x}', t)$ is $\hat{\mathbf{G}}(\mathbf{x}, \mathbf{x}', \omega)$; a similar notation applies to other fields in the following derivations. For each station pair (A,B), we compute the ANIR tensor component averaged over many time windows:

$$\widehat{ANIR}_{ij}(\mathbf{x}_B, \mathbf{x}_A, \omega) = \left\langle \frac{\hat{v}_i(\mathbf{x}_B, \omega)\hat{v}_j^*(\mathbf{x}_A, \omega)}{\{|\hat{v}_j(\mathbf{x}_A, \omega)|\}^2} \right\rangle, \tag{4.1}$$

where A is the virtual source (seismic station) and B is the receiver (seismic station), $\hat{v}_i(\mathbf{x}_A, \omega)$ and $\hat{v}_j(\mathbf{x}_B, \omega)$ are their respective noise displacement spectra. The operator $\langle \quad \rangle$ denotes stacking over time-windows and $\{ \quad \}$ denotes smoothing over the virtual source spectrum (10-point running average) to ensure stability in the deconvolution.

Along with the smoothing operation, we apply a water level if necessary to avoid singularities in the deconvolution.

To extract both Rayleigh and Love waves, we rotate the tensor from the coordinate system North-East-Down (NED) to Radial-Transverse-Down (RTD). The vertical component D is positive downward and the horizontal rotation is shown for the radial and transverse components, respectively R and T in Figure 4.6.

We compute the nine components of the Green's tensor, given the three channels at each station. We make the assumption that the Rayleigh waves are fully described in the radial and vertical planes (on the tensor components RR, RD, DR, DD) and that the Love waves are on the transverse components only (TT). This is an approximation since we ignore off-great-circle propagation, and any Love-to-Rayleigh wave conversion (and vice versa), surface wave-to-body wave conversion from complex 3-D structure (*Gregersen*, 1978; *Yoshida*, 2003; *Langston et al.*, 2009), or anisotropy (*Yao et al.*, 2011). These effects may be present in the Green's function, but we do not correct for them in the excitation nor in the recording at the specific locations. In southern California, we see some leakage of energy on the cross-terms DT, TD, RT and TR in the period band 4–10 s. Although this is not the focus of our study, it is a useful observation that could be used to constrain crustal structure.

Once we account for the common proportionality factor between the Green's function and the ANIRF, we use the superscript AN to refer to the ANIR tensor $\mathbf{G}^{AN}$ and we assume that $\hat{G}^{AN}_{TD} = \hat{G}^{AN}_{TR} = \hat{G}^{AN}_{DT} = \hat{G}^{AN}_{RT} = 0$ at all frequencies. Note that $\mathbf{G}^{AN}$ refers specifically to the Green tensor between two surface locations. We exploit the causal and anticausal symmetry of the Green's function (*Snieder*, 2004; *Bensen et al.*, 2007) by averaging the causal and anti-causal time series.

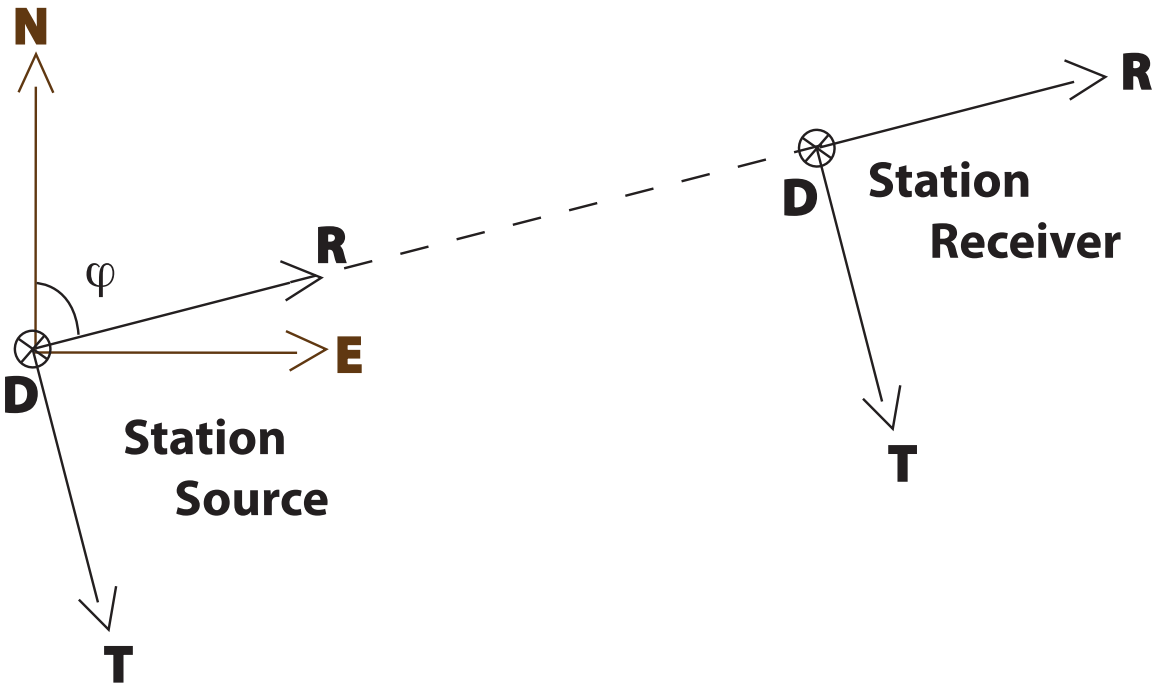

Figure 4.6: Coordinate system.

Location	M_w	Date	Latitude	Longitude	Depth	Virtual source	Latitude	Longitude	Range
Hector Road	5.06	12/06/2008	34.813°	-116.419°	5 km	HEC	34.829°	-116.335°	7.89 km
Chino Hills	5.39	07/29/2008	33.953°	-117.761 °	15 km	CHN	33.998°	-117.680°	9.03 km
San Bernardino	4.45	01/09/2009	34.107°	-117.304°	13.8 km	CLT	34.093°	-117.316°	1.98 km
San Fernando	4.24	09/01/2011	34.339°	-118.475°	7.3 km	LFP	34.305°	-118.488°	3.95 km

Table 4.1: Earthquake moment magnitudes, dates, and hypocenters from www.data.scec.org (*Hauksson et al.*, 2012); virtual source (seismic station closest to epicenter) locations; and range between epicenter and virtual source.

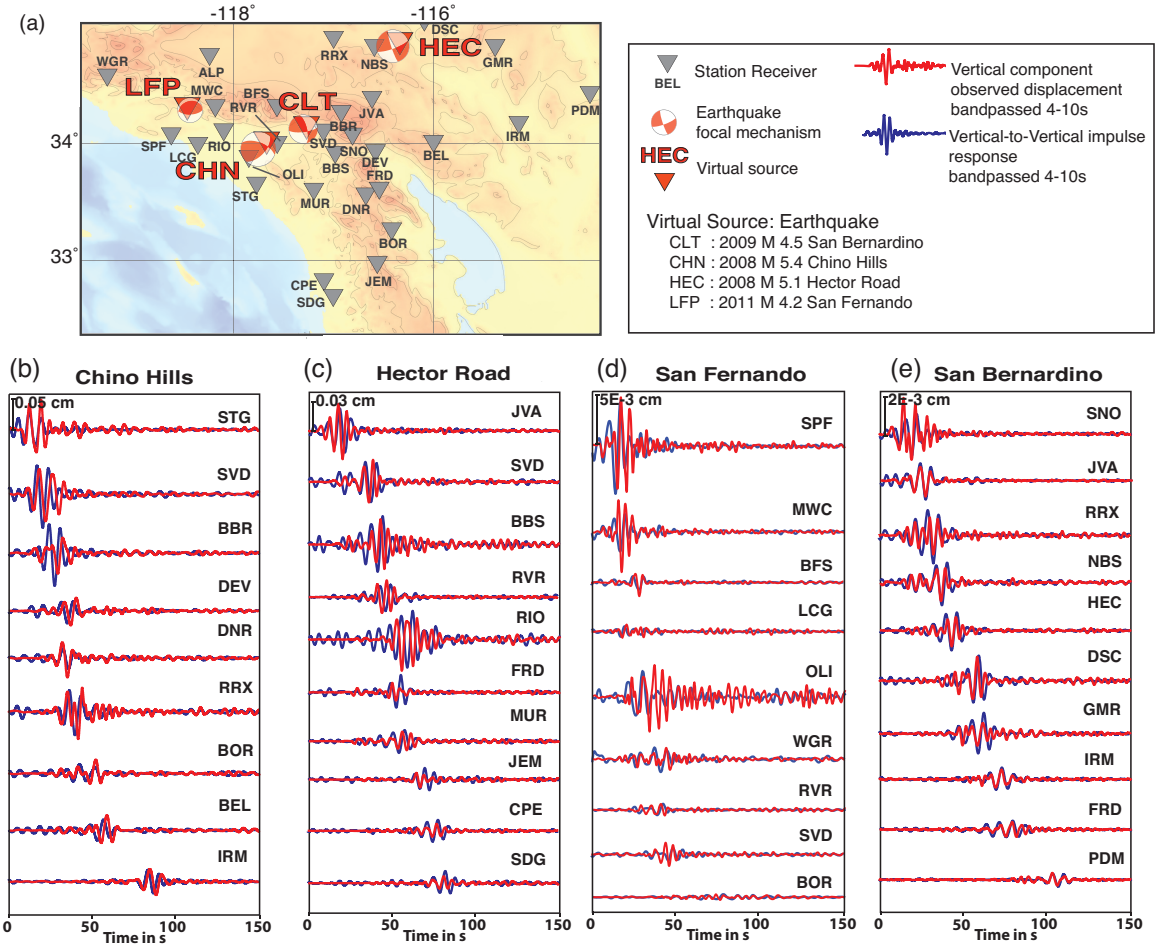

Figure 4.7: DD impulse responses compared with earthquake observations. We show in (a) the earthquake locations and mechanisms, the virtual sources, and the receiver locations. We show in (b)-(e) the vertical-to-vertical ANIRFs (in blue) against, the displacements (in cm) earthquake waveforms (in red), band passed 4–10 s, for Chino Hills, Hector Road, San Fernando, andSan Bernardino earthquakes respectively.

To verify that we retrieve correct path effects from the ANIR tensor, we compute the impulse responses from the stations closest to the four epicenters, or virtual sources: CHN for Chino Hills, HEC for Hector Road, LFP for San Fernando, and CLT for San Bernardino (see Table 4.1). First, we compare the vertical-to-vertical impulse responses with the vertical displacement earthquake records, band passed 4 – 10 s. We calibrate the ANIRFs to the observed displacement amplitudes using a normalization factor (peak displacement amplitude) common to all stations pairs

that accounts for the strength of the coherent signal traveling from the virtual source

We correct the ANIRF for the distance between the station source and the estimated epicenters, listed in Table 4.1, by using the phase velocity dispersion curve computed from GESC at the virtual source location.

In Figure 4.7, we show the similarity between the observed records and the vertical-to-vertical component of the ANIR tensor only. The horizontal components reveal similar results. By rotating the Green tensor into the RTD coordinate system, we align the orientation of the coordinate system into the maximum of the single-force radiation lobes. We therefore expect some misfit between the earthquake records that include the dislocation source mechanism radiation, and the impulse responses. However, in the 4 – 10 s period band, we see reasonable match of the amplitudes between both waveforms for the specific examples shown in Figure 4.7. This implies that the impulse responses capture, to the first order, the path effects from the virtual source as found by *Prieto and Beroza* (2008). Figures 4.7(b)–(e) illustrate the power of using the ANIRFs as a tool for ground motion prediction. The geometrical decay clearly dominates the surface-wave amplitudes; however, for receivers located in the Los Angeles Basin, the ANIRFs also capture the observed local surface-wave amplification (stations RIO in Figure 4.7(d) and OLI in Figure 4.7(e)) and extended duration.

Surface-wave excitation depends on the complexity of the velocity structure and is strongly frequency dependent. A source at the surface will more efficiently excite short period waves than a buried source. Therefore, for a better representation of earthquake ground motion, we have to correct the ANIRF for the effect of depth on the surface-wave excitation.

Correction for source depth

In this section, we focus on the fundamental surface-wave modes and assume that the medium surrounding the source can be approximated by a 1-D vertical structure. We express the surface-wave part of Green tensor in the RTD system as the contribution of both Rayleigh and Love waves:

$$\mathbf{G} \approx \mathbf{G}^L + \mathbf{G}^R = \begin{pmatrix} G_{RR} & 0 & G_{RD} \\ 0 & G_{TT} & 0 \\ G_{DR} & 0 & G_{DD} \end{pmatrix}. \tag{4.2}$$

We use the convention of *Aki and Richards* (2002) and derive the source-depth dependence of the Green tensor in cylindrical coordinates. For a surface receiver located at $\mathbf{x}$ and a source located at $\mathbf{x}'$, we define horizontal distance between the source and receiver r, azimuthal angle ϕ, and source depth h. To simplify the notation, we suppress explicit ω-dependence while retaining the source-depth dependence h. The Love-wave Green tensor is naturally expressed in the frequency domain as

$$\hat{\mathbf{G}}^L(h) = \frac{1}{8c_L U_L I_1}\sqrt{\frac{2}{\pi k_L r}} \begin{pmatrix} 0 & 0 & 0 \\ 0 & l_1(0)l_1(h) & 0 \\ 0 & 0 & 0 \end{pmatrix} \exp(i(k_L r + \pi/4)), \tag{4.3}$$

where $l_1(z)$ is the Love-wave displacement eigenfunction at depth z, c_L the phase velocity, U_L the group velocity, k_L the wavenumber, $I_1 = 1/2\int_0^\infty \rho(z) l_1^2(z) dz$ is the first energy integral. The Rayleigh-wave Green tensor is

$$\hat{\mathbf{G}}^R(h) = \frac{1}{8c_R U_R I_1}\sqrt{\frac{2}{\pi k_R r}} \begin{pmatrix} r_1(0)r_1(h) & 0 & -ir_1(0)r_2(h) \\ 0 & 0 & 0 \\ ir_2(0)r_1(h) & 0 & r_2(0)r_2(h) \end{pmatrix} \exp(i(k_R r + \pi/4)), \tag{4.4}$$

with similar notation as in the Love case; the Rayleigh-wave group velocity, phase velocity and wavenumbers have the subscript R and $I_1 = 1/2\int_0^\infty \rho(z)(r_1^2(z) + r_2^2(z))dz$. The horizontal and vertical displacement eigenfunctions, respectively $r_1(z)$ and $r_2(z)$, are frequency and depth dependent.

We note from equation 4.3 that

$$\hat{G}_{TT}(h) = \frac{l_1(h)}{l_1(0)}\hat{G}_{TT}(0). \tag{4.5}$$

For Love waves, 4.5 shows a linear relationship between the Green tensor component for a source at depth and the Green tensor component for a source at the surface. The correction factor is the ratio of the displacement eigenfunctions taken at the source depth and surface. The ambient noise Green tensor $\mathbf{G}^{AN}$ contains the information on the surface-wave 3-D propagation in the true complex crustal structure. We replace $G_{TT}(0)$ with G^{AN}_{TT} to obtain

$$\hat{G}_{TT}(h) \approx \frac{l_1(h)}{l_1(0)}\hat{G}^{AN}_{TT}. \tag{4.6}$$

This relation is always stable, in the sense that division by zero or nearly zero is avoided, because the Love-wave displacement eigenfunctions are nonzero at the surface.

For the Rayleigh-wave components of the Green tensor, we have analogous expressions:

$$\hat{G}_{RR}(h) \approx \frac{r_1(h)}{r_1(0)}\hat{G}^{AN}_{RR} \quad \text{and} \quad \hat{G}_{RD}(h) \approx \frac{r_2(h)}{r_2(0)}\hat{G}^{AN}_{RD} \tag{4.7}$$

$$\hat{G}_{DR}(h) \approx \frac{r_1(h)}{r_1(0)}\hat{G}^{AN}_{DR} \quad \text{and} \quad \hat{G}_{DD}(h) \approx \frac{r_2(h)}{r_2(0)}\hat{G}^{AN}_{DD} \tag{4.8}$$

These relationships are stable in most cases for similar reasons. *Tanimoto and Rivera* (2005) and *Denolle et al.* (2012), however, highlight changes from the usual retrograde to prograde Rayleigh-wave particle motion at the free surface for certain velocity models and frequencies. In such cases, the $r_2(0)$ can be small (or even zero) and this correction becomes ill-conditioned. We have preliminary results on where we should expect those changes, which we expand in Chapter 3. In this particular case,

however, we use the Southern California Earthquake Center Community Velocity Model Version 4.0 (CVM4.0) (*Magistrale et al.*, 2000) for which we do not see such changes in particle motion at the frequencies of interest.

We extract from CVM4.0 the velocity profiles at the four seismic stations closest to the epicenters and represent them in Figure 4.8(a). Table 4.1 contains the locations of the earthquake hypocenters (*Hauksson et al.*, 2012) with their respective virtual source (seismic station) name and location. LFP, CHN, and CLT are located in sedimentary basins, which involve strong velocity gradients at shallow depth. HEC is located in the Mojave Desert, and presents characteristics of the shallow crust that are closer to bedrock. The Hector Road event occurred shallow (∼5 km) on a strike-slip fault that accommodates part of the distributed right-lateral motion of the Eastern California Shear Zone (*Savage et al.*, 2001). The Chino Hills earthquake occurred on the blind thrust underlying the sedimentary basin (*Hauksson et al.*, 2008) at greater depth (∼15 km), whereas the San Bernardino earthquake, with similar depth, is near the deepest part of the San Andreas Fault system. The 2011 San Fernando earthquake occurred at ∼7.3 km near the location of the 1994 M 6.7 Northridge earthquake.

We represent in Figure 4.8 the source-depth correction to the Green tensor in the 1-D approximation. The dominant pattern of this correction (right panel of Fig. 4.8) is the filtering of the high frequencies for sources at depth. For the radial components, the second feature to note is the change of sign in the spectral correction related to the frequency-dependent zero crossing of the radial eigenfunction at depth.

Radiation pattern correction

We write the surface-wave displacements, $\hat{u}_i$, at $\mathbf{x}$ generated by a point source described by the moment tensor $\hat{\mathbf{M}}$ at the source located at $\mathbf{x}'$ as

$$\hat{u}_i(\mathbf{x}) = \hat{M}_{pq} \frac{\partial}{\partial x'_q} \hat{G}_{ip}(\mathbf{x}, \mathbf{x}'). \tag{4.9}$$

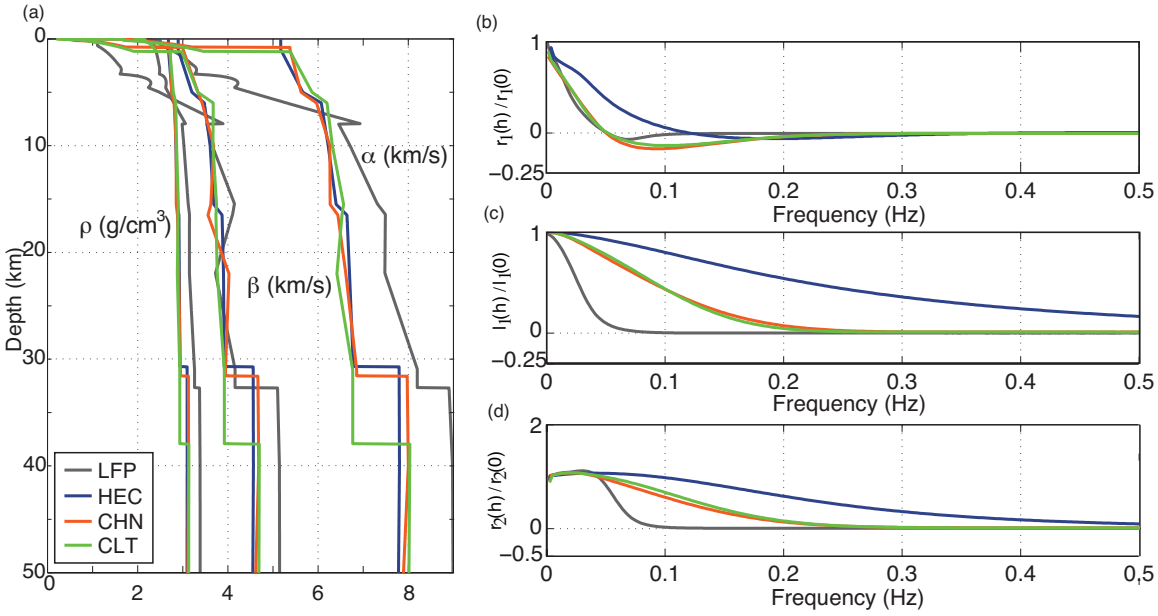

Figure 4.8: (a) Velocity and density profiles under seismic stations LFP, HEC, CLT, and CHN. (b)–(d) Ratio of the radial (Rayleigh), transverse (Love), and vertical (Rayleigh) displacement eigenfunctions taken at the source depth and the surface for the four respective seismic stations located closest to the earthquakes of interest.

Assuming that $\hat{\mathbf{G}}$ can be expressed in the form given in equations (4.2)-(4.4), we follow *Aki and Richards* (2002), assuming that the largest contributions are from depth derivatives of the eigenfunctions and the horizontal derivatives of $\exp(ikr)$. We rotate the coordinate system from NED to RTD and under the approximation described earlier, simplify the horizontal partial derivatives to:

$$\frac{\partial \hat{G}}{\partial R} = -ik\hat{G} \quad \text{and} \quad \frac{\partial \hat{G}}{\partial T} = 0. \tag{4.10}$$

For Love waves, we expand (4.9) using the depth-corrected Green tensor $\hat{\mathbf{G}}(h)$ and approximate:

$$\hat{u}_T = \hat{M}_{TD} \frac{\partial \hat{G}_{TT}}{\partial Z}\Big|_{Z=h} - ik_L \hat{M}_{TR} \hat{G}_{TT}(h). \tag{4.11}$$

From equation 4.3, we see that

$$\frac{\partial \hat{G}_{TT}}{\partial Z}\Big|_{Z=h} = \frac{l_1'(h)}{l_1(h)}\hat{G}_{TT}(h) = \frac{l_1'(h)}{l_1(0)}\hat{G}_{TT}(0). \tag{4.12}$$

And approximating $\hat{G}_{TT}(0) \approx \hat{G}^{AN}_{TT}$,

$$\hat{u}_T \approx \frac{1}{l_1(0)}\left[-ik_L\hat{M}_{TR}l_1(h) + \hat{M}_{TD}l_1'(h)\right]\hat{G}^{AN}_{TT}. \tag{4.13}$$

In a similar manner, one can show that for Rayleigh waves,

$$\begin{aligned}
\hat{u}_D &\approx \frac{1}{r_1(0)}\left[-ik_R\hat{M}_{RR}r_1(h) + \hat{M}_{RD}r_1'(h)\right]\hat{G}^{AN}_{DD} \qquad (4.14)\\
&\quad + \frac{1}{r_2(0)}\left[-ik_R\hat{M}_{DR}r_2(h) + \hat{M}_{DD}r_2'(h)\right]\hat{G}^{AN}_{DD},\\
\hat{u}_R &\approx \frac{1}{r_2(0)}\left[-ik_R\hat{M}_{DR}r_2(h) + \hat{M}_{DD}r_2'(h)\right]\hat{G}^{AN}_{RD} \qquad (4.15)\\
&\quad + \frac{1}{r_1(0)}\left[-ik_R\hat{M}_{RR}r_1(h) + \hat{M}_{RD}r_1'(h)\right]\hat{G}^{AN}_{RR}.
\end{aligned}$$

For Rayleigh waves, the conditioning of the correction strongly depends on the particle motion at the surface. The vertical displacement eigenfunction $r_2(0)$ becomes zero when particle motion changes from retrograde to prograde (and vice versa). Those changes introduce singularities in the conversion, that we do not encounter for the frequencies of interest when using CVM4.0.

We see that equations 4.13 and 4.16 relate the ANIR tensor components to the earthquake displacements with three main factors depending on the vertical, radial or transverse components. We represent their absolute values at given periods (5, 7 and 10 s) in Figure 4.9 and their variations with respect to azimuth and frequency of the source-depth and double-couple correction with a flat moment-rate function

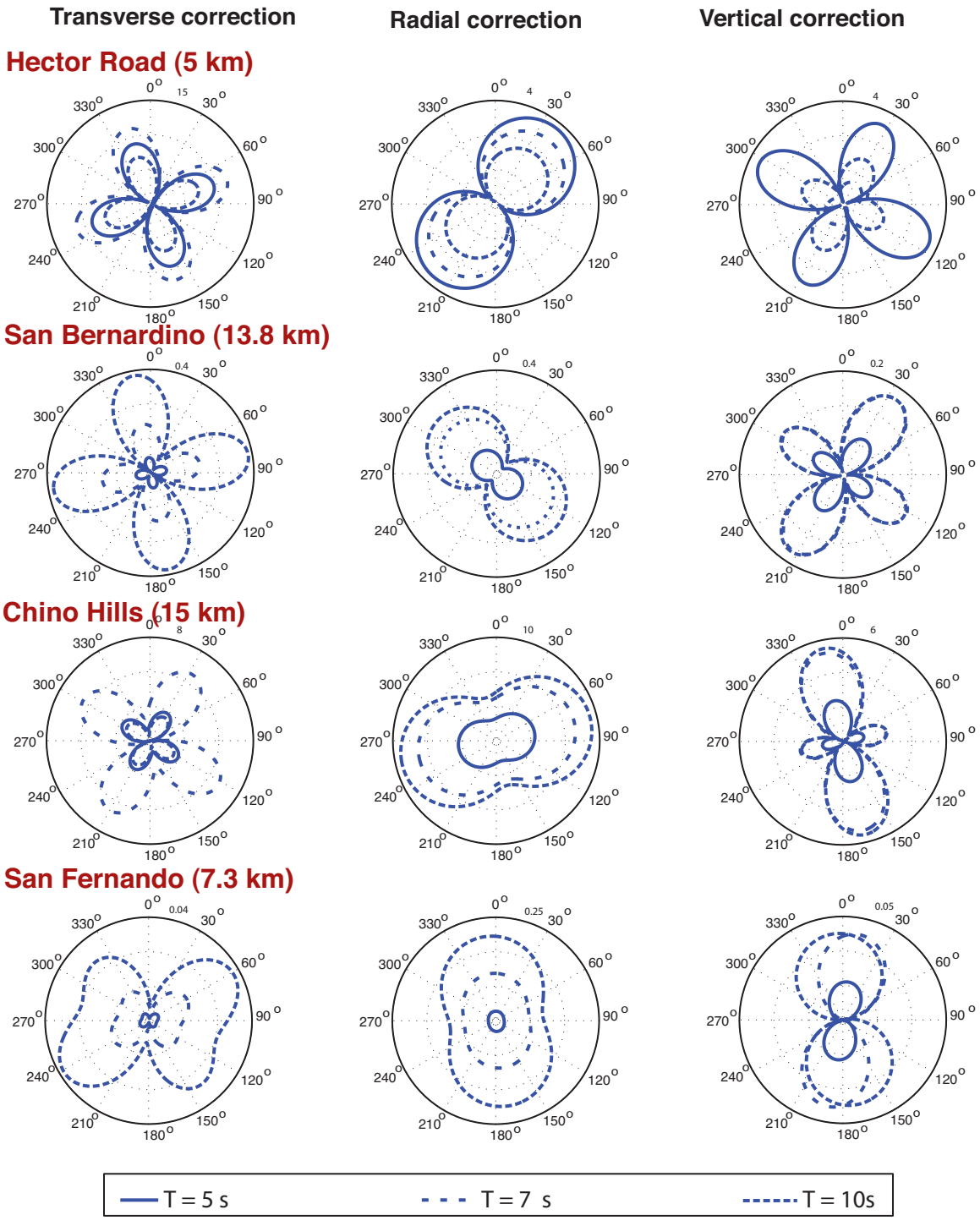

Figure 4.9: Correction terms to convert surface-impulse responses to buried double-couple radiation (displacements). The absolute values of the three factors of conversion described in (4.13) and (4.16) are shown in polar plots and their azimuth and period dependence using the four earthquake moment tensors listed in Table 4.2. For each polar representation, the maximum amplitude is shown at azimuth 15°. We impose a flat response of the moment-rate function at those periods.

Virtual source	Mo	Mxx	Mxy	Mxz	Myy	Myz	Mzz	f_c
HEC	4.9×10^{16} Nm	-2.749	-3.734	-0.959	3.052	-0.902	-0.304	0.58 Hz
CHN	1.53×10^{17} Nm	-14.17	4.9	-1.9	5.85	-7.39	8.32	0.39 Hz
CLT	5.96×10^{15} Nm	-0.2507	-0.4974	0.1639	0.1259	-0.1828	0.1248	1.17 Hz
LFP	1.74×10^{15} Nm	-0.14487	-0.02634	0.09129	-0.0004	-0.0116	0.14574	1.71 Hz

Table 4.2: Virtual source parameters: Seismic moment, deviatoric solution of the moment tensor (from SCSN, normalized to 10^{16} Nm with the convention of z positive downward), and estimated corner frequency f_c.

spectrum. The effect of the source depth is clearly expressed because buried sources excite short-period surface waves less efficiently than shallower sources. The other main feature illustrated in Figure 4.9 is the presence of four lobes at the transverse and vertical components for the pure strike-slip events (Hector Road and San Bernardino).

As mentioned earlier, the 2008 M 5.1 Hector Road earthquake occurred in the Eastern California Shear Zone and the moment tensor solution exhibits almost pure strike-slip (Fig. 4.7(a)) motion. The 2009 M 5.4 Chino Hills and 2009 M 4.5 San Bernardino earthquake mechanisms feature oblique strike-slip motion, as shown in (Fig. 4.7(a)). The 2011 M 4.2 San Fernando earthquake mechanism is almost almost pure reverse faulting.

Source pulse

In this study, we choose earthquakes of moderate magnitude so that finite-fault effects are minor at the periods of interest. There is a trade-off, however, because we require adequate signal-to-noise ratio at longer periods. Earthquakes in the range of M 4.5-5.5 provide a good balance between these two considerations. We account for the finite duration of the event with an assumed pulse width for the moment rate function. The duration T of the pulse is controlled by the corner frequency such that $T = 1/2f_c$. We estimate the corner frequency of the events based on *Hanks and Thatcher* (1972) with an assumed stress drop $\Delta\sigma = 3$ MPa, the observed seismic moment, M_0, and shear velocity $\beta = 3$ km/s:

$$f_c = 0.491\beta \left(\frac{\Delta\sigma}{M_0} \right)^{1/3}. \tag{4.16}$$

We list each earthquake corner frequency in Table 4.2. In the far-field approximation, the displacement field is proportional to the moment-rate function. We use a parabolic moment-rate function (*Herrmann*, 1978) with the Fourier spectrum

$$\hat{S}(\omega) = \exp(-i\omega T/2) \frac{4\sin^2(\omega T/8)\sin(\omega T/4)}{(\omega T/4)^3}, \tag{4.17}$$

where the moment-rate function $\dot{M}_0(t) = M_0 S(t)$ is shown in Figure 4.10.

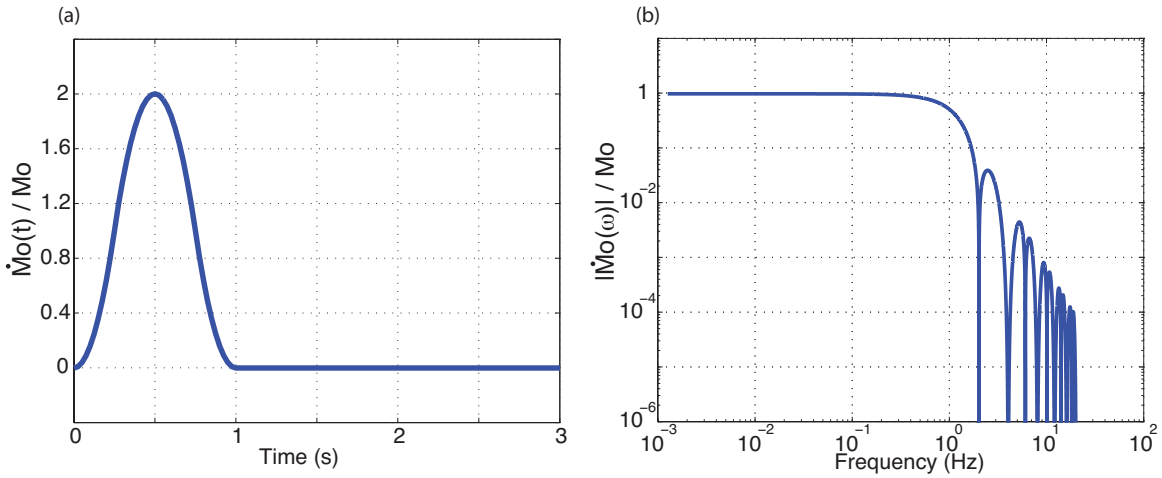

Figure 4.10: Normalized moment-rate function (a) and spectrum (b) for a corner frequency $f_c = 0.5\ Hz$.

Validating the virtual earthquake approach with seismic observations

We have shown how to incorporate the effects of more realistic source parameters in the ANIRFs to produce far-field surface-wave seismograms for a buried double-couple source that can be directly compared with earthquake observations. Once we account for the source depth, double-couple mechanism, and finite duration of the moment-rate pulse, we have constructed the virtual earthquake. To validate what we refer to as the Virtual Earthquake Approach (VEA), we compare the virtual earthquake seismograms with the earthquake records, between 4 and 10 s period.

The epicenters are not exactly collocated with the station source (Table 4.1); the distance between these and the seismic stations varies between 3 and 8 km. We combine the estimated surface-wave dispersion information, taken at the virtual source, and the difference between epicenter-receiver and virtual source-receiver locations to account for the expected time shift. For the earthquakes considered, this correction is as large as 3 s, which is significant over the period band of interest.

In making this comparison, we need to account for several sources of uncertainty in our system. First, we approximate the moment rate pulse width based on an assumed corner frequency, which we calculate for constant stress drop of 3 MPa despite its expected strong variability (*Baltay et al.*, 2011). Depending on the seismic moment and stress drop, the time delay due to the finite width of the pulse ranges between 0.3 and 1 s. This particular source of uncertainty will be consistent over the entire seismic network. Second, we use the surface-wave eigenfunctions for a 1-D velocity profile at the station source. By comparing velocity profiles from CVM4.0 at the epicenter and station-source locations, we find variations in phase velocity that lead to variations in the phase shift of at most 2-3 s for stronger variations in the velocity structure. Finally, we allow for arrival time uncertainty of 0.2 s due to the SCSN hypocenter location uncertainties. We combine the possible effects of all these uncertainties by allowing a conservative free phase shift of 1.5 s to maximize the correlation between the between the virtual and real earthquake waveforms. To isolate the changes in the waveforms only due to the VEA, we also correct the initial IRFs in the same way by

allowing the station source and the epicenter the same 1.5 s shift.

For each earthquake and each component, we calibrate the ANIR tensor and VEA waveform amplitudes with the earthquake records by taking the peak displacement amplitudes (between 4 – 10 s), averaged over all the station pairs. To first order, this normalization accounts for the difference in strength of coherence between the virtual source and receivers.

We show in Figures 4.11, 4.15, 4.18, and 4.21 comparisons between the earthquake displacement waveforms, the initial impulse responses (diagonal terms of the Green tensor), and the displacements calculated with the VEA, all band passed from 4–10 s. The VEA waveforms show a much better fit to the earthquake records for all three components for most of the stations. The initial IRFs show strong similarity with the waveforms, both in phase and amplitude, for the San Bernardino and San Fernando earthquakes. This occurs because the diagonal terms significantly dominate the response to the buried double couple for these two examples. We find greater improvement for the Hector Road and Chino Hills events, where the diagonal terms do not dominate.

To evaluate the waveform fit, we calculate the normalized correlation coefficient (CC) for each component and at each station, between the ambient-noise derived responses $\mathbf{u}$ and the earthquake records $\mathbf{v}$. We compute this coefficient on a variable time window that contains most of the surface-wave energy. We calculate the cumulative energy (in the root mean square sense) of the waveform and select the time window that contains between 1% of the energy and 90%. This adaptive window directly allows us to account for complex path effects, as we compare late coda of predicted ground motion and observed waveforms. We index those respectively N_1 and N_{90}. The correlation coefficient at each station is then:

$$CC = \frac{\sum_{i=N_1}^{N_{90}} u_i v_i}{\sqrt{\sum_{i=N_1}^{N_{90}} u_i^2 \sum_{i=N_1}^{N_{90}} v_i^2}}. \tag{4.18}$$

For each earthquake (Fig. 4.12, 4.16, 4.19, 4.22), we show a map view of the CCs across southern California. For the smaller earthquakes (San Bernardino in Figure 4.19 and San Fernando in Figure 4.21), the correlation is initially high on all three components, as explained earlier, validating again the use of the ambient seismic field for ground motion prediction. For these earthquakes, the conversion between surface-impulse response to buried dislocation preserves the goodness of fit between the observed data and the ANIRFs. For Hector Road (Fig. 4.12) and Chino Hills (Fig. 4.16) events, there is no obvious correlation between the diagonal terms of the ANIR tensor and the observed waveforms. The VEA clearly improves the accuracy of the predicted ground motion relative to the ambient noise surface impulse responses. Apart from isolated cases, all the correlations between the new waveforms and the earthquake records are positive at most stations and components.

We can represent the CCs distribution in another, more quantitative way. In Figures 4.13, 4.17, 4.20, and 4.23, we show the distribution of the CC values. The top panels describe the ranges of CCs for all four earthquakes between the diagonal terms of the Green tensor and the observed waveforms. We find positive correlations for the San Fernando and San Bernardino events, and the apparent lack of appropriate radiation pattern for the Hector Road and Chino Hills events. This latter confirms the need to account for correct source mechanism. The bottom panels show the results of applying our technique to the ANIRFs, and the overall improvement. We confirm that the VEA waveforms show overall a good match in the phase of the observed records.

For a better understanding of the accuracy of the VEA-predicted amplitudes we show in Figure 4.14 peak amplitudes for the virtual and real earthquake waveforms for the four events. There is a good match between the observed and predicted amplitudes despite the scatter, which is somewhat expected by the scatter in the initial ANIRF shown in Figures 4.2–4.5. We estimate the best fitting linear trend, using L_1 norm minimization between the predicted and observed peak amplitudes. The slopes, indicated in Figure 4.14, are close to one: 1.04 for San Fernando, 1.04 for San Bernardino, 0.95 for Hector Road, and 1.10 for Chino Hills. This clearly shows, again, that the VEA predicts, along with the correct phase, reliable amplitudes.

There are several explanations for the isolated cases where we do not see a good match between observed and predicted displacements. Even though we retrieve the 3-D path effects from the ambient noise Green's functions, the 1-D approximation around the source ignores potential coupling between Love and Rayleigh waves that would occur locally for highly heterogenous media. The rotation from the NED framework to the RTD coordinate system assumes straight ray path between the source and the receiver, which is only strictly valid for laterally homogeneous half space. Moreover, the accuracy of the velocity profiles extracted at the virtual source locations is somewhat uncertain. Local noise may affect certain components of the ANIR tensor, and hence, the overall accuracy of the resulting VEA displacements. Finally, we used a far-field approximation for the expression of the surface-wave displacement, and this method requires modification for receivers within a wavelength of the epicenters. In parallel to Figure 4.7, the summary Figure 4.24 demonstrates the potential of the VEA for ground motion prediction.

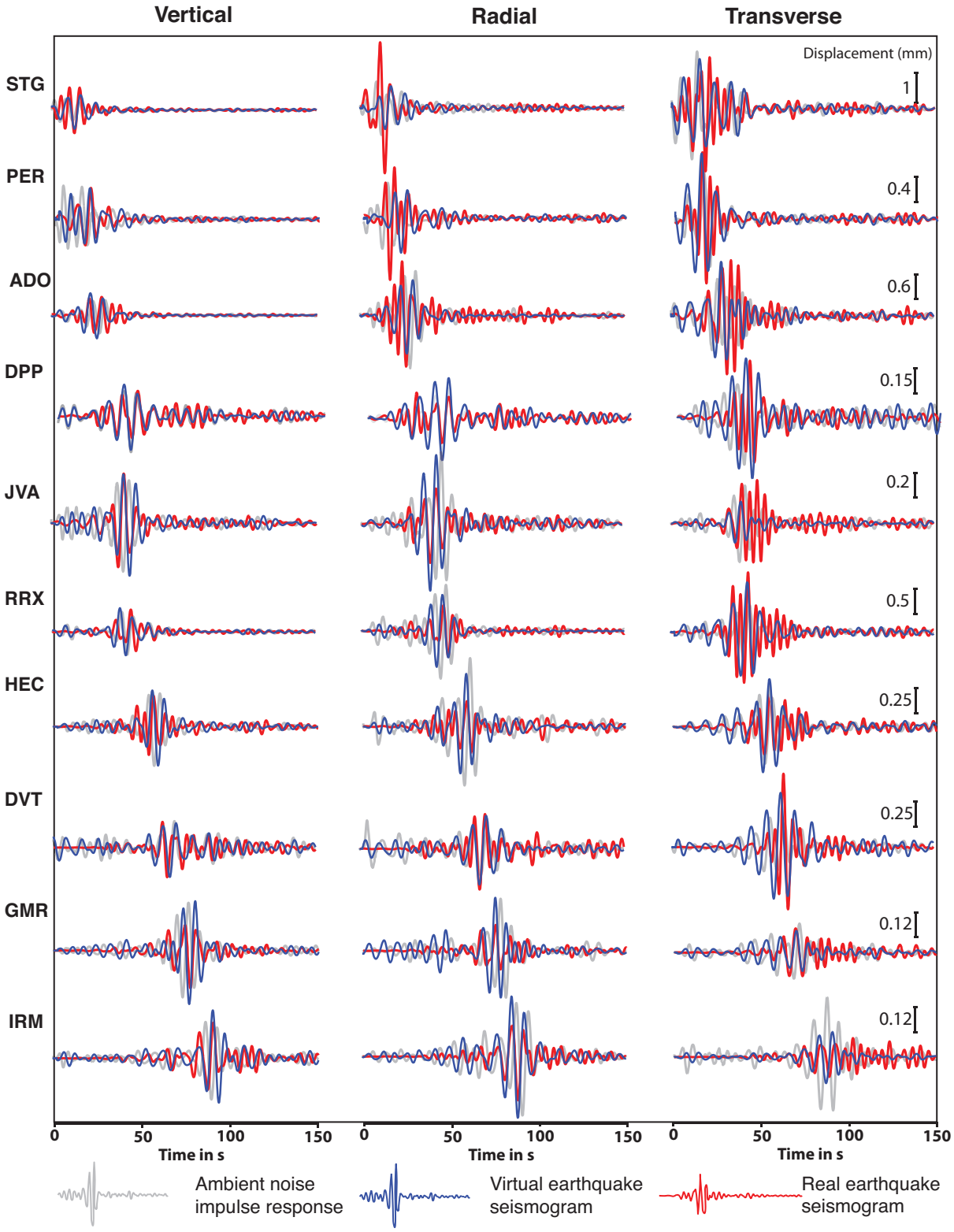

Figure 4.11: Waveform comparison, band passed 4 – 10 s, for the 2008 M 5.4 Chino Hills earthquake for all three components: the initial diagonal terms of the ANIRF tensor (DD, RR, and TT in gray), the earthquake records (D, R, and T in red) and the VEA waveforms (D, R, and T in blue). We show the receiver locations in the black upside-down triangles in all panels of Figure 4.12.

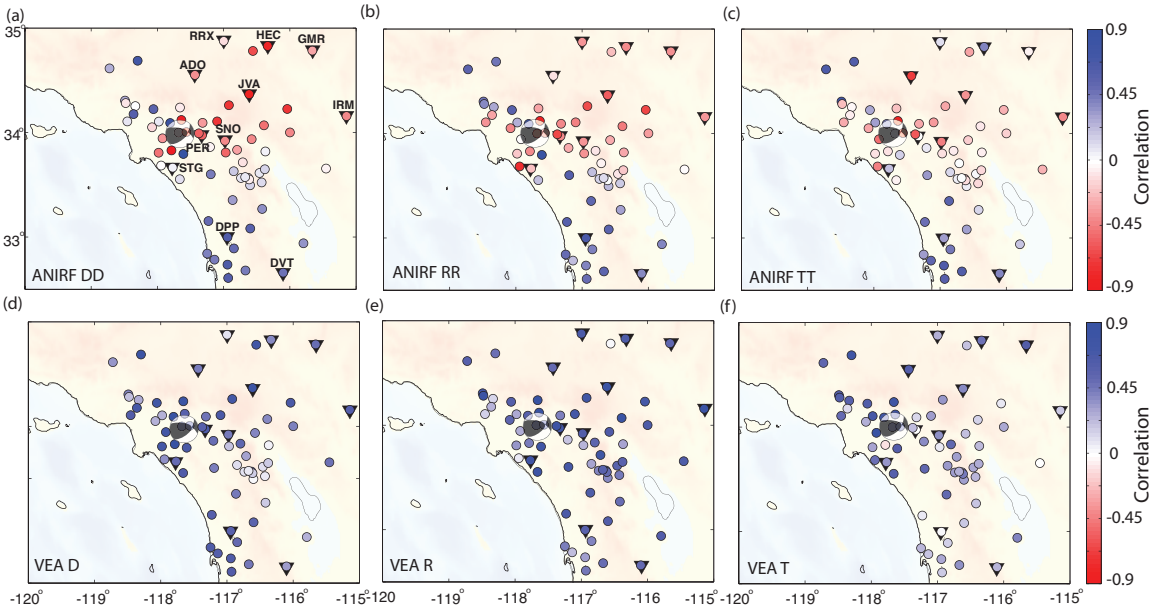

Figure 4.12: Maps representing the spatial distribution of the normalized correlation coefficients (CCs) between the predicted and observed waveforms, at each receiver, for the 2008 M 5.4 Chino Hills earthquake. The colorscale shows the CC values ranging between -0.9 (red) and 0.9 (blue). The top panels show the correlation between the initial ANIRFs and observed displacements at all three components: DD (a), RR (b), and TT (c). The black upside-down triangles show the locations of the receivers used in Figure 4.11. The bottom panels show the correlation between the VEA and the earthquake waveforms at all three components D (d), R (e) and T (f).

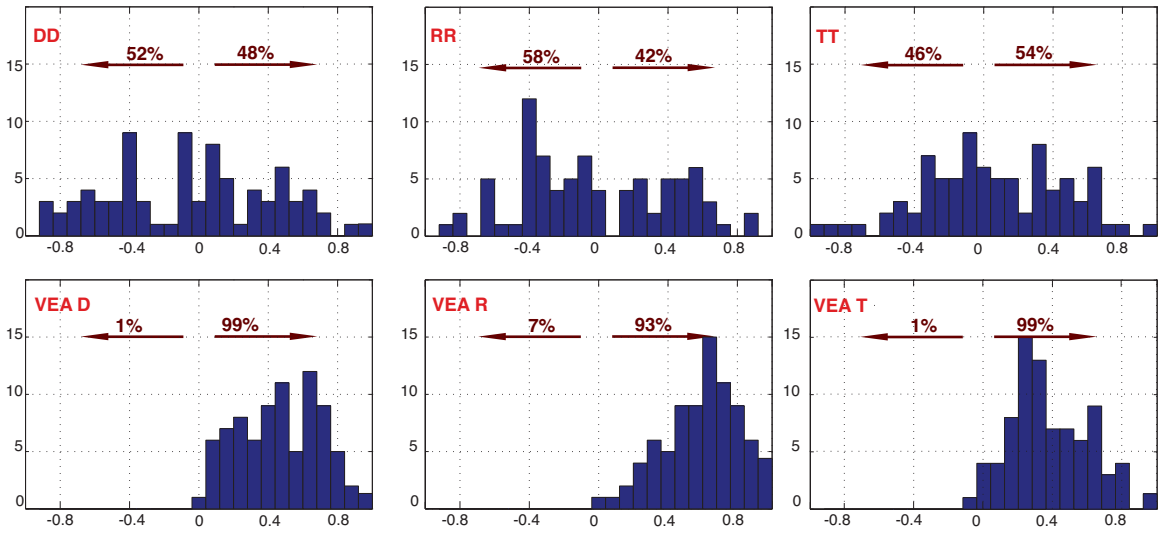

Figure 4.13: Histograms of the correlation coefficients for 2008 M 5.4 Chino Hills earthquake at all three components (from left to right: R, T and D): the CC values for the initial ANIRFs diagonal components on the top panels, the CC values for the VEA waveforms in the middle panels. The bottom panels show consistently better fits to the earthquake data than the upper panels.

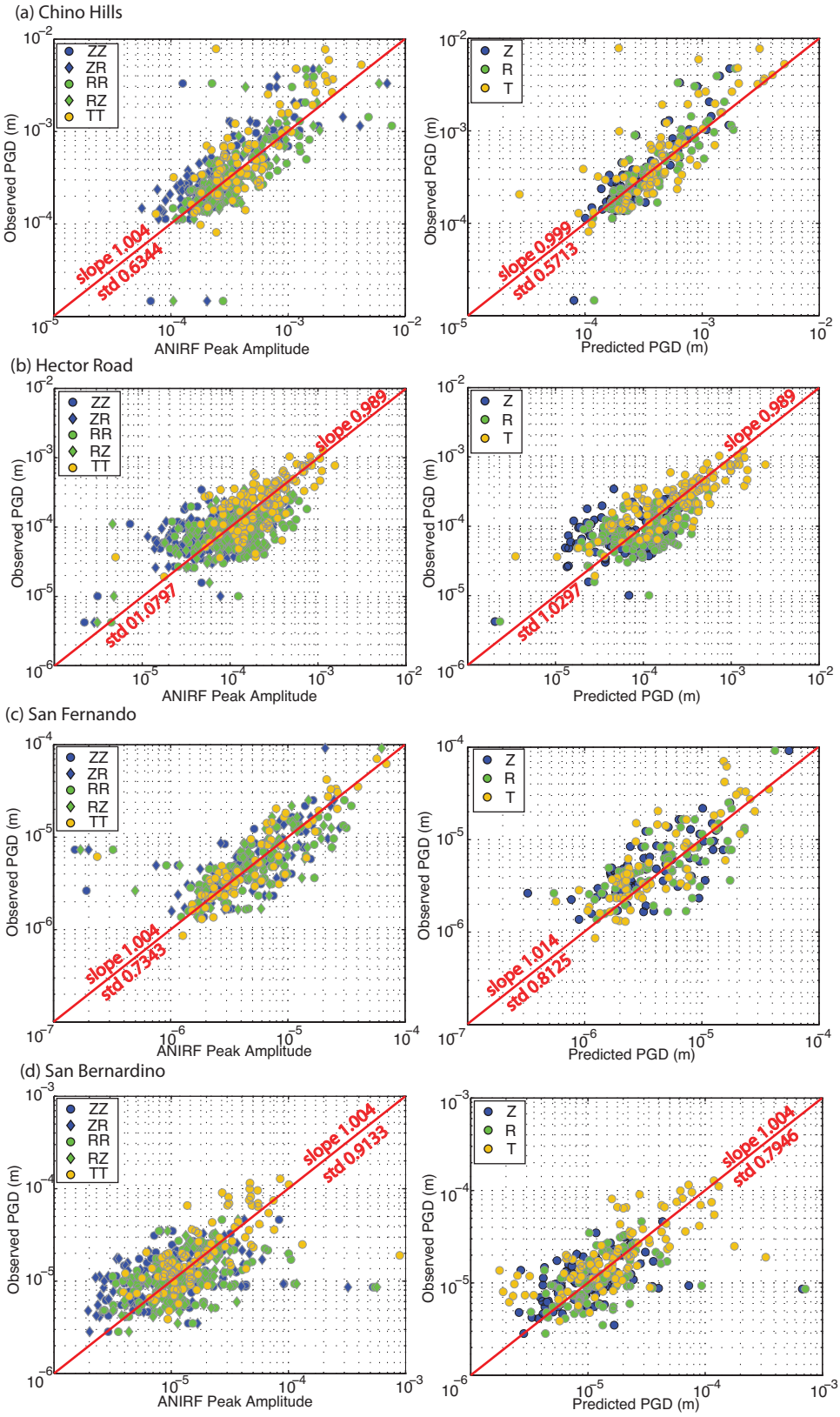

Figure 4.14: Observed and predicted peak amplitudes, filtered 4–10 s, at all stations for all four earthquakes: (a) Chino Hills, b) Hector Road, c) San Bernardino, and d) San Fernando. We compare the vertical (blue), radial (green) and tangential (yellow)

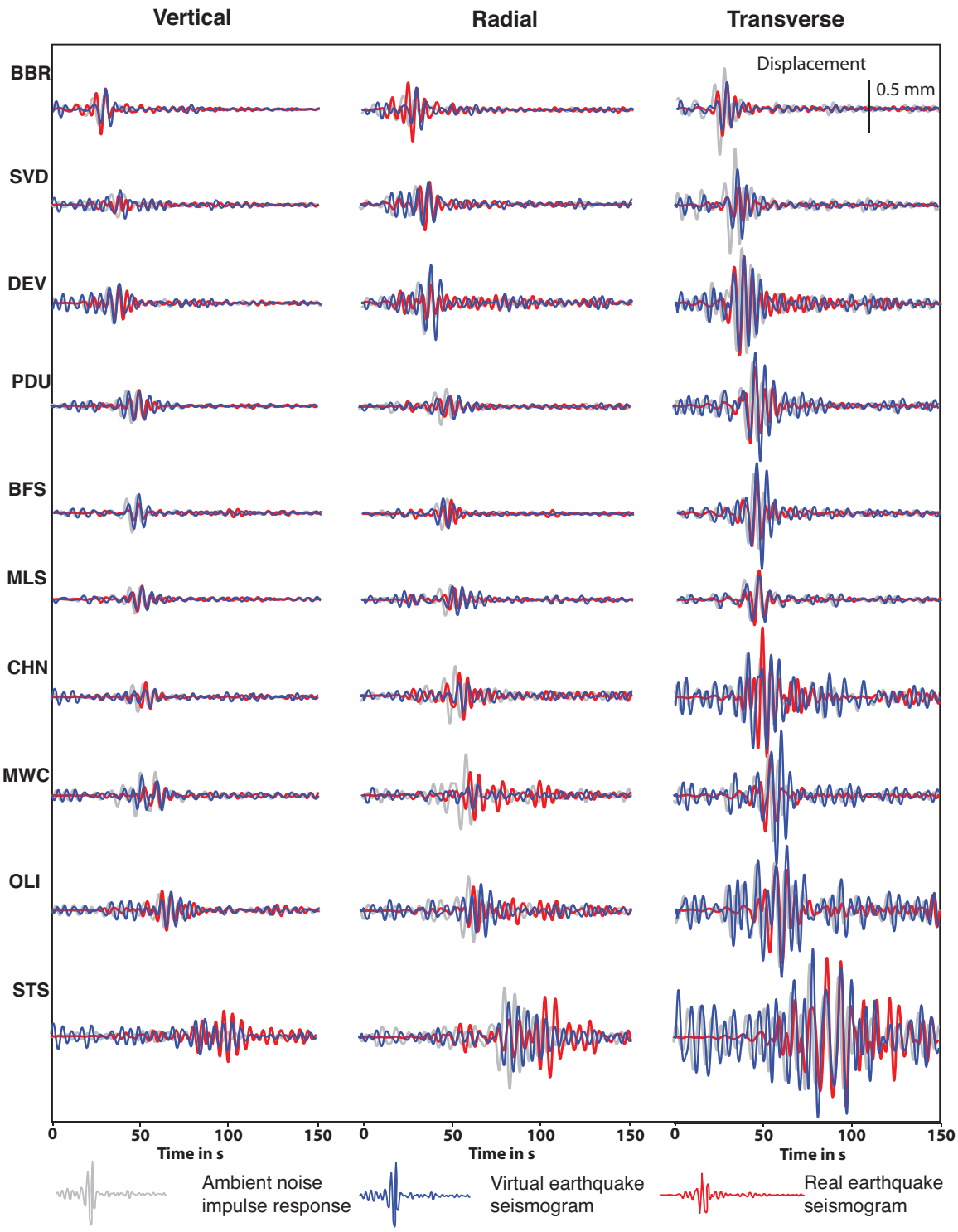

Figure 4.15: Same as Figure 4.11 for the 2008 M 5.1 Hector Road earthquake.

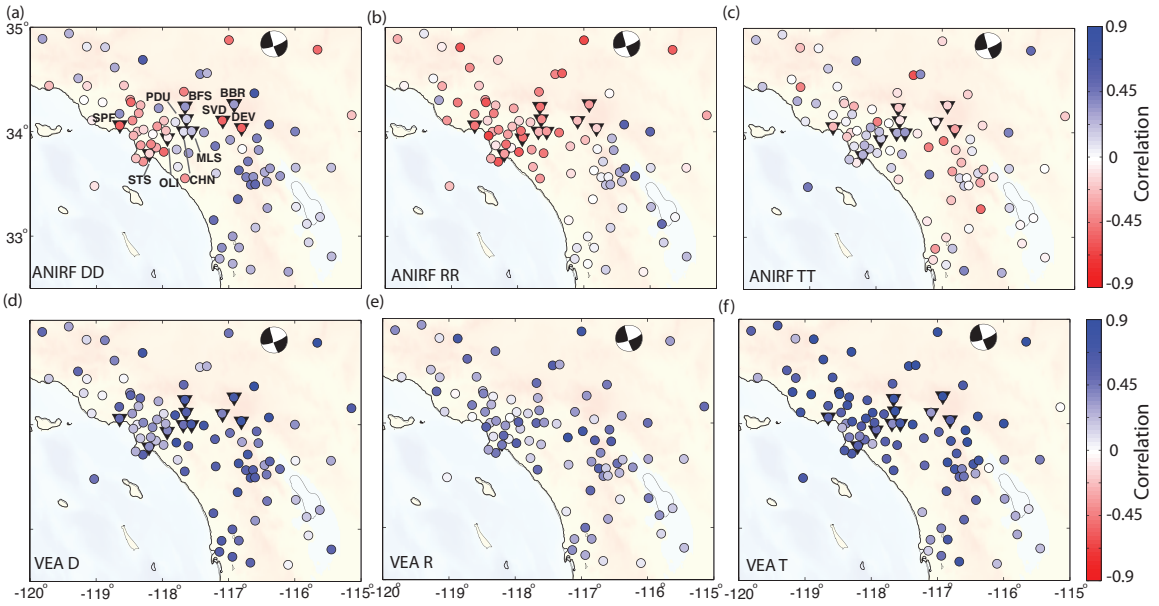

Figure 4.16: Same as Figure 4.12 for the 2008 M 5.1 Hector Road earthquake.

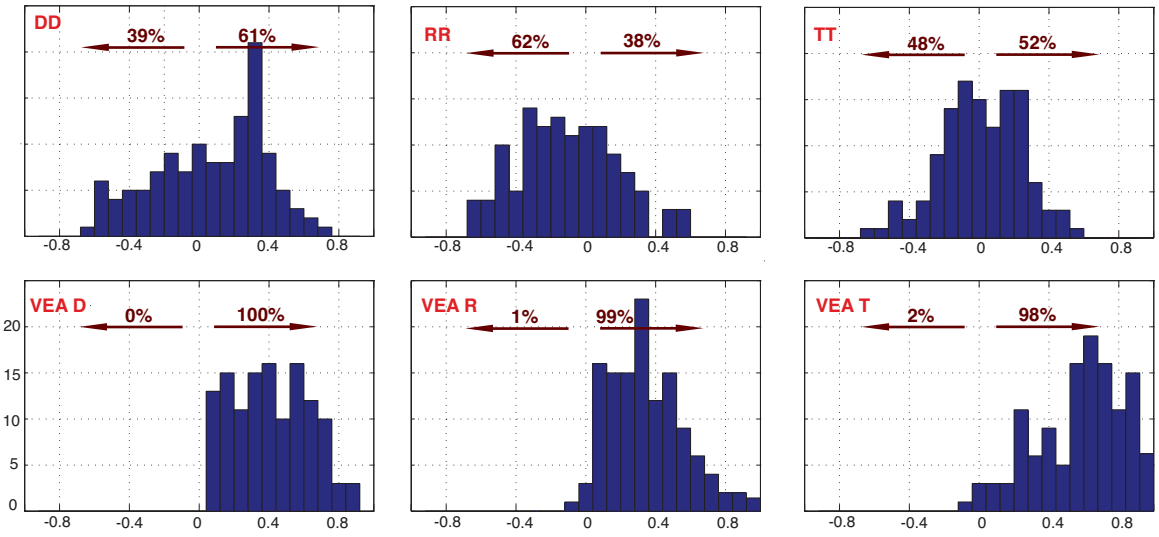

Figure 4.17: Same as Figure 4.13 for the 2008 M 5.1 Hector Road earthquake.

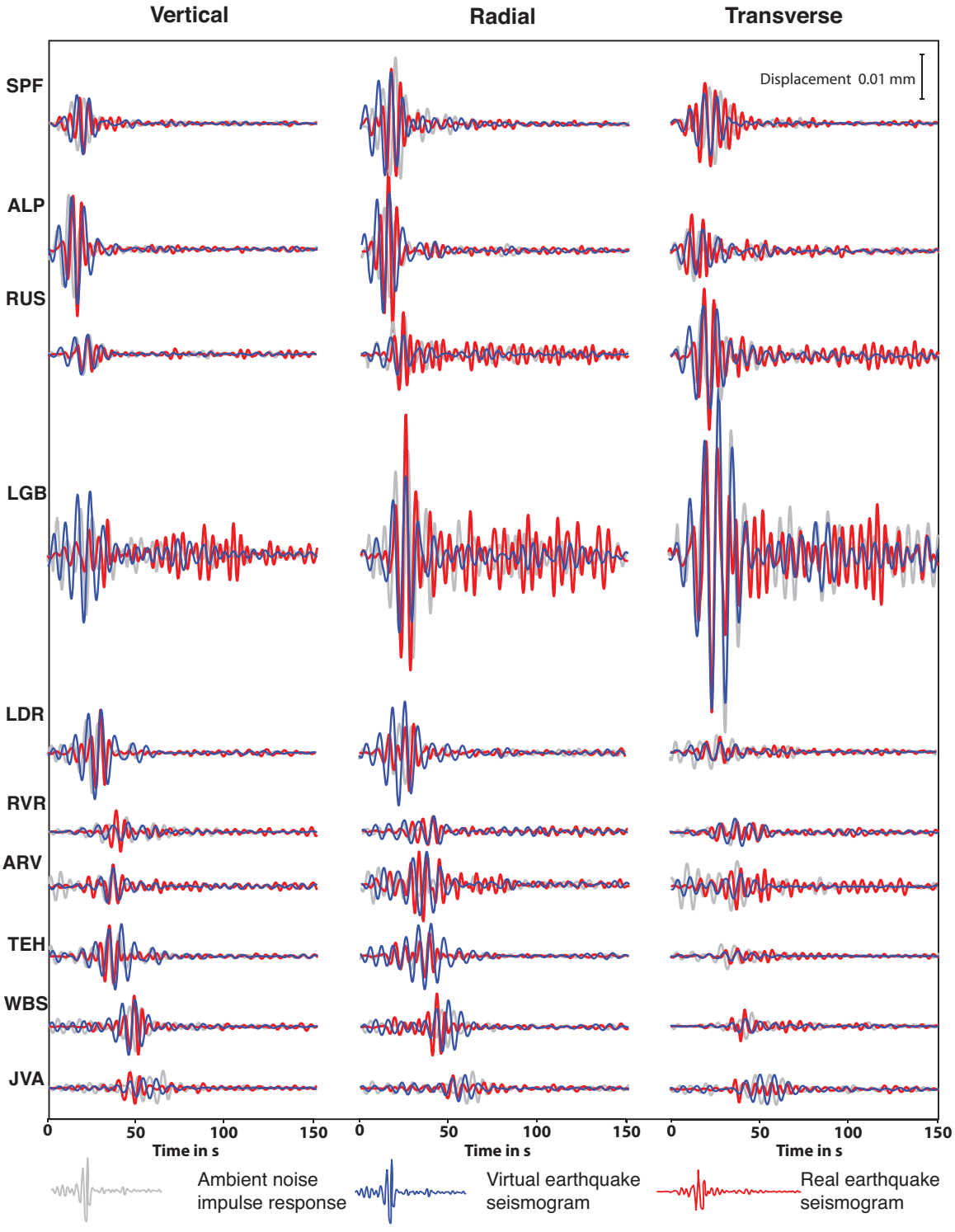

Figure 4.18: Same as Figure 4.11 for the 2011 M 4.2 San Fernando earthquake.

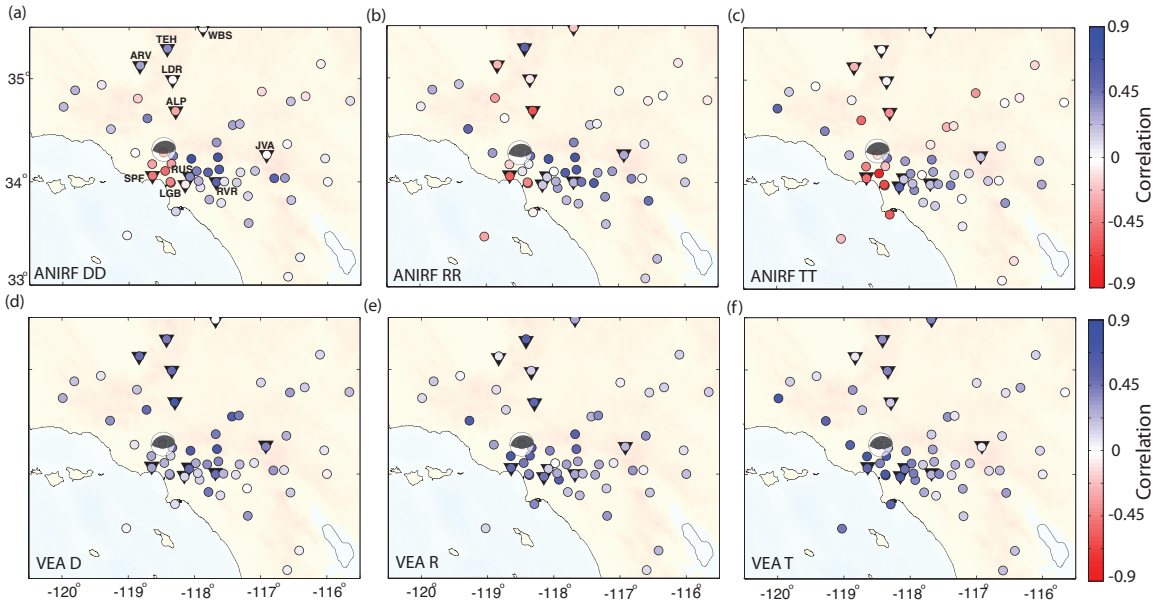

Figure 4.19: Same as Figure 4.12 for the 2011 M 4.2 San Fernando earthquake.

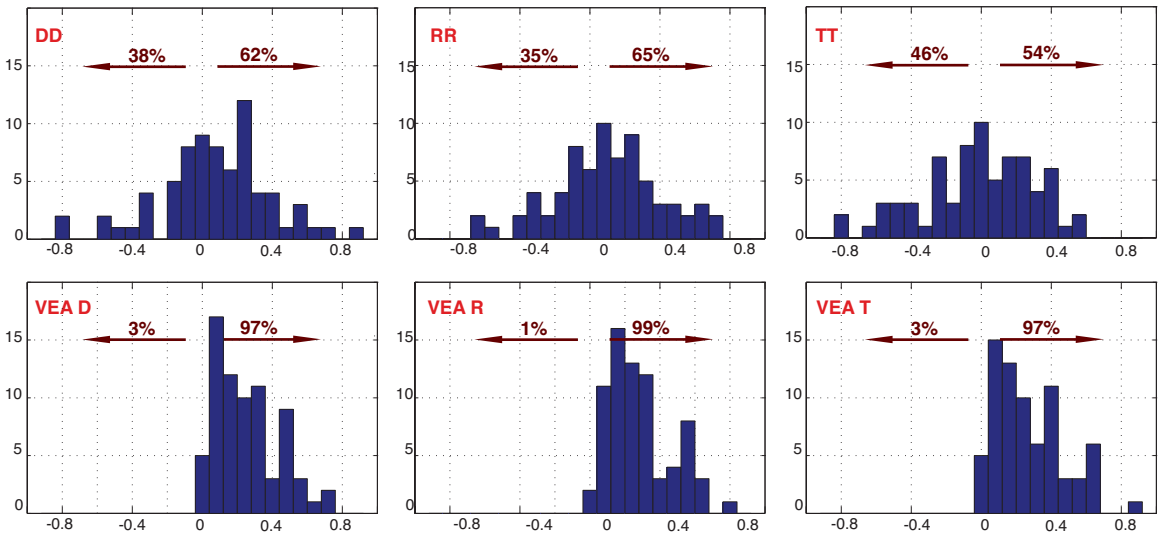

Figure 4.20: Same as Figure 4.13 for the 2011 M 4.2 San Fernando earthquake.

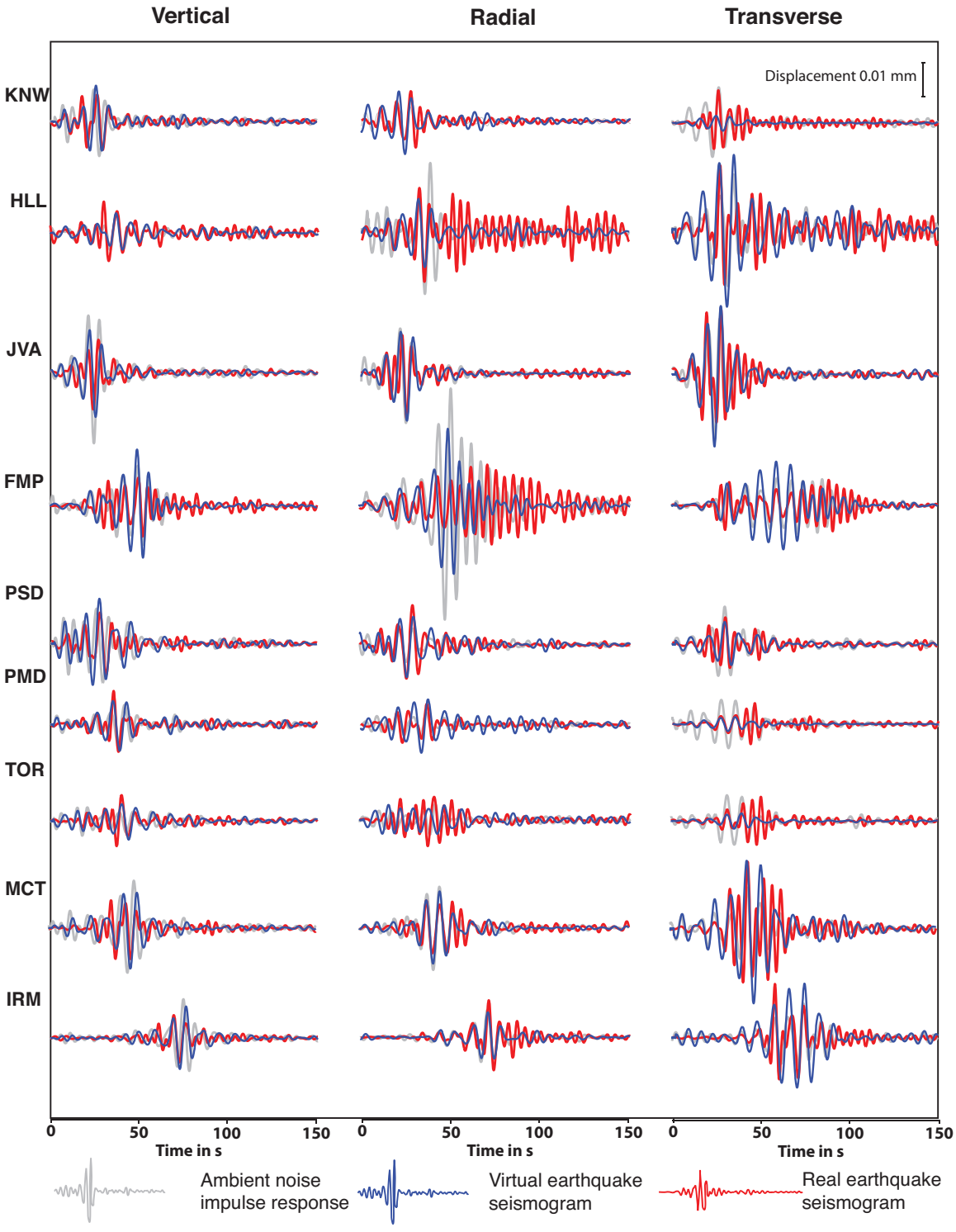

Figure 4.21: Same as Figure 4.11 for the 2011 M 4.5 San Bernardino earthquake.

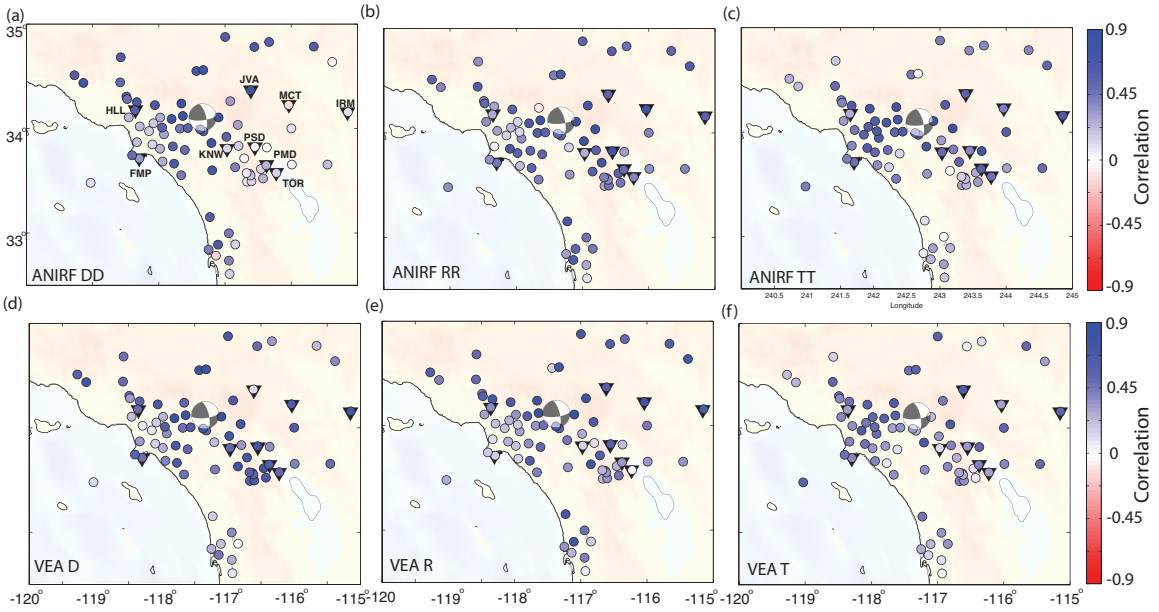

Figure 4.22: Same as Figure 4.12 for the 2011 M 4.5 San Bernardino earthquake.

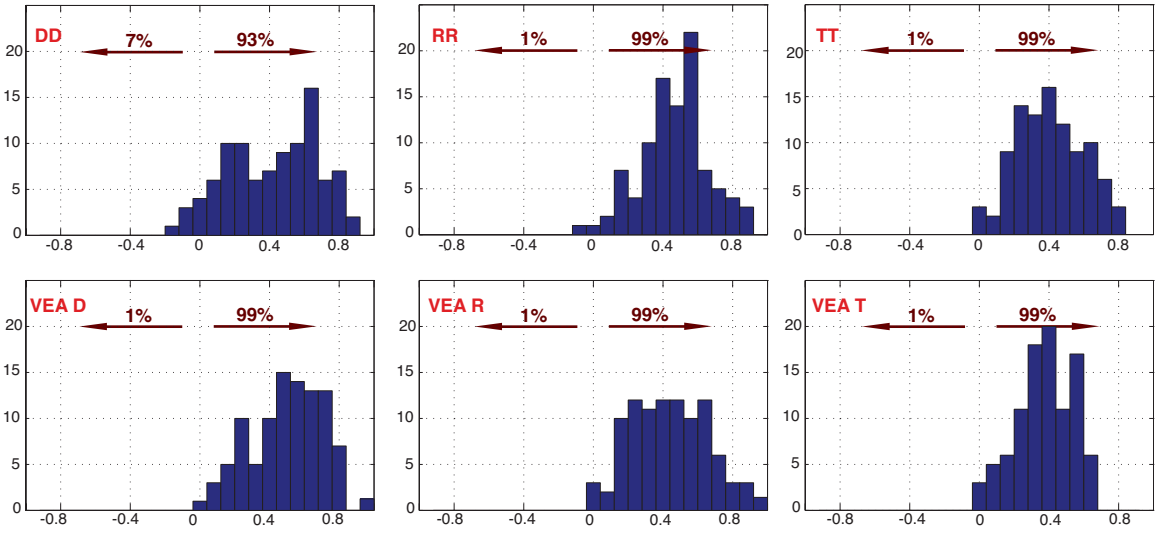

Figure 4.23: Same as Figure 4.13 for the 2011 M 4.5 San Bernardino earthquake.

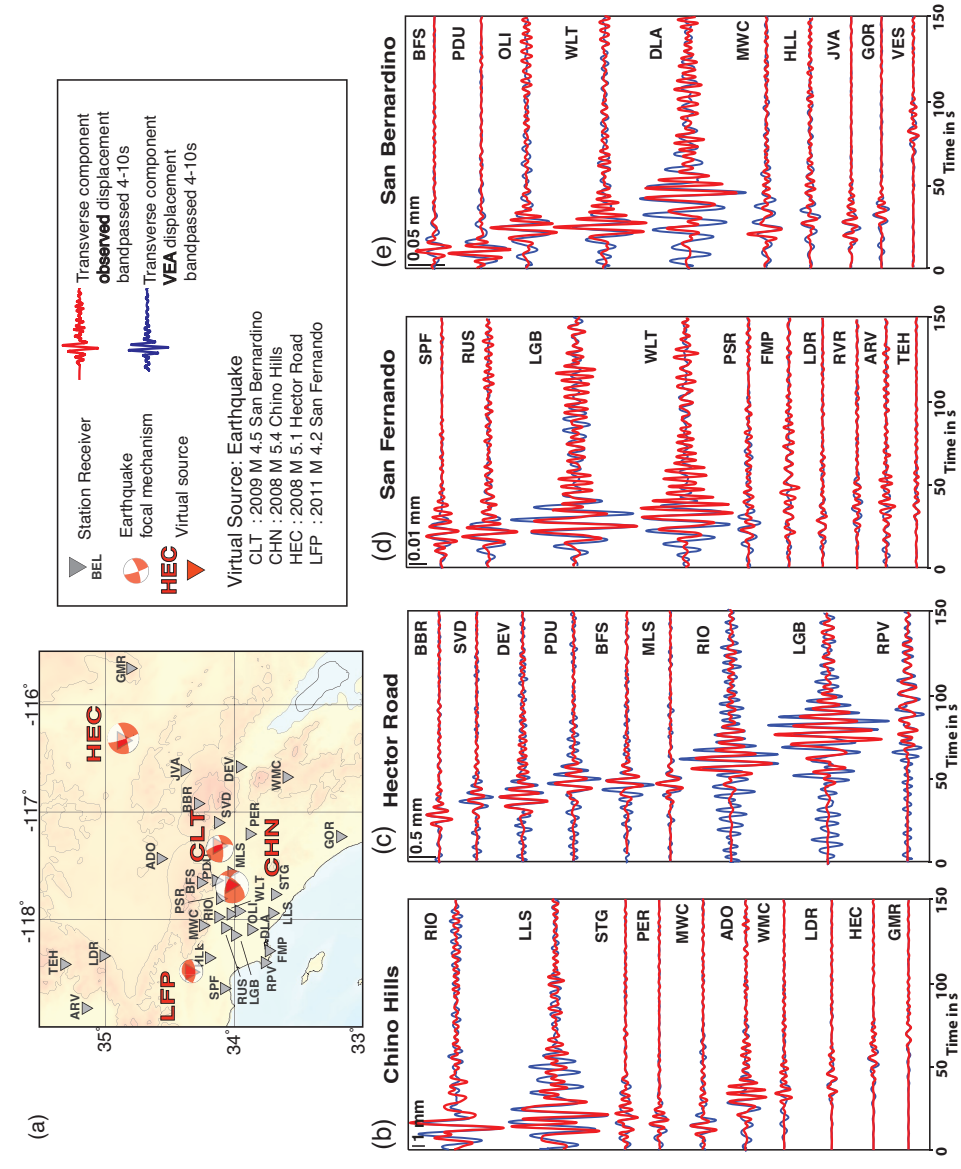

Figure 4.24: Same as Figure 4.7, but for depth and mechanism corrected response.

Conclusions

We have shown that the virtual earthquake approach can successfully predict ground motion for moderate magnitude earthquakes. We first extracted the surface-wave impulse response, or Green tensor, using the ambient seismic field for each station pair, then we corrected the impulse response for excitation depth, and the double-couple response for a single forces to the response due to a dislocation. These conversions require accurate estimation of the surface-wave excitation at the earthquake source for which we used a new surface-wave eigenproblem solver (GESC, *Denolle et al.* (2012)) that allowed us to calculate the displacement eigenfunctions and account for the locally complex vertical structure at the virtual source location.

We validate this technique by reproducing far-field terms of the seismograms for the period band of 4–10 s. Given the approximations and sources of uncertainty, we consider the validation successful, in that the constructed seismograms match real earthquake records, in both phase and amplitude. For the four moderate earthquakes in southern California with diverse focal mechanisms, the virtual earthquake approach provides reliable prediction of the ground motion over this period band.

Damaging earthquakes that are of most interest ($M > 6$) cannot be approximated as point sources at these periods. To predict ground motion for large seismic events, we need to consider the spatial variability of the Green's functions along extended ruptures. A deployment of seismometers along a fault of concern to record the ambient seismic field would provide the Green's functions needed to predict more complex displacement fields from scenario earthquakes.

Chapter 5

Large Virtual Earthquake on the San Andreas Fault

Introduction

Sedimentary basins are known to increase the damaging effects of earthquakes by amplifying and extending the duration of strong shaking (*Bard et al.*, 1988). To anticipate those effects, state-of-the-art computations of scenario earthquakes simulate seismic wave propagation through crustal structure that includes representations of sedimentary basins (*Olsen et al.*, 1995, 2006, 2009; *Graves et al.*, 2011; *Day et al.*, 2012). Our study is motivated by reports of strong basin amplification in Los Angeles for earthquakes on the southern San Andreas Fault that have emerged from such ground motion simulations (*Olsen et al.*, 2006; *Day et al.*, 2012), and the need to validate those simulations with data.

We present a virtual earthquake approach (VEA) that models long period strong ground motion using Green's functions derived from the ambient seismic field. The ambient seismic field (ASF) is excited by the coupling of the oceans and atmosphere with the solid Earth, and carries the signature of the structure between two stations. It is possible to extract the Earth's response to an impulsive force (i.e., the Green's function) through cross-correlation of the ASF (*Aki*, 1957; *Claerbout*, 1968; *Lobkis and Weaver*, 2001; *Weaver and Lobkis*, 2006; *Sánchez-Sesma and Campillo*, 2006). This capability has enabled travel-time measurements to image Earth's wave speed structure (*Campillo and Paul*, 2003; *Shapiro and Campillo*, 2004; *Shapiro et al.*, 2005; *Sabra et al.*, 2005a; *Nishida et al.*, 2008). The ambient field also contains amplitude information, including anelastic effects (*Prieto et al.*, 2009, 2011), that we exploit to predict earthquake shaking intensity.

In this study, we extend this method from point sources (*Denolle et al.*, 2013), appropriate for moderate (M $\sim$ 5) earthquakes, to finite ruptures of larger magnitude, using the representation theorem (*Burridge and Knopoff*, 1964). We apply this technique to predict ground motion in greater Los Angeles for scenario M $\sim$ 7 earthquakes on the San Andreas Fault.

We use data from a temporary deployment of broadband seismometers to determine Green's functions for virtual sources along a segment of the southern San Andreas Fault. We chose this location because previous simulations (*Day et al.*,

2012) indicate that waves generated by rupture of this segment would be strongly amplified in the Los Angeles Basin, far from the fault. We refer to our experiment as SAVELA (San Andreas Virtual Earthquake - Los Angeles). We correct the Green's functions for source location, depth, and mechanism, and scale amplitudes using a nearby earthquake of known magnitude. We then calculate seismograms using the VEA for a suite of M $\sim$ 7 scenario earthquakes along this fault, and compare the results with simulations of wave propagation through three-dimensional models of the Earth's crust (*Graves et al.*, 2011). Our results support previous findings of a pronounced waveguide effect and strong basin amplification (*Olsen et al.*, 2006; *Day et al.*, 2012). The spatial pattern of amplification found by these two techniques, however, differs substantially, as does the distribution of strong ground motion for different scenario earthquakes. The VEA provides a new method to develop and validate strong ground motion predictions.

The extended Virtual Earthquake Approach

We now introduce the extended virtual earthquake approach, which is a generalization of the point source VEA (*Denolle et al.*, 2013), to construct the ground motion for large earthquakes (Fig. 5.3). We first compute all components of the Green's tensor G_{ij} in frequency domain with the ASF velocity v_j recorded at a virtual source at surface location $\vec{\xi}' = (x_1', x_2')$ and the velocity v_i recorded at a receiver located at $\vec{\xi} = (x_1, x_2)$,

$$\widehat{G}_{ij}(\vec{\xi}, \vec{\xi}', \omega) = A \left\langle \frac{\hat{v}_i(\vec{\xi}, \omega)\hat{v}_j^*(\vec{\xi}', \omega)}{\{|\hat{v}_j(\vec{\xi}', \omega)|\}^2} \right\rangle, \tag{5.1}$$

where the operator $\langle \quad \rangle$ denotes stacking over time, and $\{ \quad \}$ denotes smoothing over the virtual source spectrum (in our case a 3 mHz running average) to stabilize the deconvolution. We recover the ASF Green's functions over the period range of 3-10 s, where the ASF has highest amplitudes from the ocean wave excitation.

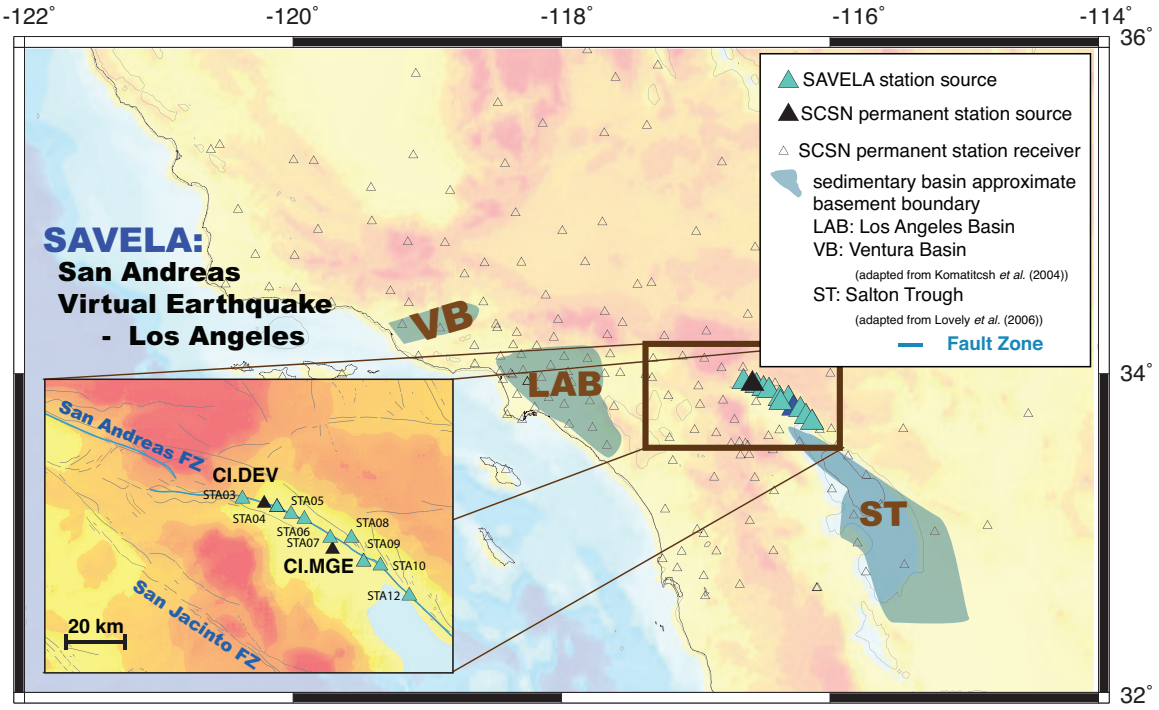

Figure 5.1: Temporary SAVELA and permanent Southern California Seismic Network (SCSN) stations. Shaded area shows the approximate shape of major sedimentary basins. Open triangles are SCSN seismic stations that we treat as receivers. Filled triangles are seismic stations with temporary deployments (blue) and permanent SCSN (black) stations located near the San Andreas Fault that we treat as virtual sources.

The source of the ambient seismic field is not uniformly distributed with azimuth (*Stehly et al.*, 2006) and different components of motion (S_H and P-S_V) are not equally excited. Both of these factors affect the recovered amplitude. We corrected our Green's functions to compensate for a first order azimuthal pattern as follows. For each source component (vertical, radial, and transverse), we find sinusoidal functions that best match the observed variation of amplitude with azimuth of the Green?s function amplitudes 5.2. For each component, we estimated the calibration factor required to for the ambient-field data to predict the absolute amplitudes for two local moderate events - the M5.4 Chino Hills, 2008 and M5.1 Hector Road, 2008 earthquakes.

We transform the Green tensor from North-East-down into radial-transverse-down coordinates, and determine the excitation using the radial and down components for Rayleigh waves and the transverse component for Love waves, thereby neglecting surface-wave refraction and multi pathing. Our data shows most clearly the surface-wave fundamental modes.

We correct each surface-to-surface Green's tensor using analytical expressions derived under the assumption that elastic properties vary solely with depth. We consider the Love-to-Rayleigh wave conversion and vice-versa to a second order, and this assumption allows us to extract Love waves on the TT component and the Rayleigh waves on RR, RD, DR, DD components. With this approximation, the Love- and Rayleigh-wave displacement spectra from a point moment tensor source $M(t)$ at horizontal position $\vec{\xi}'$ and depth $x_3' = h$ is in the far-field limit $\vec{\xi} = (x_1, x_2)$,

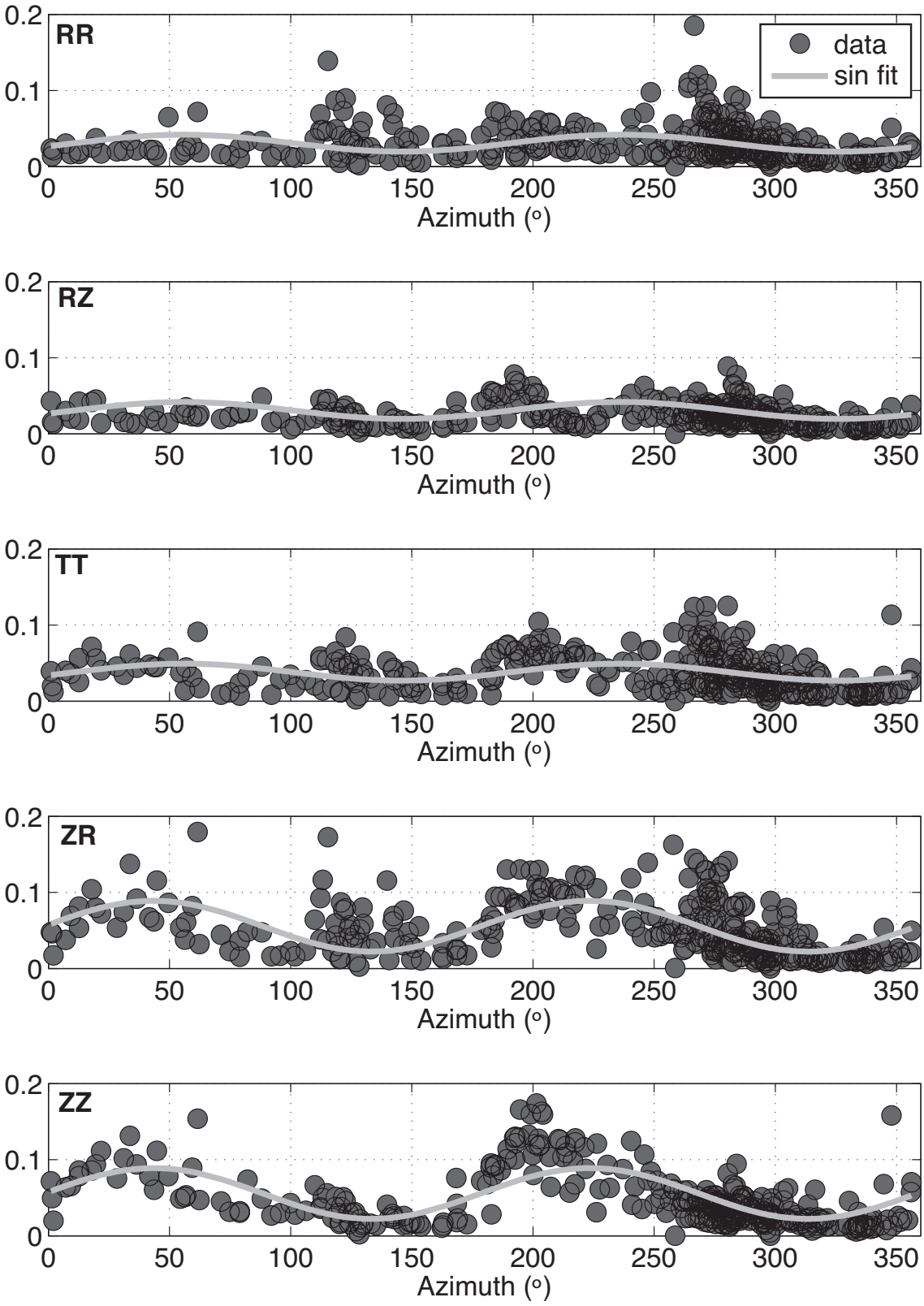

Figure 5.2: Effect of directionality of the ambient seismic field on surface-wave Green?s functions amplitudes. Peak amplitudes of the Green?s functions (one sided)

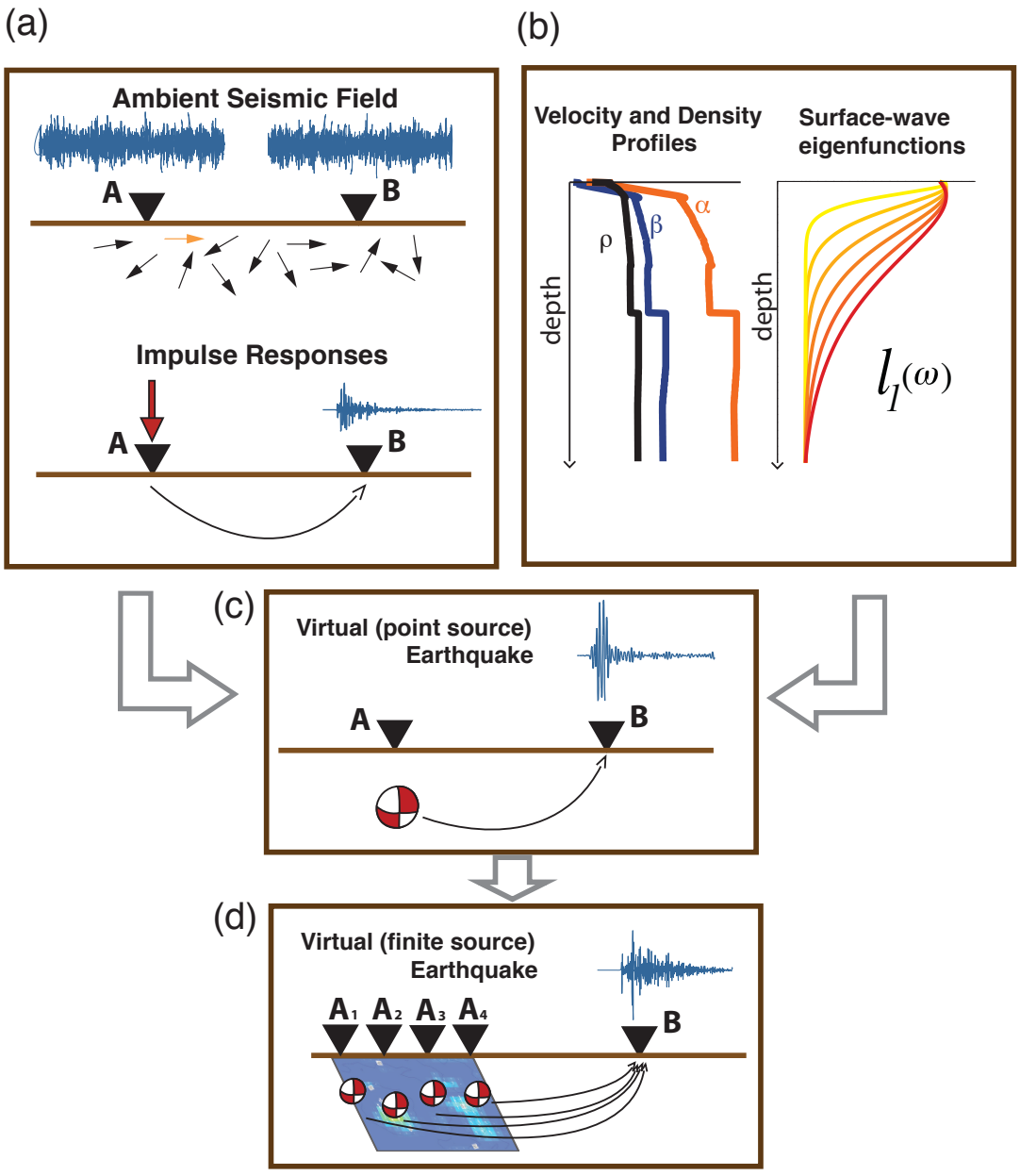

Figure 5.3: Flowchart of the extended virtual earthquake approach. (a) Compute the ASF Green's function, (b) estimate the surface-wave excitation, (d) correct for the point source virtual earthquake, and (e) sum the point sources to simulate finite rupture effects.

$$\widehat{U}_T(\vec{\xi},\omega) = \frac{1}{l_1(\vec{\xi}',0\omega)}\left[-ik_L(\vec{\xi}',\omega)\widehat{M}_{TR}(\omega)l_1(\vec{\xi}',h,\omega)+\widehat{M}_{TD}(\omega)l_1'(\vec{\xi}',h,\omega)\right]\widehat{G}_{TT}(\vec{\xi},\vec{\xi}',\omega) \quad (5.2)$$

$$\widehat{U}_R(\vec{\xi},\omega) = \frac{1}{r_1(\vec{\xi}',0,\omega)}\left[-ik_R(\vec{\xi}',\omega)\widehat{M}_{RR}r_1(\vec{\xi}',h,\omega)+\widehat{M}_{RD}(\omega)r_1'(\vec{\xi}',h,\omega)\right]\widehat{G}_{RR}(\vec{\xi},\vec{\xi}',\omega)$$
$$+\frac{1}{r_2(\vec{\xi}',0,\omega)}\left[-ik_R(\vec{\xi}',\omega)\widehat{M}_{DR}(\omega)r_2(\vec{\xi}',h,\omega)+\widehat{M}_{DD}(\omega)r_2'(\vec{\xi}',h,\omega)\right]\widehat{G}_{DR}(\vec{\xi},\vec{\xi}',\omega) \quad (5.3)$$

$$\widehat{U}_D(\vec{\xi},\omega) = \frac{1}{r_1(\vec{\xi}',0,\omega)}\left[-ik_R(\vec{\xi}',\omega)\widehat{M}_{RR}(\omega)r_1(\vec{\xi}',h,\omega)+\widehat{M}_{RD}(\omega)r_1'(\vec{\xi}',h,\omega)\right]\widehat{G}_{DR}(\vec{\xi},\vec{\xi}',\omega)$$
$$+\frac{1}{r_2(\vec{\xi}',0,\omega)}\left[-ik_R(\vec{\xi}',\omega)\widehat{M}_{DR}(\omega)r_2(\vec{\xi}',h,\omega)+\widehat{M}_{DD}(\omega)r_2'(\vec{\xi}',h,\omega)\right]\widehat{G}_{DD}(\vec{\xi},\vec{\xi}',\omega) \quad (5.4)$$

where $r_1(\vec{\xi}',\omega)$, $r_2(\vec{\xi}',\omega)$, $l_1(\vec{\xi}',\omega)$ are the displacement eigenfunctions, $k_R(\vec{\xi}',\omega)$ and $k_L(\vec{\xi}',\omega)$ are the wave numbers of Rayleigh and Love waves at the source. The dependence of the wavenumber and eigenfunction on horizontal location enters solely through the selection of the depth-dependent structure at $\vec{\xi}'$.

We obtain the surface-wave eigenfunctions (Fig. 5.3b) using the elastic wave speed and density profiles extracted from the Southern California Earthquake Center Community Velocity Model-S4 (*Magistrale et al.*, 2000; *Kohler et al.*, 2003), and solve the surface-wave eigenproblem using the Generalized Eigenproblem Spectral Collocation method (*Denolle et al.*, 2012).

Using the Representation Theorem

We reconstruct the seismograms from the large earthquake using the representation theorem (*Burridge and Knopoff*, 1964). The representation theorem relates the i^{th} component of the displacement recorded at the surface in horizontal location $\vec{\xi}$ for a source located along the depth x_3' and the horizontal location $\vec{\xi}'$:

$$u_i(\vec{\xi},0,t) = \iint_\Sigma m_{ij}(\vec{\xi}',x_3',t) * \frac{\partial}{\partial x_j'}G_{ij}(\vec{\xi},x_3',t,\vec{\xi}',0,t_0)d\Sigma \quad , \quad (5.5)$$

For a point source located in horizontal location $\vec{\xi'}$ and depth h moment tensor is:

$$m_{ij}(\vec{\xi'},t) = \mu(\vec{\xi'})\left[\Delta s_i(\vec{\xi'},h)n_j(\vec{\xi'},h) + \Delta s_j(\vec{\xi'},h)n_i(\vec{\xi'},h)\right] f(t) \tag{5.6}$$

where $f(t)$, of spectrum $\hat{F}(\omega)$ is the source time function and $\mu(\vec{\xi'},h)$ is the shear modulus at the source, and $\Delta\vec{s}$ the displacement on the fault. To represent a source slip history that realistically describes earthquake ruptures, we discretize the fault interface into sub-faults that we approximate as point sources. We can, however, obtain analytical expressions of the far-field displacement from simple source representations such as Haskell models and we detail the derivation hereafter.

Haskell Source Model

We assume a purely vertical strike slip rupture with constant slip Δs, constant rupture velocity v_r, and a receiver located in the far field, illustrated in Figure 5.4. We write

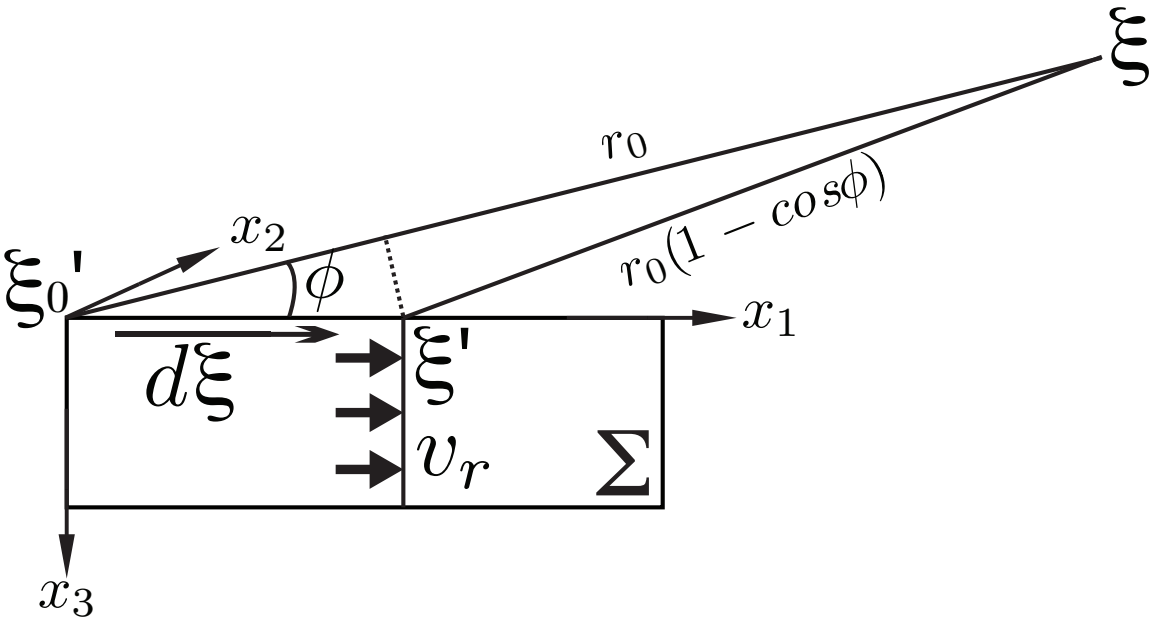

Figure 5.4: Haskell Rupture model for each segment and far-field approximation conventions.

the moment density function:

$$\begin{aligned} m(\vec{\xi'},t) &= \mu(\vec{\xi'})\Delta s\dot{f}(\vec{\xi'},t) * \delta(t - d\xi/v_r) \\ &= \overline{M}(\vec{\xi'})\dot{f}(\vec{\xi'},t) * \delta(t - d\xi/v_r) \end{aligned} \tag{5.7}$$

Because the source moves from $\vec{\xi_0'}$ to $\vec{\xi'}$, we shift the Green's function of $|\vec{\xi'} - \vec{\xi_0'}|/c(\omega)$, where $c(\omega)$ is the phase velocity. In the far field approximation (Fig. 5.4), $|\vec{\xi'} - \vec{\xi_0'}| \sim r_0 - d\xi\cos(\phi)$. The total shift becomes:

$$\begin{aligned} \frac{|\vec{\xi'} - \vec{\xi_0'}|}{c(\omega)} + d\xi/v_r &= (r_0 - d\xi\cos(\phi))/c(\omega) + d\xi/v_r \\ &= r_0/c(\omega) + d\xi/v_r(1 - v_r/c(\omega)\cos(\phi))m \end{aligned}$$

that we implement into equation 5.5:

$$\begin{aligned} \widehat{U}_T(\vec{\xi},\omega) &= i\omega\hat{F}(\omega)\iint_\Sigma \frac{\mu(\vec{\xi'})\Delta s(\vec{\xi'})}{l_1(\vec{\xi'},0,\omega)}\Bigg[- ik_L(\vec{\xi'},\omega)\overline{M}_{TR}l_1(\vec{\xi'},h,\omega) + \\ &\quad \overline{M}_{TD}l_1'(\vec{\xi'},h,\omega)\Bigg]\hat{G}_{TT}(\vec{\xi},0,\vec{\xi'},h,\omega)e^{i\omega(r_0/c(\omega) + d\xi/v_r(1 - v_r/c(\omega)\cos(\phi)))}d\Sigma \\ &= i\omega\hat{F}(\omega)e^{i\omega r_0/c(\omega)}\iint_\Sigma \frac{\mu(\vec{\xi'})\Delta s(\vec{\xi'})}{l_1(\vec{\xi'},0,\omega)}\Bigg[- ik_L(\vec{\xi'},\omega)\overline{M}_{TR}l_1(\vec{\xi'},h,\omega) + \\ &\quad \overline{M}_{TD}l_1'(\vec{\xi'},\omega)\Bigg]\hat{G}_{TT}(\vec{\xi},0,\vec{\xi'},h,\omega)e^{i\omega d\xi/v_r(1 - v_r/c(\omega)\cos(\phi))}d\Sigma \end{aligned} \tag{5.8}$$

Assuming the fault segment length L, we write the directivity factor $X = \frac{\omega L}{2v_r}(1 - v_r/c(\omega)\cos(\phi))$ such that:

$$\begin{aligned} \widehat{U}_T(\vec{\xi},\omega) &= i\omega\hat{F}(\omega)e^{i\omega r_0/c}\iint_\Sigma \frac{\mu(\vec{\xi'})\Delta s(\vec{\xi'})}{l_1(\vec{\xi'},0,\omega)}\Bigg[- ik_L(\vec{\xi'},\omega)\overline{M}_{TR}l_1(\vec{\xi'},h,\omega) + \\ &\quad \overline{M}_{TD}l_1'(\vec{\xi'},h,\omega)\Bigg]\hat{G}_{TT}(\vec{\xi'},0,\vec{\xi'},h,\omega)e^{iXd\xi/2L}d\Sigma \end{aligned} \tag{5.9}$$

Let's assume a segment of dimensions L along strike and H for the locking depth,

and a depth-dependent slip on a segment, $\Delta s(\mathbf{x}') = \Delta s(x_3')$, with a 1D medium. We reorganize and simplify equation 5.9 into:

$$\begin{aligned}
\widehat{U}_T(\vec{\xi},\omega) &= i\omega\hat{F}(\omega)e^{i\omega r_0/c(\omega)}\int_0^H\int_0^L \frac{\mu(x_3')\Delta s(x_3')}{l_1(0,\omega)}\Bigg[-ik_L(\omega)\overline{M}_{TR}l_1(x_3',\omega)+ \\
&\quad \overline{M}_{TD}l_1'(x_3',\omega)\Bigg]\hat{G}_{TT}(\vec{\xi},\vec{\xi}',\omega)e^{2iXd\xi/L}dx_1'dx_3' \\
&= \frac{i\omega\hat{F}(\omega)e^{i\omega r_0/c}}{l_1(0,\omega)}\left[\int_0^L e^{2iXd\xi/L}dx_1'\right]\left[\int_0^H \mu(x_3')\Delta s(x_3')\Bigg[-ik_L(\omega)\overline{M}_{TR}l_1(x_3',\omega)+\right. \\
&\quad \left.\overline{M}_{TD}l_1'(x_3',\omega)\Bigg]dx_3'\right]\hat{G}_{TT}(\vec{\xi},\vec{\xi}',\omega) \\
&= \frac{i\omega\hat{F}(\omega)e^{i\omega r_0/c(\omega)}}{l_1(0,\omega)}\left[\frac{e^{2iXd\xi/L}}{2iXd\xi/L}\right]_0^L\left[\int_0^H \mu(x_3')\Delta s(x_3')\Bigg[-ik_L(\omega)\overline{M}_{TR}l_1(x_3',\omega)+\right. \\
&\quad \left.\overline{M}_{TD}l_1'(x_3')\Bigg]dx_3'\right]\hat{G}_{TT}(\vec{\xi},\vec{\xi}',\omega) \\
&= \frac{i\omega\hat{F}(\omega)e^{i\omega r_0/c(\omega)}}{l_1(0,\omega)}\left[\frac{e^{2iX}}{2iX}-\frac{1}{2iX}\right]\left[\int_0^H \mu(x_3')\Delta s(x_3')\Bigg[-ik_L(\omega)\overline{M}_{TR}l_1(x_3',\omega)+\right. \\
&\quad \left.\overline{M}_{TD}l_1'(x_3',\omega)\Bigg]dx_3'\right]\hat{G}_{TT}(\vec{\xi},\vec{\xi}',\omega) \\
&= \frac{e^{iX}i\omega\hat{F}(\omega)e^{i\omega r_0/c(\omega)}}{l_1(0,\omega)}\frac{e^{iX}-e^{-iX}}{2iX}\left[\int_0^H \mu(x_3')\Delta s(x_3')\Bigg[-ik_L(\omega)\overline{M}_{TR}l_1(x_3',\omega)+\right. \\
&\quad \left.\overline{M}_{TD}l_1'(x_3',\omega)\Bigg]dx_3'\right]\hat{G}_{TT}(\vec{\xi},\vec{\xi}',\omega) \\
&= \frac{i\omega\hat{F}(\omega)e^{iX}\mathrm{sinc}(X)e^{i\omega r_0/c(\omega)}}{l_1(0,\omega)}\left[\int_0^H \mu(x_3')\Delta s(x_3')\Bigg[-ik_L(\omega)\overline{M}_{TR}l_1(x_3',\omega)+\right. \\
&\quad \left.\overline{M}_{TD}l_1'(x_3',\omega)\Bigg]dx_3'\right]\hat{G}_{TT}(\vec{\xi},\vec{\xi}',\omega) \qquad (5.10)
\end{aligned}$$

Similar results may be derived for Rayleigh waves. Despite the simplicity of Haskell models, they show the first order directivity effects that we see in channeling of the

seismic energy for propagating ruptures with strong coherent energy.

Realistic Source

We use a realistic source representation developed by the CyberShake project (*Graves et al.*, 2011) that we discuss in further detail below. The fault surface is divided into sub faults, which we approximate as point sources.

To build intuition on the effect of finite source effect, and to verify the extended virtual earthquake correction, we verify our method for a simple scenario earthquake. We place receivers 150 km away from the station source STA06, assume the Green's functions to be Gaussian pulses shifted with a wave speed of 3 km/s at all components and at all frequencies, to better visualize phase shifts and effect of directivity. We show in Figure 5.5, the location of the test-source and we take STA06 as the station source. We shift the Green's function to each point source epicenter using the phase velocities found by solving the eigenproblem under the STA06 velocity model.

CyberShake Scenario Earthquakes

The CyberShake project (*Graves et al.*, 2011) uses physics-based prediction of strong ground motion developed by combining pseudo-dynamic fault rupture models (*Guatteri et al.*, 2004) with three-dimensional numerical wave propagation simulations. CyberShake simulations solve the wave equation in complex three-dimensional crustal velocity models to obtain the Green's functions. In contrast, the VEA directly computes the Green's functions through cross-correlation of the ambient seismic field. We consider an ensemble of 96 simulated ruptures of magnitude 7.15, a small subset of the Cybershake models, chosen to coincide with rupture of the San Andreas Fault near our virtual earthquake array. We use these source models to compare two independent methods for long period ground motion prediction: the Cybershake simulations and our virtual earthquake approach.

We first discretize the fault into sub-faults. Next, we compute the VEA waveforms by treating each as a point source, and by summing their contributions (Fig. 5.3) according to their rupture time and slip amplitude. Because the SAVELA seismic

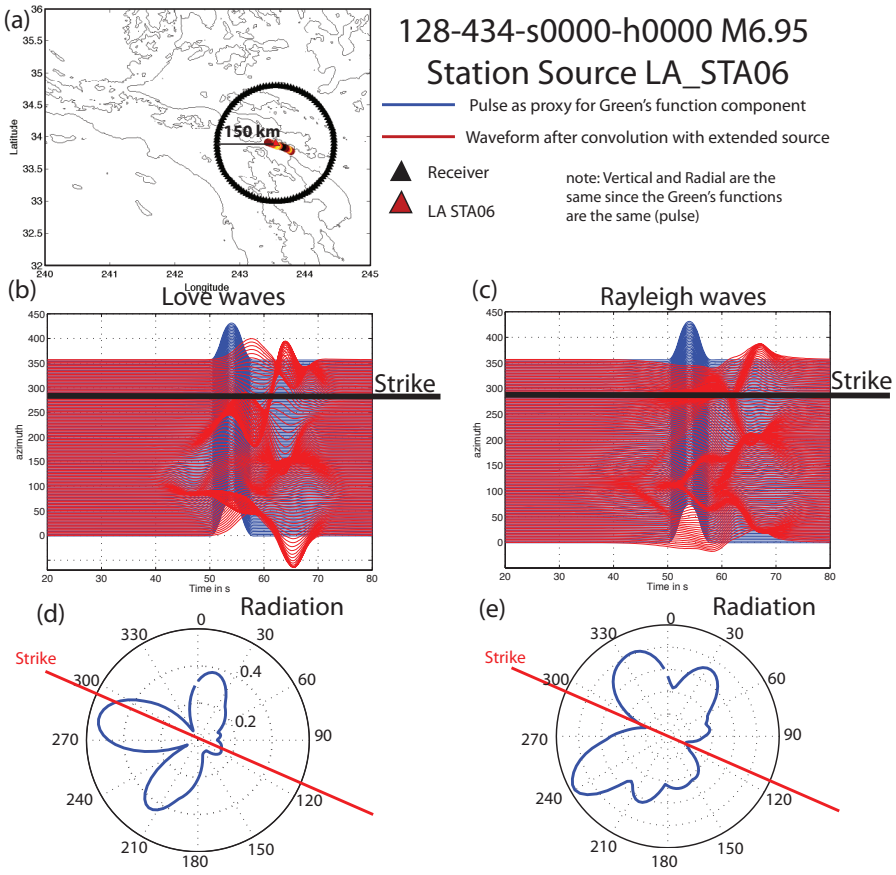

Figure 5.5: Ratio of the PGV averaged over all northwestward and southeastward propagating rupture assuming the medium is laterally homogenous with velocity profile under DEV station used as reference. We construct the surface-to-surface Green tensor using equations 7.146 and 7.147 (*Aki and Richards*, 2002) from each station source to all receivers and implement the VEA correction to estimate the ratio of peak amplitudes for the $\perp$ (a), $||$ (b), and vertical (c) components.

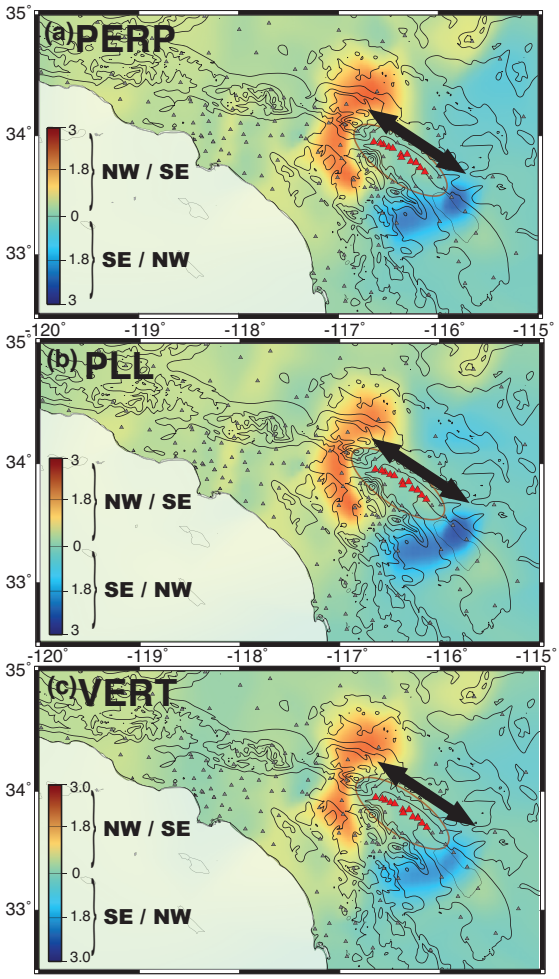

Figure 5.6: Ratio of the PGV averaged over all northwestward and southeastward propagating rupture assuming the medium is laterally homogenous with velocity profile under DEV station used as reference. We construct the surface-to-surface Green tensor using equations 7.146 and 7.147 (*Aki and Richards*, 2002) from each station source to all receivers and implement the VEA correction to estimate the ratio of peak amplitudes for the $\perp$ (a), || (b), and vertical (c) components. Compared to the 3D case (Fig. 5.8), we see lesser contrast between both scenario earthquakes and the dipole-like pattern formed by the directivity of the rupture propagation around the fault zone.

stations are approximately 5 km apart (Fig. 5.1), we interpolate the Green's functions in between the seismic station and virtual source by introducing phase shift using the phase velocity estimated through solving the surface-wave eigenproblem (*Denolle et al.*, 2012, 2013). Finally, because we use the far-field approximation, we focus on the ground motion recorded at least 30 km from the fault.

Results

Previous simulations (*Olsen et al.*, 2006) of strong ground motion for a large earthquake on the Southern San Andreas fault revealed that seismic waves would be funneled from the fault, through a sedimentary waveguide, and into the Los Angeles Basin. This would shake downtown Los Angeles much more intensely than previously expected. The degree of amplification in those simulations depends on the rupture characteristics of the earthquake (*Day et al.*, 2012); however, whether this effect would occur in a real earthquake also depends on the detailed structure of the waveguide. No earthquake large enough to excite long period seismic waves has yet occurred along the critical section of the San Andreas Fault to test the simulations; however, we can use the VEA to ascertain if this effect occurs in the real Earth.

Our VEA ground motion predictions (Fig. 5.7) show strong amplification and the channeling of seismic waves into the Los Angeles basin. For identical slip distributions, but southward vs. northward propagation, we find a factor of 2 difference in peak ground velocity (PGV) due to directivity. We also find much greater shaking in the basin than in surrounding areas at equivalent distances from the source for both scenarios.

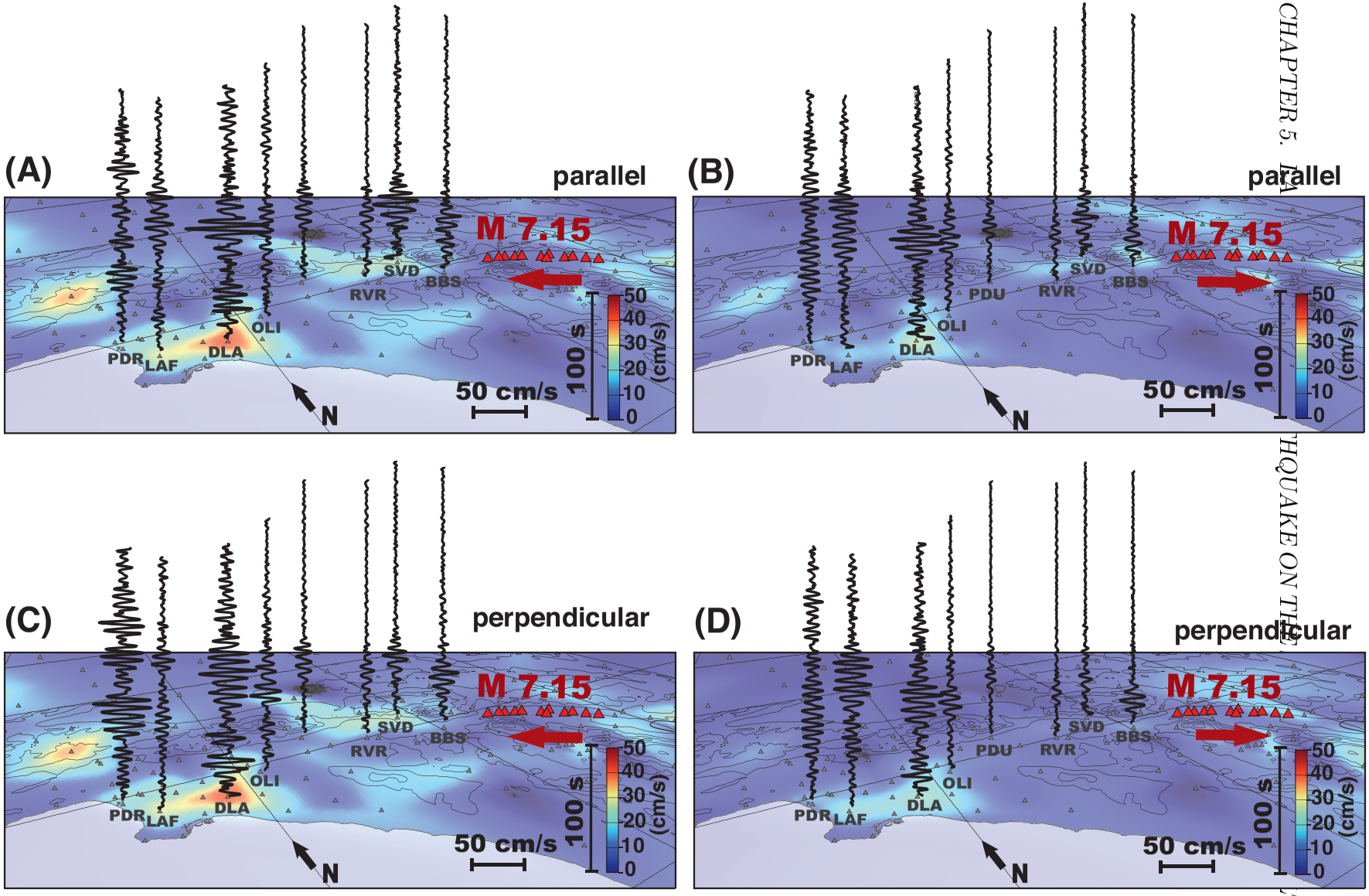

Figure 5.7: Velocity seismograms (white waveforms) and PGV (color scale) for two M 7.15 scenario earthquake ruptures determined using the virtual earthquake approach. Simulations are divided into northwestward propagating ruptures (left) and southeastward propagating ruptures (right) for the horizontal fault-parallel and fault-perpendicular components of motion.

We consider separately the VEA results for scenario slip distributions for hypocenters located at either end of the fault segment. Figure 5.8 shows peak ground velocity (PGV) for the fault-parallel, fault-perpendicular, and vertical components of velocities averaged separately over scenarios involving propagation to the northwest and southeast. Amplification in sedimentary basins is apparent, regardless of rupture propagation direction. The PGV experienced in downtown Los Angeles, averaged over all scenarios, is as high as 50 cm/s for the vertical and 36 cm/s for the horizontal components. This differs substantially from the horizontal-to-vertical strong ground motion amplitudes at higher frequencies and closer distances where horizontal amplitudes are typically larger (*Campbell and Bozorgnia*, 2003). The directivity-basin coupling (*Day et al.*, 2012) appears in the enhanced amplification in Ventura Basin (VB) and Los Angeles Basin (LAB) that noticeably correlates with the 3-D structure. In a laterally homogeneous medium, we expect a systematic variation with direction that approximates a dipole (Fig. 5.6). Instead, we see strong variations of amplitude ratios (Fig. 5.8) for all three components of motion. The strength of the directivity-structure coupling is extensive, and spatially variable within the Los Angeles Basin. Northern LA and the San Gabriel foothills experience strong coupling on the fault-perpendicular component, whereas the coupling for the fault-parallel component is stronger in South Los Angeles, Palos Verdes, and Chino Hills. Coupling for the vertical component is stronger in the areas where the basin is deepest, and overall stronger than in the laterally homogeneous case.

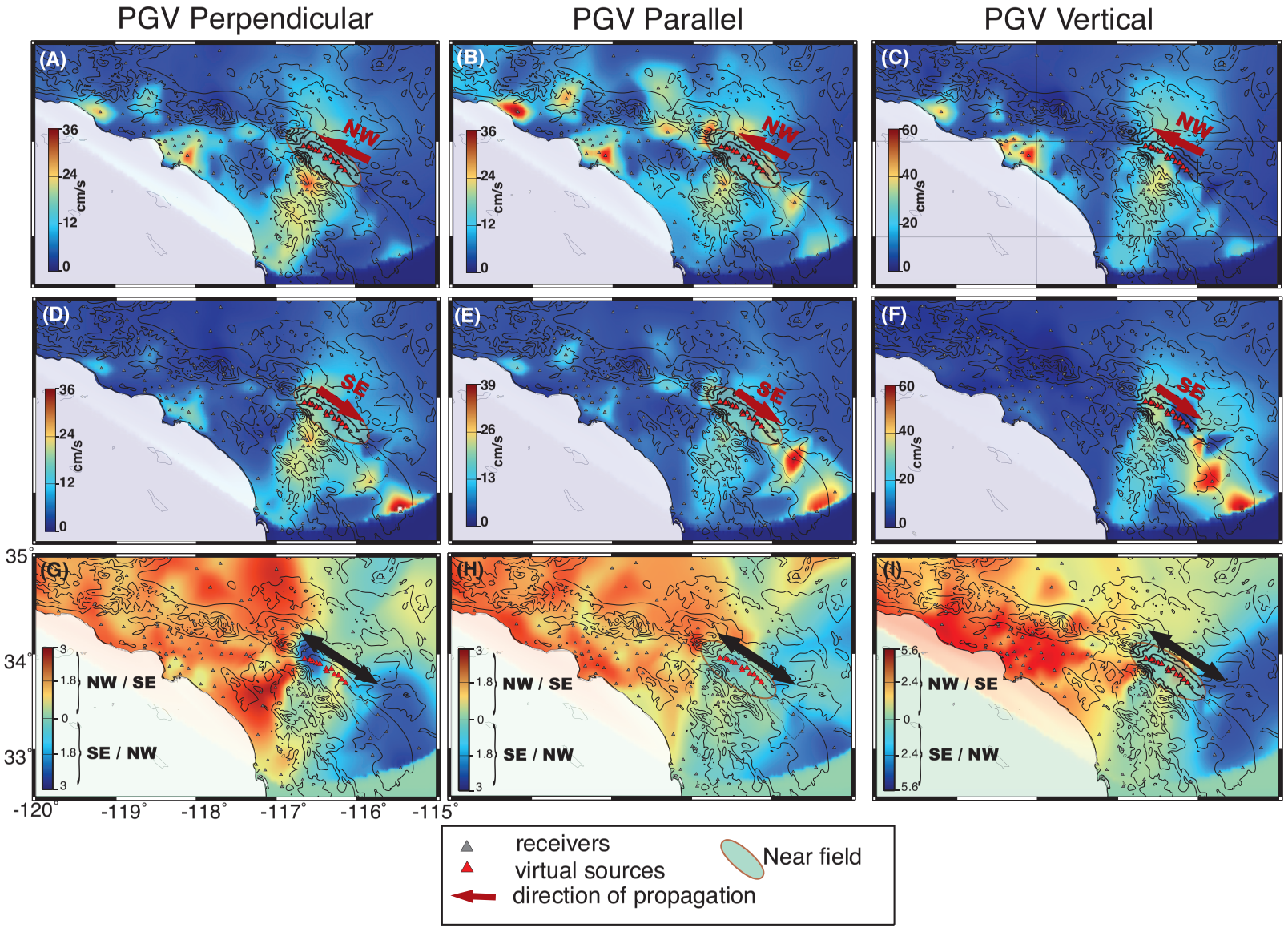

Figure 5.8: PGV averaged over all northwestward (top panels) and southeastward (mid-panels) propagating ruptures for perpendicular ((A) and (D)), parallel ((B) and (E)), and vertical ((V) and (f)) components. (E) Ratio of mean PGV for NW scenario to SE scenario of the fault-perpendicular (g), fault parallel (F), and vertical (I). Compared to the 1D case (Fig. 5.6), we see lesser contrast between both scenario earthquakes and the dipole-like

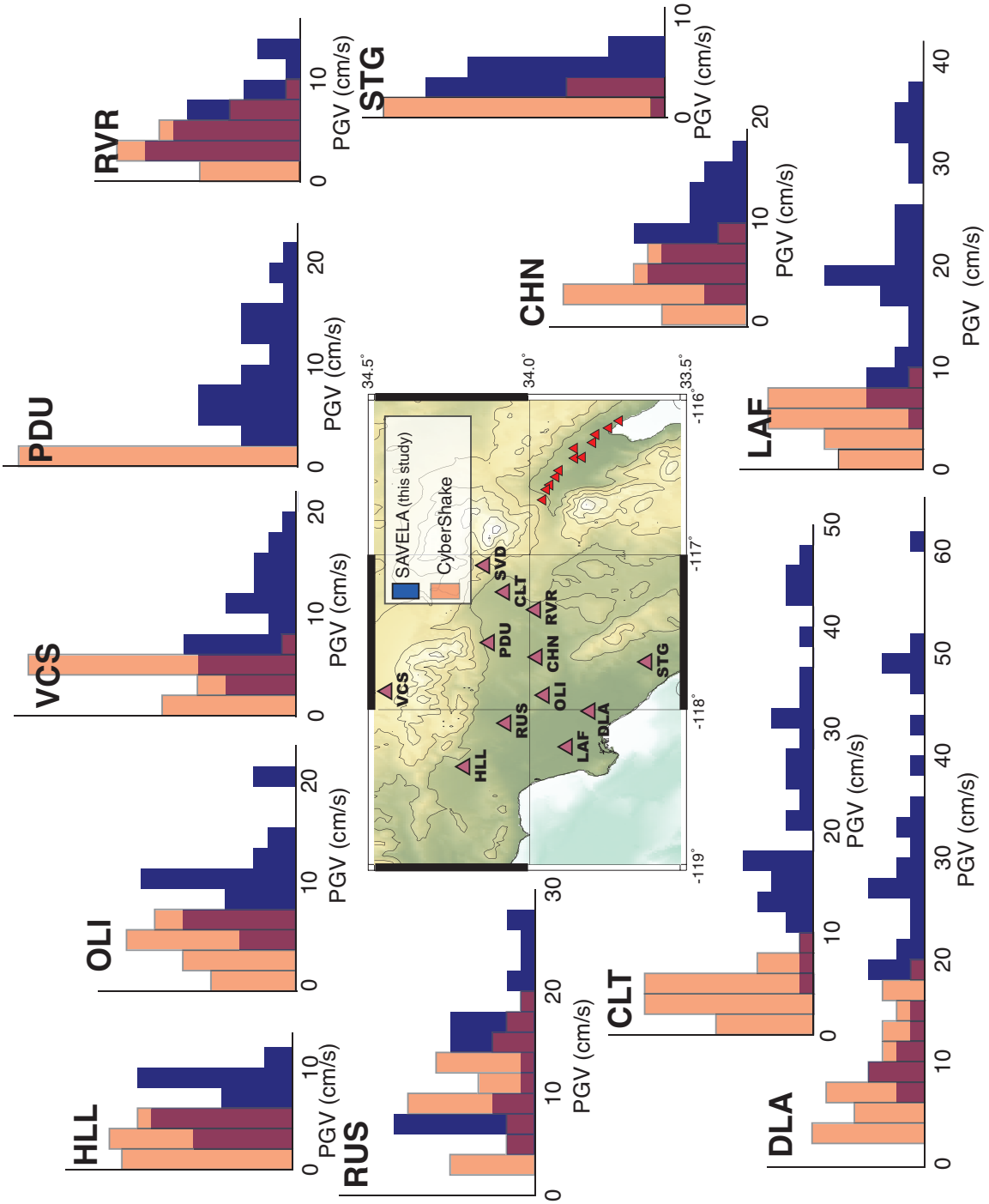

Figure 5.9: Histograms of PGV (in cm/s) for the fault-parallel component from both SAVELA (blue) and CyberShake (orange) for 36 scenario earthquakes.

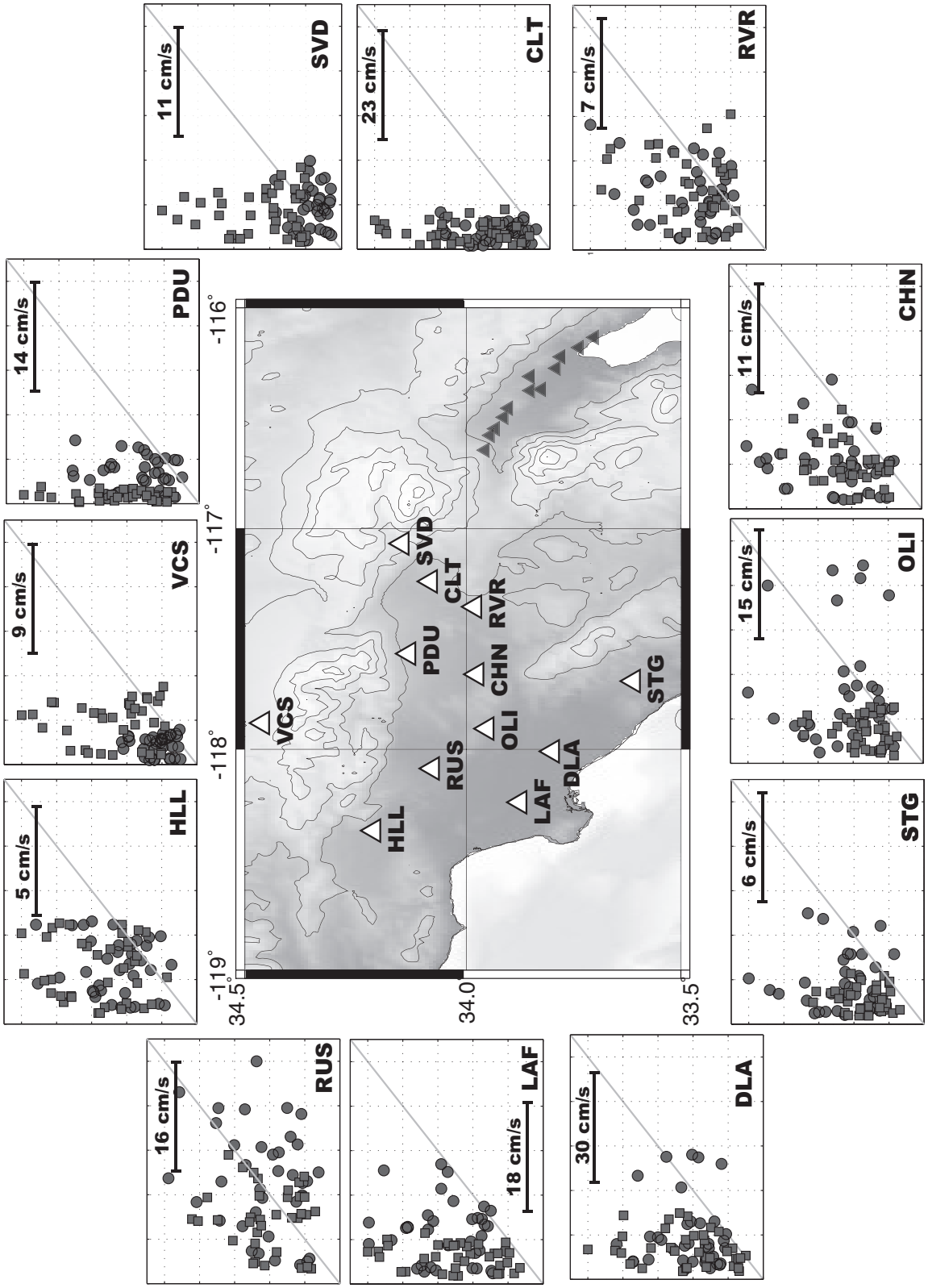

Figure 5.10: Scatter plots of the predicted PGV from CyberShake (x-axis) and SAVELA (y-axis) normalized at each site for a maximal prediction for 32 scenario earthquakes. Green line is perfect fit, fault-parallel component (squares), fault-perpendicular component (dots)

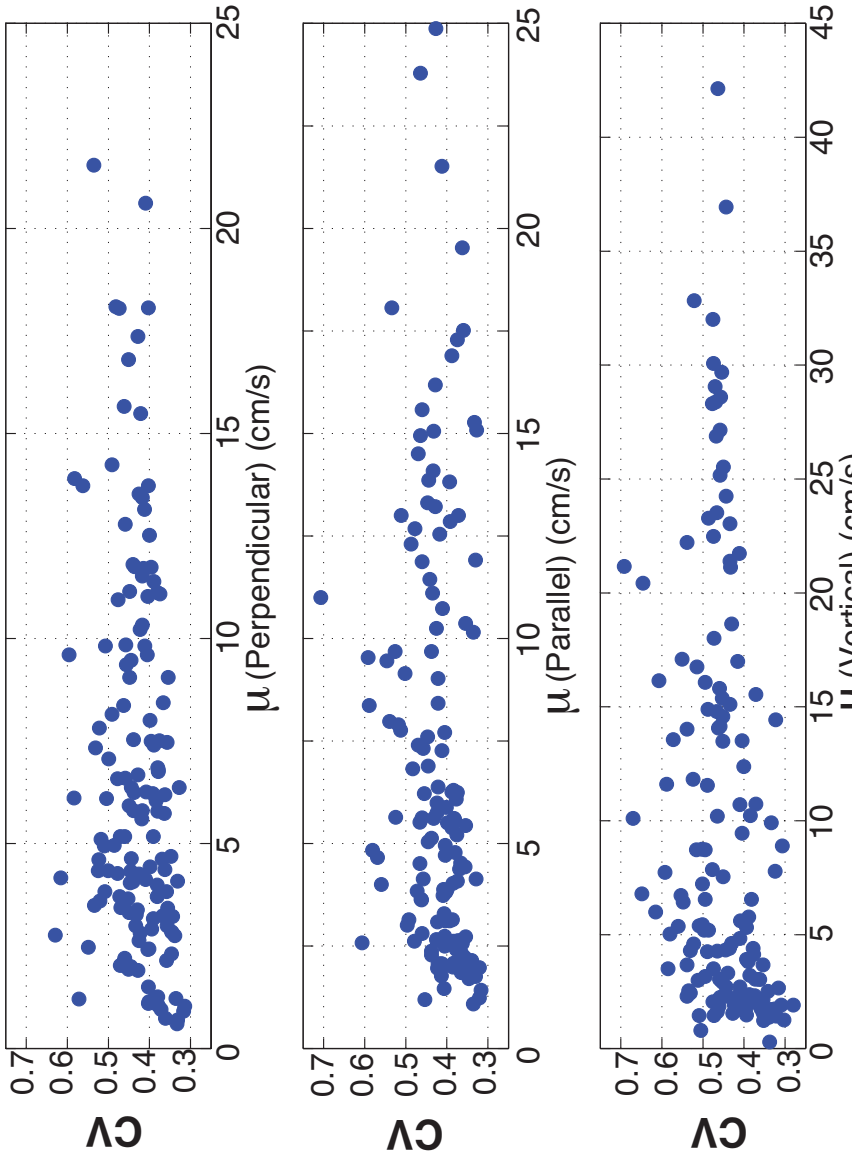

Figure 5.11: Coefficient of variation $CV = \sigma/\mu$ where μ is the mean PGV and σ the standard deviation at each station, for the perpendicular (top), parallel (medium) and vertical (bottom) components. The uncertainties grow with the ground motion.

We compare VEA low frequency (up to 0.33 Hz) seismograms with Cybershake simulations for 36 scenario earthquakes at the subset of sites for which CyberShake results are available (*Graves et al.*, 2011). We find approximate agreement between PGV levels found independently by the two methods; however, there are substantial differences in the distributions of those ground motions (Fig. 5.9, Fig. 5.10). For both methods the variation of PGV is narrow for stations on bedrock (VCS, PDU, and SVD) and broad for stations in the basin (DLA, LAF and RUS). This suggests that not only is ground motion amplified by sedimentary basins, but that ground motion variability scales with it. The variability in PGV increases with the overall ground motion such that the coefficient of variation stays constant (Fig. 5.11). Ground motion variability also tends to be greater for the virtual earthquake results than for the CyberShake simulations. Although we believe these differences are real, there could be contributions from uncertainties in the VEA results due to: low *signal-to-noise ratio* of the Green's functions, the 1D approximation for source excitation, and linear effects due to shallow structure that affects the VEA, but may not be represented in the velocity model used for the CyberShake simulations.

We calibrated the amplitudes of the Green?s functions such that the peak amplitudes predicted by our approach would match those of moderate-sized earthquakes. Nonlinear effects in surficial materials are important in strong ground motion. Some ground motion simulations have incorporated non-linear soil effects (29), and found a large decrease in the predicted strong ground motion. This could be an important effect because unconsolidated sediments are likely to be found in sedimentary basins, and would be expected to behave nonlinearly during strong shaking. Our approach, as well as the CyberShake simulations, is based on an assumption of linearity, and does not incorporate nonlinear effects. To the extent that they are important, our predicted ground motion amplitudes are likely to over-estimate true amplitudes in future large earthquakes.

Conclusions

In summary, we present a new approach to predict strong ground motion and to validate simulations of large scenario earthquakes using the ambient seismic field. We use a temporary array of seismic stations along the southern San Andreas Fault and apply the virtual earthquake approach to predict ground motion in the Los Angeles area for M 7.15 scenario earthquakes. We predict large amplitudes in a period range of 3 –10 s in sedimentary basins, consistent with CyberShake simulation predictions. Our results confirm the presence and influence of a waveguide to the west of San Gorgonio pass that channels seismic waves from San Andreas events into the Los Angeles Basin. This amplification is significant for all tested scenarios. We also confirm that directivity couples with shallow crustal structure to increase the effect of amplification (*Day et al.*, 2012). We find greater variability of ground motion within the basins than on bedrock. We also find a wider range of predicted peak amplitudes than is found in simulations, which would increase uncertainty in ground motion predictions, and thereby impact seismic hazard assessments. We consider the SAVELA experiment to be a proof-of-concept experiment to demonstrate the viability of using the ambient seismic field to predict strong ground motion from large earthquakes. Our results support more ambitious, targeted experiments to improve the accuracy of long-period strong ground motion prediction for future earthquakes in earthquake-threatened cities .

Chapter 6

Towards Improved Green's Functions

Introduction

The cross-correlation of the diffuse field recorded at two receivers yields the impulse response function between two receivers (*Aki*, 1957; *Claerbout*, 1968; *Lobkis and Weaver*, 2001; *Weaver and Lobkis*, 2006), but only under appropriate conditions. The key assumption to guarantee that the cross-correlations correspond to the impulse response is that the sources of the diffuse field have to be equipartioned and uniformly distributed in time and space (*Snieder*, 2004; *Sánchez-Sesma and Campillo*, 2006; *Tsai*, 2009, 2011). Seismologists have found those properties in coda waves(*Campillo and Paul*, 2003; *Snieder*, 2004), and in the ambient seismic field (*Shapiro and Campillo*, 2004; *Shapiro et al.*, 2005; *Sabra et al.*, 2005a).

Although seismic scattering may contribute to the equipartition of seismic waves traveling through the Earth, it does not necessarily overcome the non-uniform source distribution (*Stehly et al.*, 2006). The source of coda waves (CWs) are earthquakes, and are thus excited by seismically active regions. The microseismic background is the most energetic source of the ambient seismic field (ASF). It is excited by the coupling of oceanic waves with the oceanic floor and strongly illuminates the diffuse field from the coast.

Given the many uses of the ambient seismic field Green's functions, there is strong motivation to improve their accuracy. *Gallot et al.* (2011) use dense seismic arrays to reconstruct focusing (anti causal field) and defocusing (causal field) of the response function. *Baig et al.* (2009) build a time-frequency filter to de-noise single traces and improve accuracy in arrival time measurements. Higher-order correlations, or correlations of the coda of the Green's function, replicate multiple scattering more effectively (*Stehly et al.*, 2008), but a uniform distribution of the seismic stations, which are now considered as sources, become as important as a uniform distribution of local earthquakes, much like when constructing the Green's functions from coda-waves. The convergence of the correlation function toward a stable answer may be improved through data processing (*Bensen et al.*, 2007; *Seats et al.*, 2011), and we find that the simple correlation of unprocessed short time windows often converges sufficiently rapidly (e.g correlation coefficient at 0.9 after 2 weeks of stacking).

The Green's function emerges as the incoherent noise cancels out with incoherent stacking over a long period of time. To asses the accuracy of the Green's functions, we measure symmetry and causality of the correlation function. Symmetry refers to the conjugate symmetric waveform shape (phase and amplitude) on either side of the time zero axis. Causality indicates the order of arrival of seismic waves that is governed by the wave equation, and we call acausality its violation. When the source illumination is strongly directional, the condition of equipartition is not met, and asymmetry and acausality arise in the Green's function. Strong directionality is often the case in practice when the oceans consistently generate strong microseismic background, and this should be particularly true to southern California (*Stehly et al.*, 2006).

We propose to use constraints of causality and symmetry to construct hybrid Green's functions using both the ambient seismic field and coda waves. This study is motivated by the observation of the complementary directionality of the ambient seismic field and of the coda waves during our temporary deployment in southern California. We deployed a month prior to the El-Cucapah Mayor M7.2, 2010 earthquake and its aftershocks sequence. This interfered with our ambient seismic field measurement, but allowed us to take advantage of the local seismicity to construct Green's functions from coda-wave interferometry.

We show in Figure 6.1 the observations that motivated the notion of building hybrid Green's functions. The Green's functions are affected by the directionality of both fields and, in southern California, in a favorable manner. We construct the Green's function separately from the ambient seismic field, and from coda waves. In both cases, the Green's functions are either asymmetric with high signal-to-noise ratio, or weakly symmetric with low signal-to-noise ratio (Fig. 6.1). This suggests that we can improve the Green's functions by combining those two estimates. We propose to use the constraint that real Green's functions are both causal and time-symmetric to improve our ability to estimate them from data.

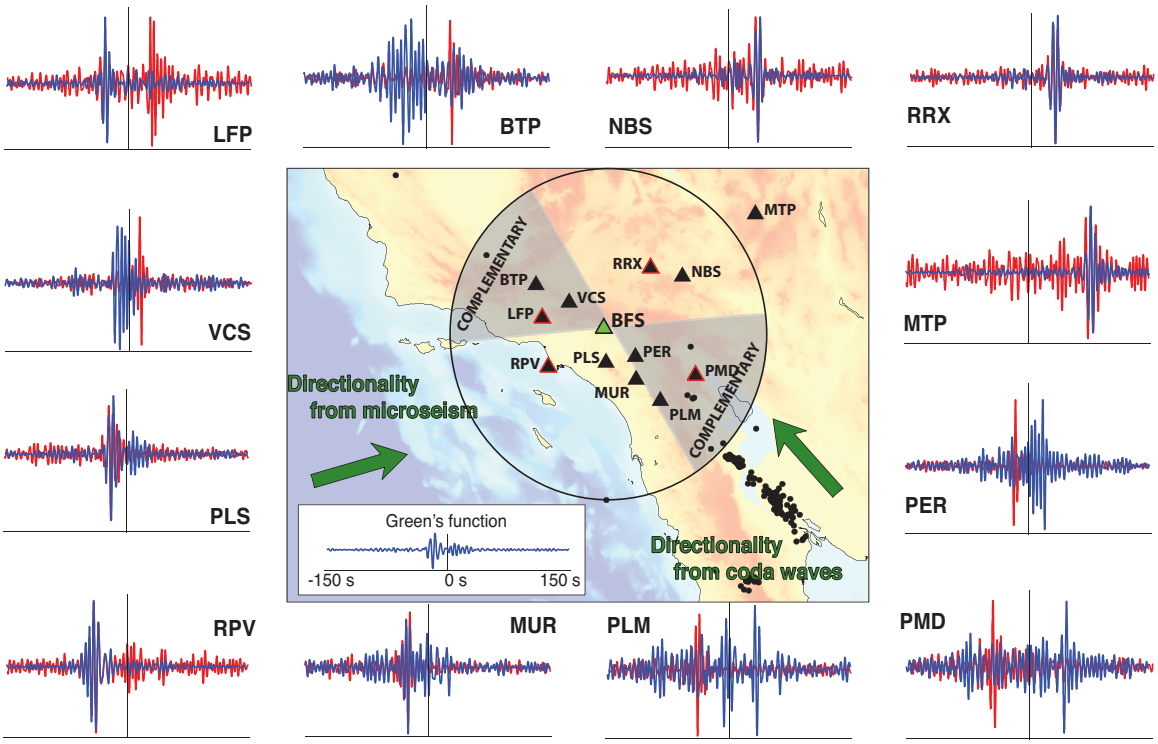

Figure 6.1: Complementary nature of the vertical-to-vertical Green's function that arises from directionality of the microseisms (blue waveforms) and of coda-waves from the El Mayor-Cucapah aftershock sequence(red waveforms) from the station source BFS to Southern California Seismic Network stations.

Ambient Seismic Field and Coda-wave Green's functions

We reconstruct Green's functions using an ensemble of cross-correlation functions that we calculate individually from the raw, unprocessed, short (30 minutes) time series of the ambient seismic field and of coda waves. For the ambient seismic field (ASF) data set, we only incorporate the time windows that do not contain earthquakes or instrumental noise (peak amplitude must be less than 10 times the standard deviation). We taper the edges, first and last 10% of time series using a cosine function. For the coda-wave (CW) data set, we use the SCSN catalog *Hauksson et al.* (2012) for location and timing of the local events during the same period of time of the ASF data set. We select the coda waves from the peak amplitude of the earthquake signal until we fill 1800s of signal, and remove the ballistic waves by padding the time series with zeros.

zero-pad the time series,

peak amplitude of the earthquake signal and keep the coda from the peak amplitude until we fill 1800 s of signal. If we encounter aftershocks in the coda, we stop at the peak amplitude immediately after start of the coda. Based on the observed signal levels, we chose to include approximately 50 events for our analysis. For each time window, we compute the Fourier Transform of each velocity times series for station A and B, respectively $v_A(t)$ and $v_B(t)$, in the frequency domain using the notation $F(\omega)$ for the Fourier transform of the time series $f(t)$:

$$\widehat{G}_{AB}(\omega) = \left\langle \frac{\hat{V}_A(\omega)\hat{V}_B^*(\omega)}{\{|\hat{V}_A(\omega)|\}^2} \right\rangle, \tag{6.1}$$

where the operator $\langle \quad \rangle$ denotes stacking over time, and $\{ \quad \}$ denotes smoothing over the virtual source spectrum (in our case a 6 mHz running average) to stabilize the deconvolution. We ignore any cross-spectrum that has a peak amplitude larger than 10^4 (equation 6.1 is non-dimensional).

Traditionally, we assume equal contributions of each correlation function to form the correlation stack. We stack in frequency domain, remove the mean of the spectrum, to avoid Fourier transform artifacts such as strong arrivals at $t = 0$, and finally inverse Fourier transform. We measure symmetry with the ratio of the peak amplitude on the causal side, with t_+ to note the positive lags, over the peak amplitude on the anti-causal side, noted t_- for negative lags. We measure the strength of causality using the norm of the energy (L_2 sense) within the time interval $t_{ac} = [d_{sr}/V_s d_{sr}/V_s]$, where d_{sr} is the distance between seismic stations, V_S is taken to be 5 km/s for the fastest surface-waves, and normalize by the energy of the entire time series: $||GF(t_{ac})||_2/||GF(t)||_2$.

Figure 6.2 shows the variation of symmetry and causality with respect to azimuth. We focus our measurements on the station sources of our temporary deployment and use stations of the entire Southern California Seismic Network as receivers. The symmetry of the ASF Green's functions (Fig. 6.2 (a-b)) varies with azimuth, showing the strongest causal arrivals for receivers located on the East of the source and the strongest anti-causal arrivals for receivers located on the West of the station source. This is likely an expression of the microseisms being generated in the Pacific Ocean. The CW Green's function symmetry is not as strong, but we see anti-correlation with the ASF Green's function symmetry. In parallel, the acausality is stronger when the symmetry is found close to one, which tends to represent a low signal to noise ratio. The azimuth where we see this effect correlates to the source-receiver axis parallel to the coast, which are paths that are unfavorably oriented with respect to the source of most of the ambient seismic field.

Green's functions that satisfy causality and symmetry

We propose to use the two physical constraints, causality and symmetry, to weight the contributions of individual correlations used to construct the Green's function. We solve for the weights that optimally satisfy the constraints on the stacked Green's

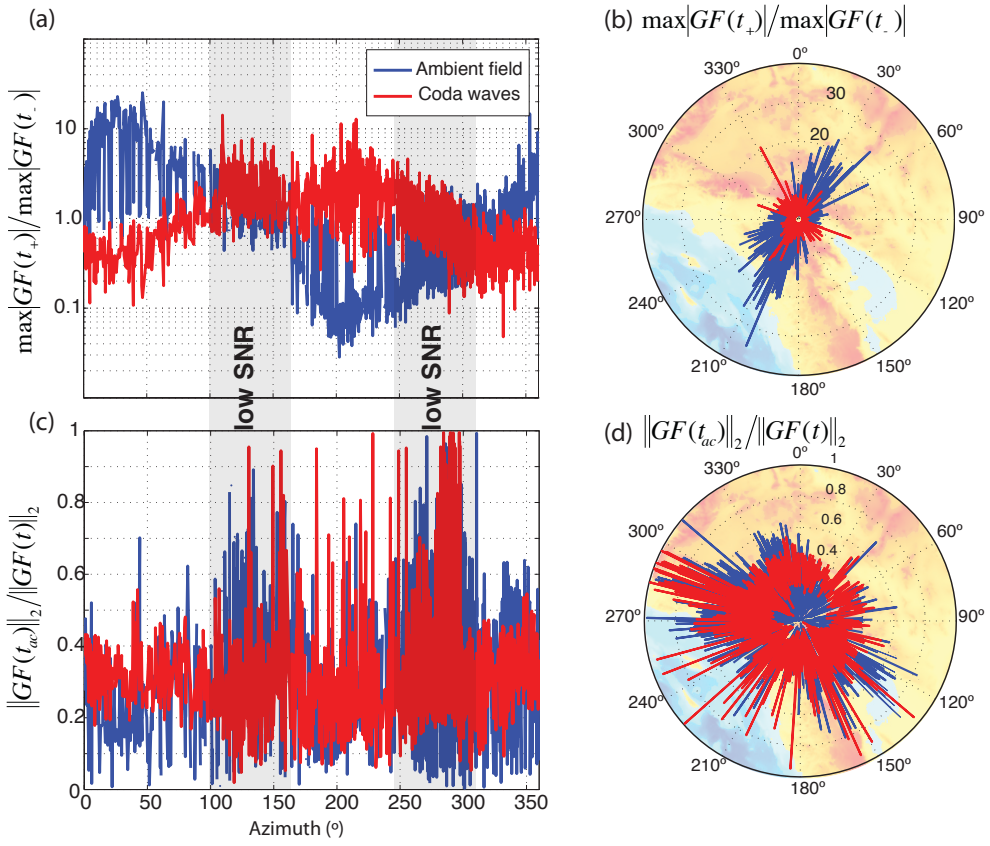

Figure 6.2: Symmetry and causality for both independent data sets measured from stations source in the Coachella Valley: Coda-waves (red) and Ambient seismic field (blue). (a-b) Ratio of peak amplitudes from causal over anti causal sides for cartesian and polar representation respectively. (c-d) Contribution of acausal energy in Green's functions for cartesian and polar representation respectively. (shaded gray areas) Zone of low signal to noise ratio (snr), and of strong acausality.

functions. Since the weights have to be strictly non-negative, this optimization is non-linear (Fig. 6.3).

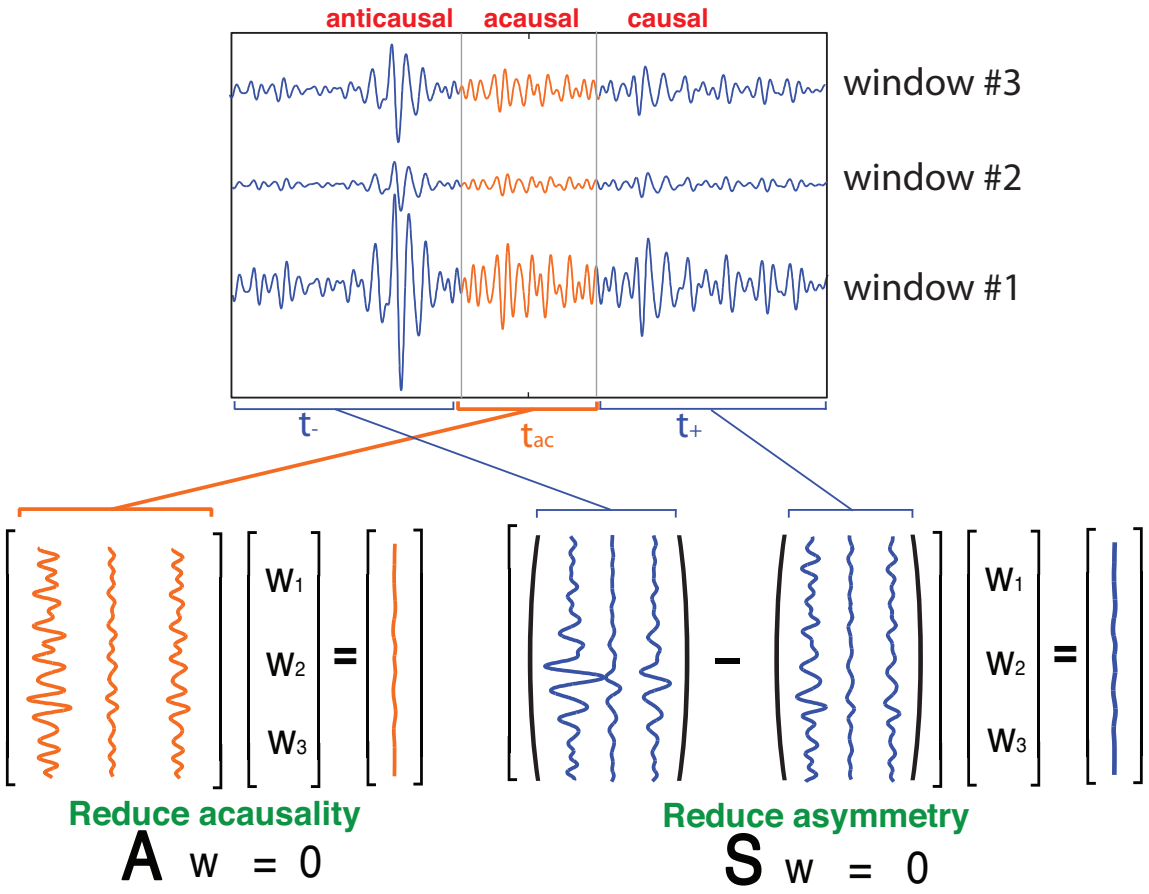

Figure 6.3: Improve causality (reduce acausality) and Improve symmetry (reduce asymmetry). (orange) acausal waveforms in windows 1, 2 and 3. (blue) coherent signal on causal and anti causal side. **A** is causality matrix, **S** is symmetry matrix.

We build two matrices with the waveforms from each correlation function. We want to minimize the acausal energy in the stack, i.e. find the best linear combination of the windows to minimize this energy. Alternatively, we can maximize symmetry, or minimize asymmetry, and build a matrix of the difference in both causal and anti causal waveforms. We write the objective function with respect to the vectors of

weights $\mathbf{w}$, or coefficients to that optimal linear combination:

$$\phi(\mathbf{w}) = ||\mathbf{A}\mathbf{w}||_2 + \alpha||\mathbf{S}\mathbf{w}||_2 + \lambda||\mathbf{L}\mathbf{w}||_2, \tag{6.2}$$

and we find the best α and λ so that we fit within a tolerance τ. We choose τ to be 20% of the noise level (L_2 norm of the acausal and late coda part). We guarantee a well behaved solution for the weights with a first order smoothing operator that prevent any window from dominating the stack.

The nonlinearity comes from imposing the weights to be strictly positive. We use the non linear least-square solver `lsqlin` from The Primal-Dual interior method for Convex Objectives (PDCO) (*Saunders*, 2010) to impose the constraints on the weights. We then loop over different values of α and λ to fit within tolerance, τ. We reduce the dimension of the system by pre-stacking the correlation functions at each day, and limiting the number of weights to solve. This also provides one way to balance the number of time windows from ASF and the ones from CW. Another way to achieve this balance is to impose the sum of the weights to be equal for ASF and for CW. We impose this with the condition:

$$\begin{bmatrix} 1 & \cdots & 1 & 0 & \cdots & 0 \\ 0 & \cdots & 0 & 1 & \cdots & 1 \end{bmatrix} \begin{bmatrix} w_1 \\ \vdots \\ w_{N0} \\ w_{N0+1} \\ \vdots \\ w_N \end{bmatrix} = \begin{bmatrix} 1/2 \\ 1/2 \end{bmatrix} \tag{6.3}$$

Equation 6.3 is easily implemented in the `lsqlin` algorithm, and we see how this problem may be generalized to other data sets than ASF and CW Green's functions.

Figure 6.4 illustrates an example of the Green's function estimation. The source is the seismic station MGE, and BZN is the receiver. We compute the ASF Green's functions stacked each day, along with the CW Green's function. Both sets of Green's functions are strongly asymmetric, but in the opposite sense (Fig. 6.4(c)). We see variation in causality (Fig. 6.4(a)) in the ensemble of Green's functions to stack. We

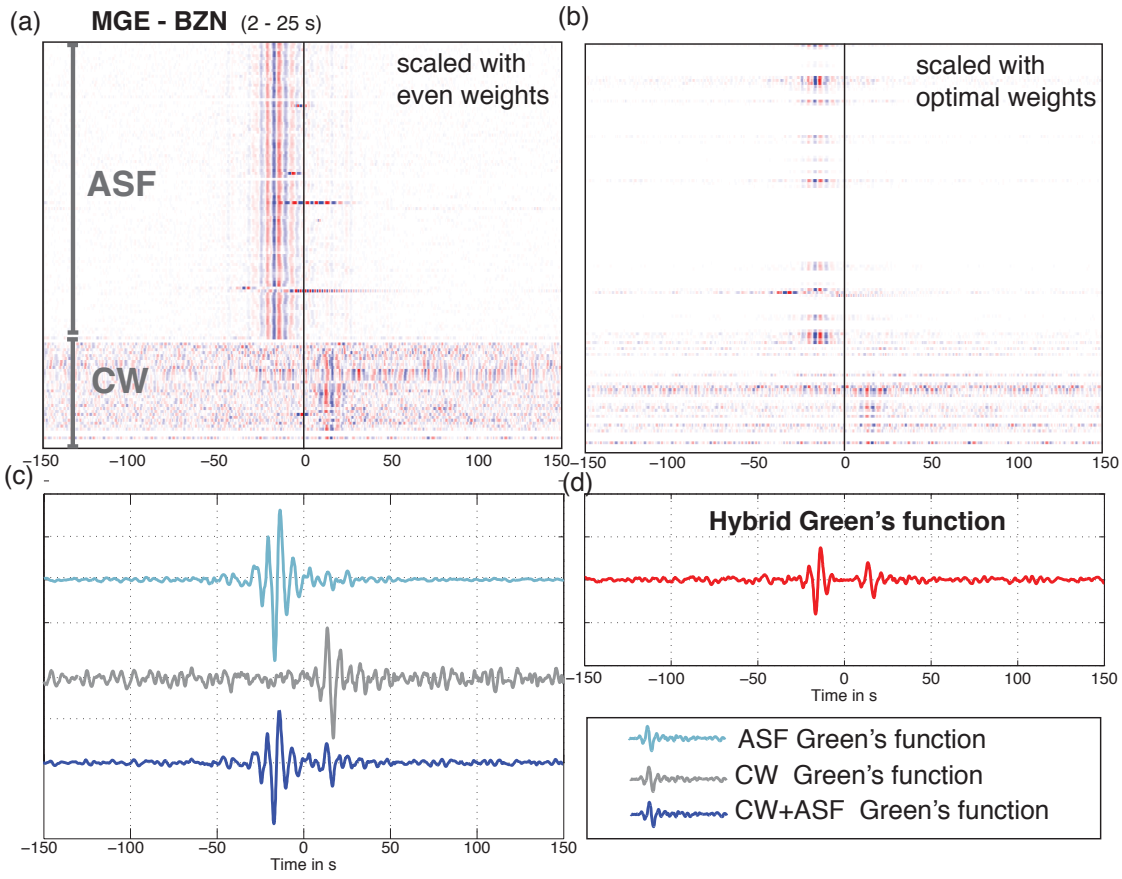

Figure 6.4: top panels: matrix representation of individual correlation function to stack color scaled with even weight (a) and optimal weight (b). bottom panels: stacked correlation functions with even weight (c) and optimal weights (d).

find the optimal weights as solutions of our inverse problem and color scale the individual Green's function traces in Figure 6.4(b) to form the hybrid Green's functions that satisfy conditions of causality and symmetry (Figure 6.4(d)).

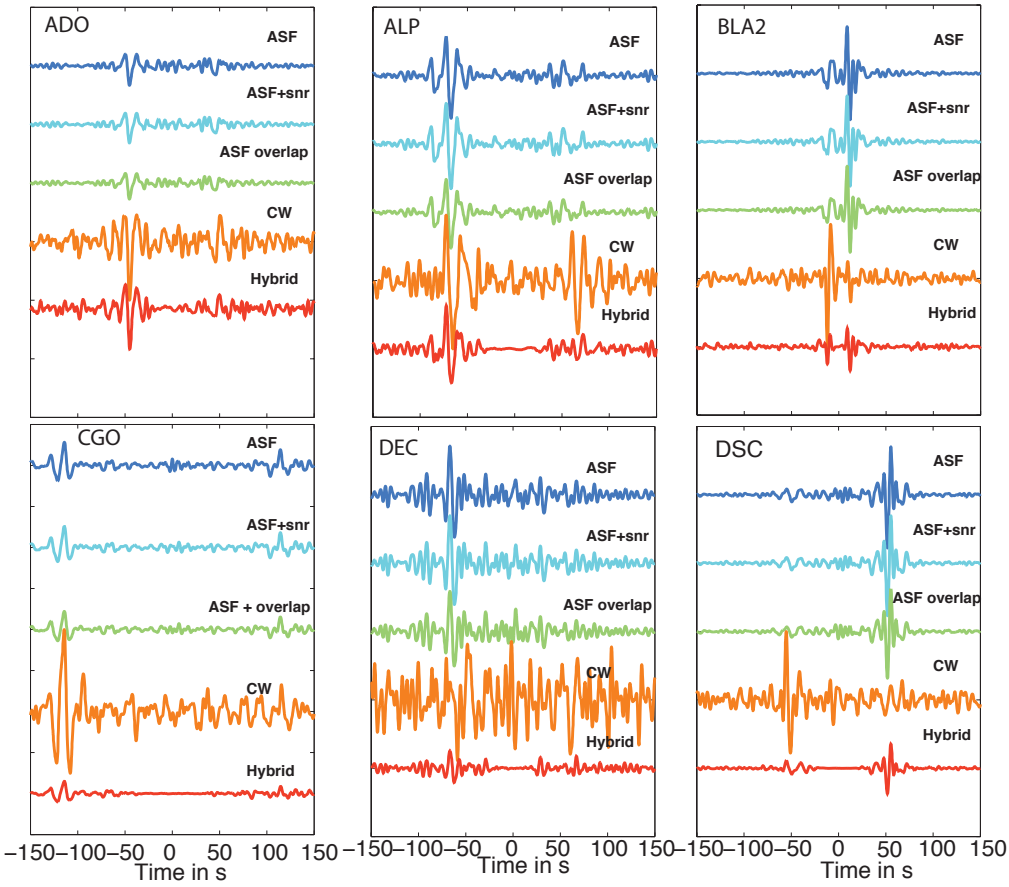

Figure 6.5: Hybrid Green's functions (orange waveforms) compared with other traditional approaches for estimating Green's functions: equal contribution of the correlation functions (blue), adaptive stacking scheme using the *snr* of the correlations (light blue waveforms), equal contributions of correlations functions obtained with overlapping time windows (green waveforms) and functions obtained by correlating coda waves (yellow waveforms).

We compare in Figure 6.5 the Green's functions obtained from different techniques with our hybrid Green's function. First, we use an even contribution of the individual correlation functions for the raw ASF, and labeled as such. Second, and with the same data set, we construct a stack with a weighted contribution that depends on the

signal-to-noise ratio (*Riedesel et al.*, 1980) $w_i = 1/snr_i, \forall i \in [1, N_w]$, where N_w is the number of correlation functions to stack and snr_i is the signal-to-noise ratio of the ith correlation function. The third function we compare uses overlapping ambient seismic field time windows (*Seats et al.*, 2011) and equal weights for all correlation functions. Finally, we compare our results with the functions calculated from correlating the coda-waves, stacked with equal contributions.

Figure 6.5 shows a limited set of comparisons between the different functions and our estimate of hybrid Green's functions. In all cases, we retrieve stronger causality, when it is enforced for the hybrid Green's functions, which combines the information from the two independent data sets (ASF and CW). The functions obtained with the overlapping time windows, or with the adaptive stack resemble strongly the ASF function of reference. This confirms the fast convergence toward a unique solution of our estimate of the Green's function. We also note that the CW functions have higher amplitude, and we suggest that the higher amplitudes of the coda waves compared to the ambient seismic field can explain this difference. The symmetry is only possible if the gather of correlation functions considered actually contain functions with accurate Green's function information for both the causal and anti-causal time periods. We see for an ensemble of 400 station pairs in Figure 6.6 for which we successfully improve the Green's function symmetry by combining the two independent data sets. The ASF Green's functions we use are strongly asymmetric, whereas the directionality of the coda waves seem to be less affecting the symmetry of the Green's functions. Nevertheless, we successfully reconstruct hybrid Green's functions with stronger causality and symmetry.

Conclusions

In this study, we have improved the Green's functions obtained from correlation of ambient seismic field and coda waves over a short recording period. We have shown how we can incorporate independent estimates of the Green's functions to reconstruct a hybrid Green's function that better satisfy causality and symmetry. Most importantly, we developed a new approach that optimally construct Green's functions that

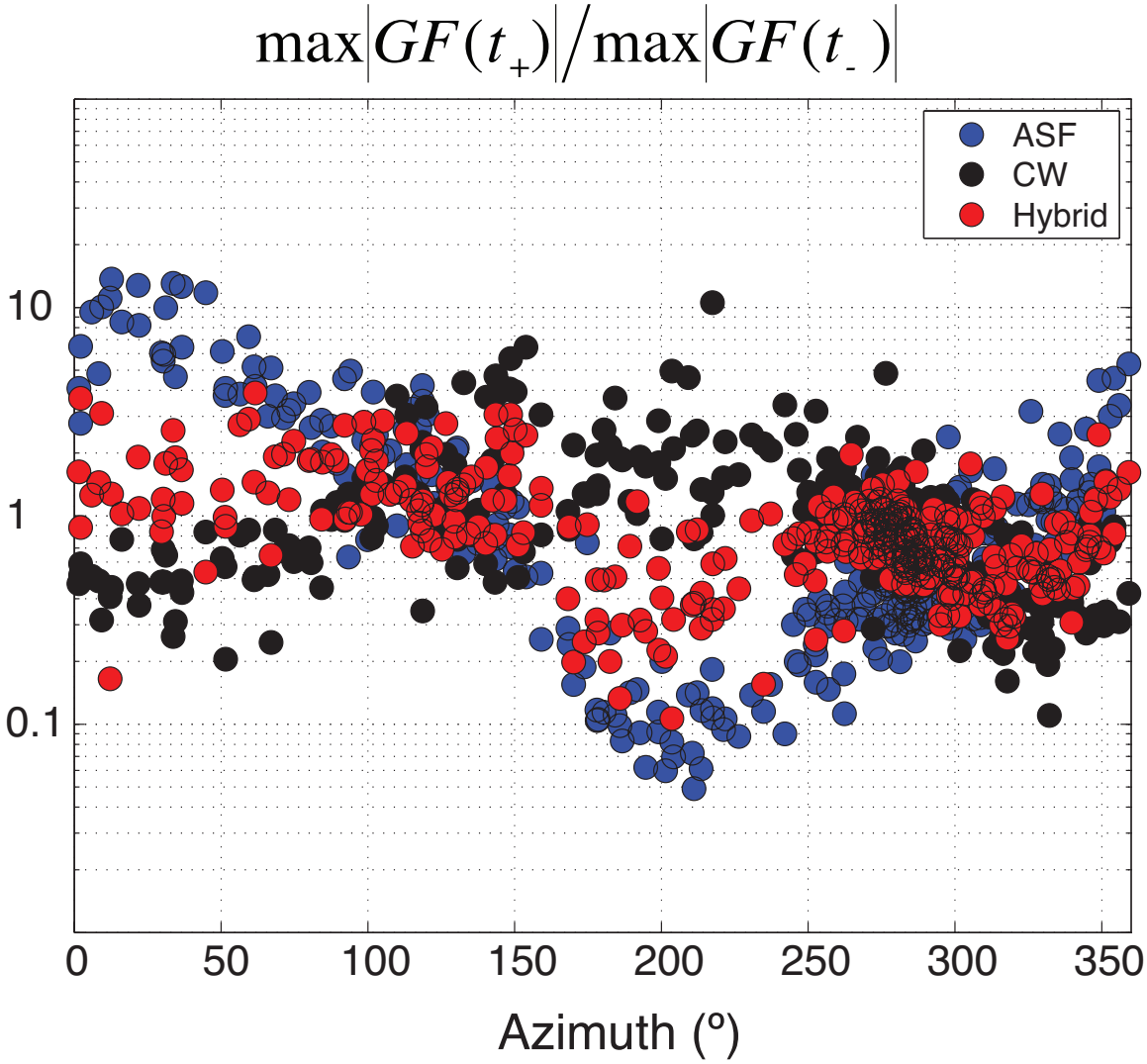

Figure 6.6: Same as Figure 6.2(a): ratio of the peak amplitudes of the causal over the anti causal sides for the ASF (blue filled circles) and CW (gray filled circles) Green's functions with our estimate (red filled circles) from constraining causality an symmetry.

can be generalized to other, independent, data sets such as the responses obtained during active seismic surveys, or using higher-order correlation techniques.

Unlike the traditional approach that relies on non-uniform illumination of the diffuse field, this approach virtually replicates a more uniform distribution of the noise sources. It does not require information of the noise source distribution and only allows the physical constraints of causality and symmetry to simulate the conditions of equipartition. We anticipate future work that would investigate further the obstacles of causality, and most importantly, the contributions of this approach to construct Green's functions with higher-order correlation functions.

Bibliography

Abrahamson, N. A., and K. M. Shedlock (1997), Overview, *Seismol. Res. Lett.*, *68*, 9–23, doi:10.1785/gssrl.68.1.9.

Abrahamson, N. A., W. J. Silva, and R. Kamai (2013), Update of the AS08 Ground-Motion Prediction Equations Based on the NGA-West2 Data Set, *PEER Report 2013/04*.

Adams, B. M. (2000), Basin-Edge Effects from the Sh-Wave Modeling with Reference to the Lower Hutt Valley, New Zealand, Ph.D. thesis, Department of Civil Engineering, University of Canterbury, Christchurch, New Zealand.

Afnimar, K. Koketsu, and M. Komazawa (2003), 3-D Structure of the Kanto basin, Japan from Joint Inversion of Refraction and Gravity Data, in *IUGG 2003 Scientific Program and Abstracts*, edited by IUGG, pp. SS04/07A/A03–002,B.487.

AIST (2012), Active Fault Database of Japan, February 28, 2012 version, research Information Database DB095 National Institute of Advanced Industrial Science and Technology (AIST).

Aki, K. (1957), Space and Time Spectra of Stationary Stochastic Waves, with Special Reference to Microtremors, *Bull. Earthq. Res. Inst. Univ. Tokyo*, *35*, 415–456.

Aki, K. (1993), Local Site Effects on Weak and Strong Ground Motion, *Tectonophysics*, *218*, 93–111, doi:10.1016/0040-1951(93)90262-I.

Aki, K., and P. G. Richards (2002), *Quantitative Seismology, Second Edition*, 700 pp., University Science Books, Sausalito, California.

Ascher, U., and P. Spudich (1986), A hybrid collocation method for calculating complete theoretical seismograms in vertically varying media, *Geophys. J. Roy. Astr. S.*, *86*, 19–40.

Baig, A. M., M. Campillo, and F. Brenguier (2009), Denoising seismic noise cross correlations, *J. Geophys. Res.*, *114*, B08,310.

Baltay, A. A., S. Ide, G. Prieto, and G. C. Beroza (2011), Variability in earthquakes stress drop and apparent stress, *Geophys. Res. Lett.*, *38*, L06,303, doi: 10.1029/2011GL046698.

Bard, P.-Y., M. Campillo, F. J. Chávez-Garcia, and F. J. Sánchez-Sesma (1988), The Mexico Earthquake of September 19, 1985 - A Theoretical Investigation of Large- and Small-scale Amplification Effects in the Mexico City Valley, *Earthquake Spectra*, *4*(3), 609–633.

Bensen, G. D., M. H. Ritzwoller, M. P. Barmin, A. L. Levshin, F. Lin, M. P. Moschetti, N. M. Shapiro, and Y. Yang (2007), Processing seismic ambient noise data to obtain reliable broad-band surface waves dispersion measurements, *Geophys. J. Int.*, *169*, 1239–1260, doi:10.1111/j.1365-246X.2007.03374.x.

Bensen, G. D., M. H. Ritzwoller, and N. M. Shapiro (2008), Broadband ambient noise surface wave tomography across the United States, *J. Geophys. Res.*, *113*, B05,306.

Brenguier, F., N. M. Shapiro, V. Ferrazzini, Z. Duputel, O. Coutant, and A. Nercessian (2008a), Towards forecasting volcanic eruptions using seismic noise, *Nature Geosciences*, *1*, 126–130, doi:10.1038/ngeo104.

Brenguier, F., M. Campillo, C. Hadziiannou, N. M. Shapiro, R. M. Nadeau, and E. Larose (2008b), Postseismic Relaxation Along the San Andreas Fault at Parkfield from Continuous Seismological Observations, *Science*, *321*, 1478–1479, doi: 10.1126/science.1160943.

Buchen, P. W., and R. Ben-Hador (1996), Free-mode surface-wave computations, *Geophys. J. Int.*, *124*, 869–887.

Burridge, R., and L. Knopoff (1964), Body force equivalents for seismic dislocations, *B. Seismol. Soc. Am.*, *54*(1875-1888).

Campbell, K. W., and Y. Bozorgnia (2003), Updated Near-Source Ground-Motion (Attenuation) Relations for the Horizontal and Vertical Components of Peak Ground Acceleration and Acceleration Response Spectra, *B. Seismol. Soc. Am.*, *93*(1), 314–331.

Campbell, K. W., and Y. Bozorgnia (2013), NGA-West2 Campbell-Bozorgnia Ground Motion Model for the Horizontal Components of PGA, PGV, and 5%-Damped Elastic Pseudo-Acceleration Response Spectra for Periods Ranging from 0.01 to 10 sec, *PEER Report 2013/06*.

Campillo, M., and A. Paul (2003), Long-Range Correlations in the Diffuse Seismic Coda, *Science*, *299*(5606), 547–549, doi:doi:10.1126/science.1078551.

Claerbout, J. (1968), Synthesis of a layered medium from its acoustic transmission response, *Geophysics*, *33*(2), 264–259.

Cupillard, P., L. Stehly, and B. Romanowicz (2011), The one-bit noise correlation: a theory based on the concepts of coherent and incoherent noise, *Geophys. J. Int.*, *184*, 1397–1414.

Dahlen, F. A., and J. Tromp (1998), *Theoretical Global Seismology*, 944 pp., Princeton University Press, Princeton, New Jersey.

Day, S. M., R. Graves, J. Bielak, D. Dreger, S. Larsen, K. B. Olsen, A. Pitarka, and L. Ramirez-Guzman (2008), Model for Basin Effects on Long-Period Response Spectra in Southern California, *Earthquake Spectra*, *24*(1), 257–277.

Day, S. M., D. Roten, and K. B. Olsen (2012), Adjoint analysis of the source and path sensitivities of basin-guided waves, *Geophys. J. Int.*, *189*, 1103–1124.

Denolle, M. A., E. M. Dunham, and G. C. Beroza (2012), Solving the Surface-Wave Eigenproblem with Chebyshev Spectral Collocation, *B. Seismol. Soc. Am.*, *102*, 1214–1223, doi:10.1785/0120110183.

Denolle, M. A., E. M. Dunham, G. A. Prieto, and G. C. Beroza (2013), Ground motion prediction of realistic earthquake sources using the ambient seismic field, *J. Geophys. Res.*, *118*, 1–17, doi:10.1029/2012JB009603.

Duputel, Z., V. Ferrazzini, F. Brenguier, N. M. Shapiro, M. Campillo, and A. Nercessian (2009), Real time monitoring of relative velocity changes using ambient seismic noise at the Piton de la Fournaise volcano (La Réunion) from January 2006 to June 2007, *J. Volcanol. Geotherm. Res.*, *184*, 164–173.

Ewing, M., W. S. Jardetzky, and F. Press (1957), *Elastic Waves in Layered Media*, 380 pp., McGraw-Hill Book Co., New York.

Froment, B., M. Campillo, P. Roux, P. Gouédard, A. Verdel, and R. L. Weaver (2010), Estimation fo the effect of nonisotropically distributed energy on the apparent arrival time in correlations, *Geophysics*, *75*(5), SA85–SA93.

Furumura, T., and T. Hayakawa (2007), Anomalous Propagation of Long-Period Ground Motions Recorded in Tokyo during the 23 October 2004 Mw 6.6 Niigata-ken Chuetsu, Japan, Earthquake, *B. Seismol. Soc. Am.*, *97*(3), 863–880.

Furumura, T., and B. L. N. Kennett (1998), On the nature of regional seismic phases - iii. The influence of crustal heterogeneity on the wavefield for subduction earthquakes: the 1985 Michoacan and 1995 Copala, Guerrero, Mexico earthquakes, *Geophys. J. Int.*, *135*, 1060–1084.

Gallot, T., S. Catheline, P. Roux, and M. Campillo (2011), A passive inverse filter for Green's function retrieval, *J. Acoust. Soc. Am.*, *131*(1).

Graves, R., A. Pitarka, and P. G. Somerville (1998), Ground-Motion Amplification in the Santa Monica Area: Effects of Shallow Basin-Edge Structure, *B. Seismol. Soc. Am.*, *88*(5), 1224–242.

Graves, R., T. H. Jordan, S. Callaghan, E. Deelman, E. Field, G. Juve, C. Kesselman, P. Maechling, G. Mehta, K. Milner, D. Okaya, P. Small, and K. Vahi (2011),

Cybershake: A Physics-Based Seismic Hazard Model for Southern California, *Pure and Applied Geophysics*, *168*(3-4), 367–381.

Gregersen, S. (1978), Possible mode conversion between Love and Rayleigh waves at a continental margin, *Geophys. J. Roy. Astr. S.*, *54*, 121–127, doi:10.1111/j.1365-246X.1978.tb06759.x.

Guatteri, M., P. M. Mai, and G. C. Beroza (2004), A Pseudo-Dynamic Approximation to Dynamic Rupture Models for Strong Ground Motion Prediction, *B. Seismol. Soc. Am.*, *94*(6), 2051–2063.

Hanks, T., and W. Thatcher (1972), A Graphical Representation of Seismic Source Parameters, *J. Geophys. Res.*, *77, no. 23*, 4393–4405, doi: 10.1029/JB077i023p04393.

Hartzell, S., A. Frankel, P. Liu, Y. Zeng, and S. Rahman (2011), Model and Parametric Uncertainty in Source-Based Kinematic Models of Earthquake Ground Motion, *B. Seismol. Soc. Am.*, *101, no. 5*, 2431–2452, doi:10.1785/0120110028.

Harvey, D. J. (1981), Seismogram synthesis using normal mode superposition: the locked mode approximation, *Geophys. J. Roy. Astr. S.*, *66*, 37–69.

Haskell, N. A. (1953), The Dispersion of Surface Waves on Multilayered Media, *B. Seismol. Soc. Am.*, pp. 17–34s.

Hauksson, E., K. Felzer, D. Given, M. Giveon, S. Hough, K. Hutton, H. Kanamori, V. Sevilgen, Shengji, and A. Yong (2008), Preliminary Report on the 29 July 2008 Mw 5.4 Chino Hills, Eastern Los Angeles Basin, California, Earthquake Sequence, *Seismol. Res. Lett.*, *79, no. 6*, 855–866, doi:10.1785/gssrl.79.6.855.

Hauksson, E., W. Yang, and P. M. Shearer (2012), Waveform Relocated Earthquake Catalog for Southern California (1981 to 2011), *B. Seismol. Soc. Am.*, *102*(5), 2239–2244.

Herrmann, R. B. (1978), Computer Programs in Earthquake Seismology, Volume 2: General Programs, *Tech. rep.*, Saint Louis University.

Iwaki, A., and T. Iwata (2010), Simulations of long-period ground motion in the Osaka sedimentary basin: performance estimation and the basin structure effects, *Geophys. J. Int.*, *181*, 1062–1076.

Karplus, M. S., S. L. Klemperer, J. F. Lawrence, W. Zhao, J. Mechie, F. Tilmann, E. Sandvol, and J. Ni (2013), Ambient-noise tomography of north Tibet limits geological terrane signature to upper-middle crust, *Geophys. Res. Lett.*, *40*, 808–813.

Kasahara, K., S. Sakai, Y. Morita, N. Hirata, N. Tsuruoka, S. Nakagawa, K. Nanjo, and K. Obara (2009), Development of the Metropolitan Seismic Observation Network (MeSO-net) for Detection of Mega-thurst beneath Tokyo Metropolitan Area, *Bull. Earthq. Res. Inst. Univ. Tokyo*, *84*, 71–88.

Kawabe, H., and K. Kamae (2008), Prediction of long-period ground motions from huge subduction earthquakes in Osaka, Japan, *J. Seismol*, *12*, 173–184.

Kawase, H. (1996), The cause of the damage belt in Kobe, the "basin edge effect", constructive interference of the direct S-wave with the basin-induced diffracted/Rayleigh waves, *Seismol. Res. Lett.*, *67*(5), 25–34.

Kennett, B. L. N. (1974), Reflections, rays and reverberations, *B. Seismol. Soc. Am.*, *64*(6), 1685–1696.

Kennett, B. L. N. (2009), *Seismic wave propagation in stratified media*, 497 pp., The Australian National University, Canberra, Australia.

Kennett, B. L. N., and T. J. Clarke (1979), Seismic waves in a stratified half space, *Geophys. J. Roy. Astr. S.*, *57*, 557–583.

Kirrmann, P. (1995), On the completeness of Lamb modes, *J. Elasticity*, *37*, 36–39.

Knopoff, L. (1964), A Matrix Method for Elastic Wave Problems, *B. Seismol. Soc. Am.*, *54, No. 1*, 431–438.

Kohler, M. D., H. Magistrale, and R. W. Clayton (2003), Mantle heterogeneities at the SCEC reference three-dimensional Seismic Velocitiy Model Version 3, *B. Seismol. Soc. Am*, *93*(2), 757–774.

Koketsu, K., and H. Miyake (2008), A seismoloigical overview of long-period ground motion, *J. Seismol*, *12*, 133–143.

Koketsu, K., K. Hatayama, T. Furumura, Y. Ikegami, and S. Akiyama (2005), Damaging Long-period Ground Motions from the 2003 Mw 8.3 Tokachi-oki, Japan, Earthquake, *Seismol. Res. Lett.*, *76*(1), 67–73.

Koketsu, K., H. Miyake, Afnimar, and Y. Tanaka (2009), A proposal for a standard procedure of modeling 3-D velocity structures and its application to the Tokyo metropolitan area, Japan, *Tectonophysics*, *472*, 290–300.

Langston, C. A., S.-C. C. Chiu, Z. Lawrence, P. Bodin, and S. Horton (2009), Array Observations of Microseismic Noise and the Nature of H/V in the Mississippi Embayment, *B. Seismol. Soc. Am*, *99*(5), 2893–2911, doi:10.1785/0120080189.

Lawrence, J. F., and G. A. Prieto (2011), Attenuation tomography of the western United States from ambient seismic noise, *J. Geophys. Res.*, *116*, B06,302, doi: 10.1029/2010JB007836.

Lawrence, J. F., M. A. Denolle, K. J. Seats, and G. A. Prieto (in press), A numeric evaluation of attenuation from ambient noise correlation functions, *J. Geophys. Res.*

Lin, F.-C., M. P. Moschetti, and M. Ritzwoller (2008), Surface wave tomography of the western United States from ambient seismic noise: Rayleigh and Love wave phase velocity maps, *Geophys. J. Int.*, *2007*, doi:10.1111/j.1365-246X.2008.03720.x.

Lin, F.-C., V. C. Tsai, and M. H. Ritzwoller (2012), The local amplification of surface-waves: A new observable to constrain elastic velocities, density and anelastic attenuation, *J. Geophys. Res.*, *117*, B06,302.

Lobkis, O. I., and R. L. Weaver (2001), On the emergence of the Green's fucntion in the correlations of a diffuse field, *J. Acoust. Soc. of Am.*, *110*, 3001–3017, doi: 10.1121/1.1417528.

Lysmer, J. (1970), Lunped Mass Method for Rayleigh Waves, *B. Seismol. Soc. Am*, *60*(1), 89–104.

Magistrale, H., S. Day, R. W. Clayton, and R. Graves (2000), The SCEC Southern California Reference Three-Dimensional Seismic Velocity Model Version 2, *B. Seismol. Soc. Am*, *90, 6B*, S65–S76.

Minato, S., T. Tsuji, S. Ohmi, and T. Matsuoka (2012), Monitoring seismic velocity changes caused by the 2011 Tohoku-oki earthquake using ambient noise records, *Geophys. Res. Lett.*, *39*, L09,309.

Miyake, H., and K. Koketsu (2005), Long-period ground motions from a large offshore earthquake: The case of teh 2004 off the Kii peninsula earthquake, Japan, *Earth Planets Space*, *57*, 203–207.

Moler, C. B., and G. W. Stewart (1973), An algorithm for generalized matrix eigenvalue problems, *SIAM Journal of Numerical Analysis*, *10*(2), 241–256.

Moschetti, M. P., M. H. Ritzwoller, F.-C. Lin, and Y. Yang (2010), Crustal shear velocity structure of the western US inferred from ambient noise and earthquake data, *J. Geophys. Res.*, *115*, B10,306.

Nishida, K., H. Kawakatsu, and K. Obara (2008), Three-dimensional crustal S wave velocity structure in Japan using microseismic data recorded by Hi-net tiltmeters, *J. Geophys. Res.*, *113*, B10,302, doi:10.1029/2007JB005395.

Obara, K., K. Kasahara, S. Hori, and Y. Okada (2005), A densely distributed high-sensitivity seismograph network in Japan: Hi-net by National Research Institute for Earth Science and Disaster Prevention, *Rev. Sci. Instrum.*, *76*, 021,301.

Okada, Y., K. Kasahara, K. Obara, S. Sekuguchi, H. Fujiwara, and A. Yamamoto (2004), Recent progress of seismic observation networks in Japan -Hi-net, F-net, K-NET and KiK-net, *Earth Planets and Space*, *56*, xv–xviii.

Olsen, K., S. M. Day, J. Minster, Y. Cui, A. Chourasia, M. Faerman, R. Moore, P. Maechling, and T. Jordan (2006), Strong shaking in Los Angeles expected from southern San Andreas earthquakes, *Geophys. Res. Lett.*, *33*, L07,305, doi: 10.1029/2005GL025472.

Olsen, K. B. (2000), Site Amplitifcation in the Los Angeles Basin from the Three-Dimensional Modeling of Ground Motion, *B. Seismol. Soc. Am*, *90*(6B), S77–S94.

Olsen, K. B., R. J. Archuleta, and J. R. Matarese (1995), Three-Dimensiontal Simulation of a magnitude 7.75 Earthquake on the San Andreas Fault, *Science*, *270*.

Olsen, K. B., S. M. Day, L. A. Dalguer, J. Mayhew, Y. Cui, J. Zhu, V. Cruz-Atienza, D. Roten, P. Maechling, T. H. Jordan, D. Okaya, and A. Chourasia (2009), ShakeOut-D: Ground motion estimates using an ensemble of large earthquakes on the San Andreas fault with spontaneous rupture propagation, *Geophys. Res. Lett.*, *36*, L04,303, doi:10.1029/2008GL036832.

Pei, D., J. N. Louie, and S. K. Pullammanappallil (2008), Improvements on computation of phase velocities of Rayleigh waves based on the generalized R/T coefficient methods, *B. Seismol. Soc. Am*, *98*(1), 280–287.

Pestel, E. C., and F. A. Leckie (1963), *Matrix-Methods in Elasto-Mechanics*, 453 pp., McGraw-Hill, New York.

Pitarka, A., K. Irikura, T. Iwata, and H. Sekiguchi (1998), Three-Dimensional Simulation of the Near-Fault Ground Motion for the 1995 Hyogo-ken Nanbu (Kobe), Japan, Earthquake, *B. Seismol. Soc. Am*, *88*(2), 428–440.

Prieto, G. A., and G. C. Beroza (2008), Earthquake Ground Motion Prediction Using the Ambient Seismic Field, *Geophys. Res. Lett.*, *35*, doi:10.1029/2008GL034428.

Prieto, G. A., J. F. Lawrence, and G. C. Beroza (2009), Anelastic Earth Structure from the Coherency of the Ambient Seismic Field, *J. Geophys. Res.*, *114*, doi: 10.1029/2008JB006067.

Prieto, G. A., M. Denolle, J. F. Lawrence, and G. C. Beroza (2011), On amplitude information carried by the ambient seismic field, *C. R. Geosci.*, *343*, 600–614, doi: 10.1016/j.crte.2011.03.006.

Rickett, J., and J. Claerbout (1999), Acoustic daylight imaging via spectral factorization: Helioseismology and reservoir monitoring, *The Leading Edge*, *18*(957-960).

Riedesel, M. A., D. Agnew, J. Berger, and F. Gilbert (1980), Stacking for the frequencies and Qs of ${}_0S_0$ and ${}_1S_0$, *Geophys. J. Roy. Astr. S.*, *62*, 457–471.

Roux, P. (2009), Passive seismic imaging with directive ambient noise: application to surface waves and the San Andreas Fault in Parkfield, CA, *Geophys. J. Int.*, *179*, 367–373.

Sabra, K. G., P. Gerstoft, P. Roux, W. A. Kuperman, and M. C. Fehler (2005a), Extracting time-domain Green's function estimates from ambient seismic noise, *Geophys. Res. Lett.*, *32*, L03,310, doi:10.1029/2004GL021862.

Sabra, K. G., P. Gerstoft, P. Roux, W. A. Kuperman, and M. C. Fehler (2005b), Surface wave tomography from microseisms in Southern California, *Geophys. Res. Lett.*, *32*, L14,311, doi:10.1029/2005GL023155.

Sakai, S., and N. Hirata (2009), Distribution of the Metropolitan Seismic Observation network, *Bull. Earthq. Res. Inst. Univ. Tokyo*, *84*(57-69).

Sánchez-Sesma, F. J., and M. Campillo (2006), Retrieval of the Green's Function from Cross Correlation: The Canonical Elastic Problems, *B. Seismol. Soc. Am*, *96*, 1182–1191, doi:10.1785/0120050181.

Sánchez-Sesma, F. J., J. A. Pérez-Ruiz, F. Luzón, M. Campillo, and A. Rodríguez-Castellanos (2008), Diffuse fields in dynamic elasticity, *Wave Motion*, *45*(5), 641–654.

Saunders, M. (2010), PDCO Matlab software for convex optimization, *http://www.stanford.edu/group/SOL/software.html*.

Savage, J. C., W. Gan, and J. L. Svarc (2001), Strain accumulation and rotation in the Eastern California Shear Zone, *J. Geophys. Res.*, *106*(B10), 21,995–22,007, doi:10.1029/2000JB000127.

Schwab, F., and L. Knopoff (1971), Surface waves on multilayered anelastic media, *B. Seismol. Soc. Am*, *61*(4), 893–912.

Seats, K. J., J. F. Lawrence, and G. A. Prieto (2011), Improved ambient noise correlation functions using Welch's methods, *Geophys. J. Int.*, *188*, 513–523, doi: 10.1111/j.1365-246X.2011.05263.x.

Shapiro, N. M., and M. Campillo (2004), Emergence of broadband Rayleigh waves from correlations of the ambient seismic noise, *Geophys. Res. Lett.*, *31*, L07,614, doi:10.1029/2004/GL019491.

Shapiro, N. M., M. Campillo, L. Stehly, and M. H. Ritzwoller (2005), High-Resolution Surface Wave Tomography from Ambient Seismic Noise, *Science*, *307*, 1615–1617, doi:10.1126/science.1108339.

Snieder, R. (2004), Extracting the Green's function from the correlation of coda waves: A derivation based on stationay phase, *Phys. Rev. E*, *69(4)*, 046,610–1–7, doi:10.1103/PhysRevE.69.046610.

Spudich, P., and U. Ascher (1983), Calculation of complete theoretical seismograms in vertically varying media using collocation methods, *Geophys. J. Roy. Astr. S.*, *75*, 101–124.

Stehly, L., M. Campillo, and N. M. Shapiro (2006), A study of the seismic noise from its long-range correlation properties, *J. Geophys. Res.*, *111*, B10,306.

Stehly, L., M. Campillo, B. Froment, and R. L. Weaver (2008), Reconstructing Green's function by correlation of the code of the correlation (c^3) of ambient seismic noise, *J. Geophys. Res.*, *113*, B11,306, doi:doi:10.1029/2008JB005693.

Takeuchi, H., and N. Saito (1972), *Methods in Computational Physics*, chap. Seismic Surface Waves, pp. 217–295, Bolt, B. A., Academic Press, New York.

Tanaka, Y., K. Koketsu, H. Miyake, T. Furumura, H. Sato, N. Hirata, H. Suzuki, and T. Masuda (2005), Integrated modeling of 3D velocity structure beneath the Tokyo metropolitan area, *Eos Trans. AGU*, *86*(52), Abstract S21A–0200.

Tanimoto, T., and L. Rivera (2005), Prograde Rayleigh wave particle motion, *Geophys. J. Int.*, *162*, 399–405, doi:10.111/j.1365-246X.2005.02481.x.

Thomson, W. T. (1950), Transmission of Elastic Waves through a Stratified Solid Medium, *J. Appl. Phy.*, *21*, 89–93.

Toro, G. R., N. A. Abrahamson, and J. F. Schneider (1997), Model of Strong Ground Motion from Earthquakes in Central and Eastern North America: Best Estimates and Uncertainties, *Seismol. Res. Lett.*, *68*, 41–57, doi:10.1785/gssrl.68.1.41.

Trefethen, L. N. (2000), *Spectral Methods in MATLAB*, 165 pp., Society of Industrial and Applied Mathematics, SIAM, Philadelphia.

Tsai, V. C. (2009), On establishing the accuracy of noise tomography travel-time measurements in a realistic medium, *Geophys. J. Int.*, *178*, 1555–1564.

Tsai, V. C. (2011), Understanding the amplitudes of noise correlation measurements, *J. Geophys. Res.*, *116*, B09,311.

Tsuno, S., H. Yamanaka, S. Midorikawa, S. Yamamoto, H. Miura, S. Sakai, N. Hirata, K. Kasahara, H. Kimura, and T. Aketagawa (2012), Characteristics of Long-Period Ground Motions in the Tokyo Metropolitan Area and its Vicinity, by Recording Data of the 2011 Off the Pacific Coast of Tohoku Earthquake (Mw 9.0) and the Aftershocks, *Journal of Japan Association for Earthquake Engineering*, *12*(5), 102–116.

Tsuno, S., A. M. Pramatadie, Y. P. Dhakal, K. Chimoto, W. Tsutsumi, and H. Yamanaka (2013), Long-Period Ground Motions Observed in the Northern Part of

Kanto Basin, During the 2011 off the Pacific Coast of Tohoku Earthquake, Japan, *Journal of Japan Association for Earthquake Engineering*, *8*(7), 781–791.

Watson, T. H. (1970), A note on fast computation of Rayleigh wave dispersion in the multilayered half-space, *B. Seismol. Soc. Am*, *60, No 1*, 161–166.

Weaver, R. L., and O. I. Lobkis (2006), Diffuse fields in ultrasonics and seismology, *Geophysics*, *71, no 4*, S15–S19, doi:10.1190/1.2212247.

Weaver, R. L., B. Froment, and M. Campillo (2009), On the correlation of non-isotropically distributed ballistic scalar diffuse waves, *J. Acoust. Soc. Am.*, *126*(4), 1817–1826.

Yamada, N., and T. Iwata (2005), Long-period ground motions simulation in the Kinki area during the M_j 7.1 foreshock for the 2004 off the Kii peninsula earthquakes, *Earth Planets Space*, *57*, 197–202.

Yamanaka, H., and N. Yamada (2006), Modeling 3D S-Wave Velocity Structure of Kanto Basin for Estimation of Earthquake Ground Motion, *Butsuri-Tansa*, *59*(6), 549–560.

Yao, H., R. D. van der Hilst, and J.-P. Montagner (2011), Heterogeneity and anisotropy of the lithosphere of SE Tibet surface-wave array tomography, *J. Geophys. Res.*, *115*, B12,307, 24 PP., doi:10.1029/2009JB007142.

Yoshida, M. (2003), Rayleigh to Love wave conversion in a mountain root structure, *Bull. Earthq. Res. Inst. Univ. Tokyo*, *78*, 1–18, doi:00408972.